AD-A268 081

NTATION PAGE

Form Approved
OMB No. 0704-0188

1. AGENCY USE ONLY (Leave blank)	2. REPORT DATE	3. REPORT TYPE AND DATES COVERED
	June 1993	THESIS/DISSERTATION

4. TITLE AND SUBTITLE
A CORRELATIVE COMPARISON OF GEOMAGNETIC STORMS AND AURORAL SUBSTORMS USING GEOMAGNETIC INDICIES

5. FUNDING NUMBERS

6. AUTHOR(S)
Capt William B. Cade III

7. PERFORMING ORGANIZATION NAME(S) AND ADDRESS(ES)
AFIT Student Attending: Utah State University

8. PERFORMING ORGANIZATION REPORT NUMBER
AFIT/CI/CIA- 93-116

9. SPONSORING/MONITORING AGENCY NAME(S) AND ADDRESS(ES)
DEPARTMENT OF THE AIR FORCE
AFIT/CI
2950 P STREET
WRIGHT-PATTERSON AFB OH 45433-77

10. SPONSORING/MONITORING AGENCY REPORT NUMBER

11. SUPPLEMENTARY NOTES

12a. DISTRIBUTION/AVAILABILITY STATEMENT
Approved for Public Release IAW 190-1
Distribution Unlimited
MICHAEL M. BRICKER, SMSgt, USAF
Chief Administration

12b. DISTRIBUTION CODE

13. ABSTRACT (Maximum 200 words)

14. SUBJECT TERMS

15. NUMBER OF PAGES
108

16. PRICE CODE

17. SECURITY CLASSIFICATION OF REPORT	18. SECURITY CLASSIFICATION OF THIS PAGE	19. SECURITY CLASSIFICATION OF ABSTRACT	20. LIMITATION OF ABSTRACT

DISCLAIMER NOTICE

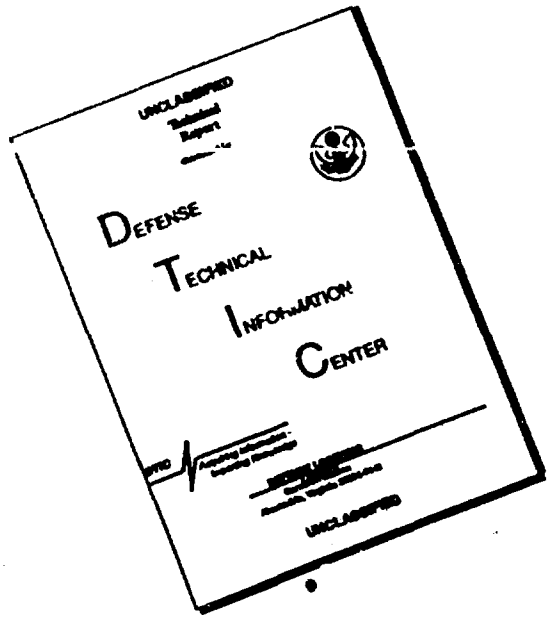

THIS DOCUMENT IS BEST QUALITY AVAILABLE. THE COPY FURNISHED TO DTIC CONTAINED A SIGNIFICANT NUMBER OF PAGES WHICH DO NOT REPRODUCE LEGIBLY.

A CORRELATIVE COMPARISON OF GEOMAGNETIC STORMS AND AURORAL SUBSTORMS USING GEOMAGNETIC INDICES

by

William B. Cade III

A thesis submitted in partial fulfillment
of the requirements for the degree

of

MASTER OF SCIENCE

in

Physics

Approved:

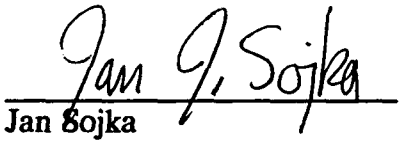

Jan Sojka
Major Professor

William Pendleton
Committee Member

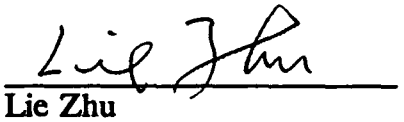

Lie Zhu
Committee Member

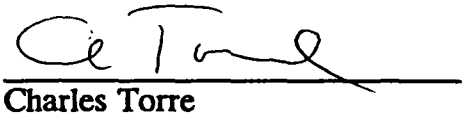

Charles Torre
Committee Member

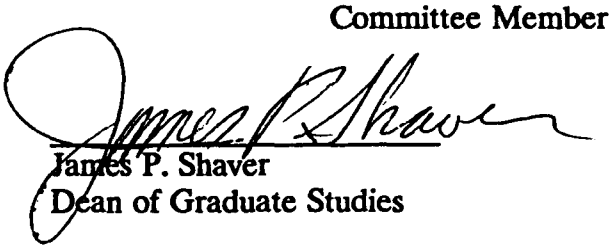

James P. Shaver
Dean of Graduate Studies

UTAH STATE UNIVERSITY
Logan, Utah

1993

ACKNOWLEDGMENTS

This study made use of the CEDAR Data Base at NCAR (National Center for Atmospheric Research), which is supported by the National Science Foundation. The plots contained herein were generated using the plotl program written by Don Thompson.

This work would not have been possible were it not for the help and support of many people. I would like to express my great appreciation to my advisor, Dr. Sojka, for his constant enthusiasm, and for encouraging me to pursue a topic in which I was interested but that neither of us knew much about. His continual interest made all the difference. A special thanks goes to Lie Zhu for his frequent technical assistance as the only researcher on substorm physics at Utah State University. His aid was invaluable. I would also like to thank Devin Della-Rose for his friendship and help during the early stages of my research, Ken Hart for his assistance in obtaining an article that was critical to this work, and my parents, Nelwyn Strain and Bancker Cade, for their support and interest.

Most of all I would like to thank my wife, Beth, for her patience, support, and motivation throughout my class work and research. I couldn't have done it without you. My final gratitude goes to my daughter, Kelsi, who has provided me with some much needed laughter and joy during my work.

William B. Cade III

CONTENTS

LIST OF TABLES

LIST OF FIGURES

ABSTRACT

A Correlative Comparison of Geomagnetic Storms and Auroral Substorms Using Geomagnetic Indices

by

William B. Cade III, Master of Science

Utah State University, 1993

Major Professor: Dr. Jan J. Sojka
Department: Physics

Geomagnetic storms and auroral substorms are usually defined in terms of their respective current systems and measured by geomagnetic indices. While there should be a relationship between the two current systems, finding one has eluded most researchers. However, when a time-weighted accumulation technique is applied to the auroral electrojet index, a clear relationship emerges which shows that the two current systems are indeed dominated by the same directly driven process, differing only in how they respond to the same input. Furthermore, the possibility is demonstrated of modeling and even forecasting the ring current from time-weighted electrojet data.

(118 pages)

CHAPTER 1

INTRODUCTION

One of the first comprehensive theories of geomagnetic storm development was put forth by *Chapman and Bartels* [1940]. They assumed that most of the time the space environment is empty, but at times of geomagnetic storms, plasma from the sun interacts with the earth's magnetic field. In their "corpuscular theory" this interaction produces a magnetic cavity in the solar plasma that confines the earth's magnetic field and produces magnetic storms by the establishment of a temporary "ring current" around the earth in the solar plasma. We now know that solar plasma is always present as the solar wind and that their proposed magnetic cavity continuously exists as the magnetosphere. We also know that geomagnetic storms and substorms are caused by changes in the solar wind and its interaction with the magnetosphere.

Geomagnetic storms have been recognized since the turn of the century as events that impact our world on a global scale. They affect electrical power transmission systems, navigational systems, radars, and cable, radio, and satellite communications. In space they can induce spacecraft charging in satellite systems and cause low-orbiting satellites to be lost. Being able to understand, much less forecast, such storms has been an important goal of geophysical research for decades.

Over the past 25 years, the primary focus of geomagnetic storm research has been in the area of auroral sub storms. The prevalent thought has been that if one can understand the substorm, this will lead to a better understanding of the storm as

a whole. While some relationships have been derived for relatively quiet periods, these correlations break down during times of intense storms. This study will investigate this relationship during intense storms and try to determine, through the use of geomagnetic indices, how the storm and substorm current systems are related, how well they correlate, and if the information contained in the indices has any new application toward storm modeling and forecasting.

CHAPTER 2

GEOMAGNETIC STORM AND SUBSTORM PROCESSES

Magnetospheric Structure

As far as storms and substorms are concerned, the magnetosphere is where most of the action takes place. Understanding of the magnetosphere and its structure is fundamental to the understanding of storms and substorms.

According to *McPherron* [1991], the magnetosphere is a composite of closed and open magnetospheric models. In the closed model, viscous interaction with the solar wind produces the magnetospheric convection pattern shown in Figure 1 and the corresponding ionospheric convection in Figure 2 [*Axford*, 1964]. In the open model, first proposed by *Dungey* [1961], the IMF (interplanetary magnetic field) and the earth's magnetic field merge at x-type neutral lines formed when the IMF is southward (antiparallel). The field lines connect at the front, are carried downstream, and reconnect in the distant magnetotail. This produces the same magnetospheric and ionospheric convection patterns.

Viscous interaction is always present to some degree since magnetospheric convection is observed regardless of IMF orientation. Open lines are apparently always present over the poles, since the polar cap is always open to the solar wind [*McDiarmid et al.*, 1980]. This leads to the topology of open and closed field lines shown in Figure 3. Open field lines are connected at the subsolar point and carried over the poles. Only in the equatorial plane do closed field lines make contact with

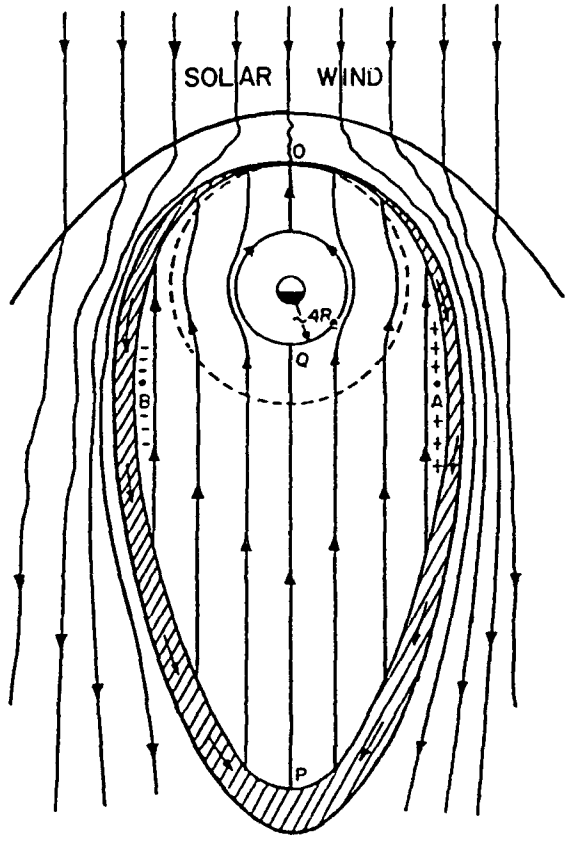

Fig. 1. The magnetospheric convection pattern induced in the equatorial plane by viscous interaction [*Axford*, 1964].

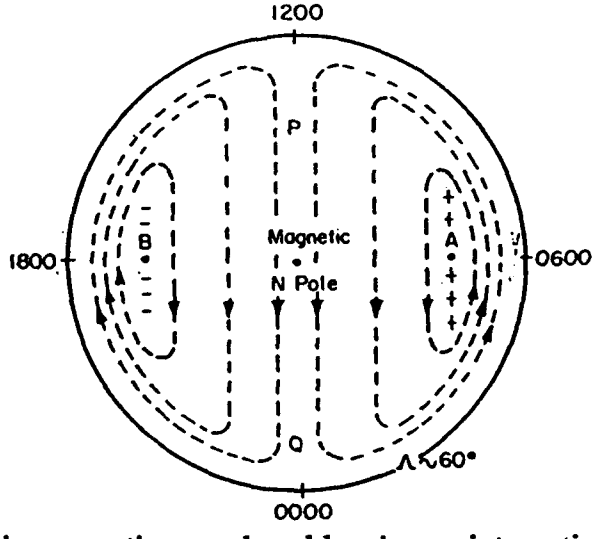

Fig. 2. Ionospheric convection produced by viscous interaction [*Axford*, 1964].

the solar wind, where viscous interaction drags the field lines tailward along the flanks.

In Figure 4, the composite motion of field lines is depicted [in (b) and (c) motion due to viscous interaction is shaded]. Closed field lines are dragged along the sides (a) and return just inside the tailward moving lines (b). The tailward-flowing field lines on the flanks of the magnetosphere form a boundary layer called the low-

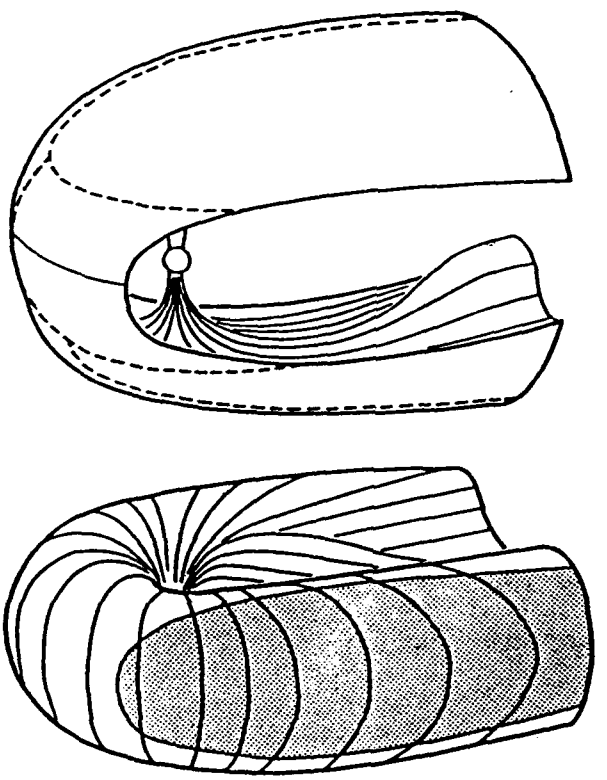

Fig. 3. Topological regions of the composite magnetosphere. The solar wind transports open field lines over the poles (top) while viscous interaction moves field lines along the flanks (bottom) [*McPherron*, 1991].

latitude boundary layer (LLBL). Open field lines that merge at the subsolar point are carried over the poles (a) and flow earthward in the center of the plasma sheet (b), passing around the plasmapause and inside the returning viscous field lines. Part (c) shows the corresponding composite ionospheric convection. Note that this is done for southward IMF – for northward IMF some debate remains over whether reconnection occurs and over the ionospheric convection pattern, although some evidence shows that sunward convection occurs over the poles [*Stern and Alexeev*, 1988]. Figure 5 shows a cross section of the magnetotail, with the various boundary layers depicted. The plasma sheet actually has two distinct layers – the Central Plasma Sheet (CPS) and the Plasma Sheet Boundary Layer (PSBL). Because of antiparallel lines in the two tail lobes, a current sheet (the cross tail current) flows from dawn to dusk across the plasma sheet [*Ness*, 1965].

Through a combination of E field drift and collisions, Hall currents are produced in the ionosphere. Both electrons and ions in the ionosphere drift according to $\boldsymbol{v}=\boldsymbol{E}\times\boldsymbol{B}/B^2$. Since neutrals are also present and the ions experience more collisions, this creates a flow of electrons in the $\boldsymbol{E}\times\boldsymbol{B}$ direction and thus a current in the $-\boldsymbol{E}\times\boldsymbol{B}$ direction. The Hall current has the same pattern as the ionospheric flow shown in Figure 2, but in the opposite direction. The eastward and westward auroral electrojets are simply concentrations of these currents in the high conductivity channels on the night side produced by auroral particle precipitation [*Akasofu*, 1977].

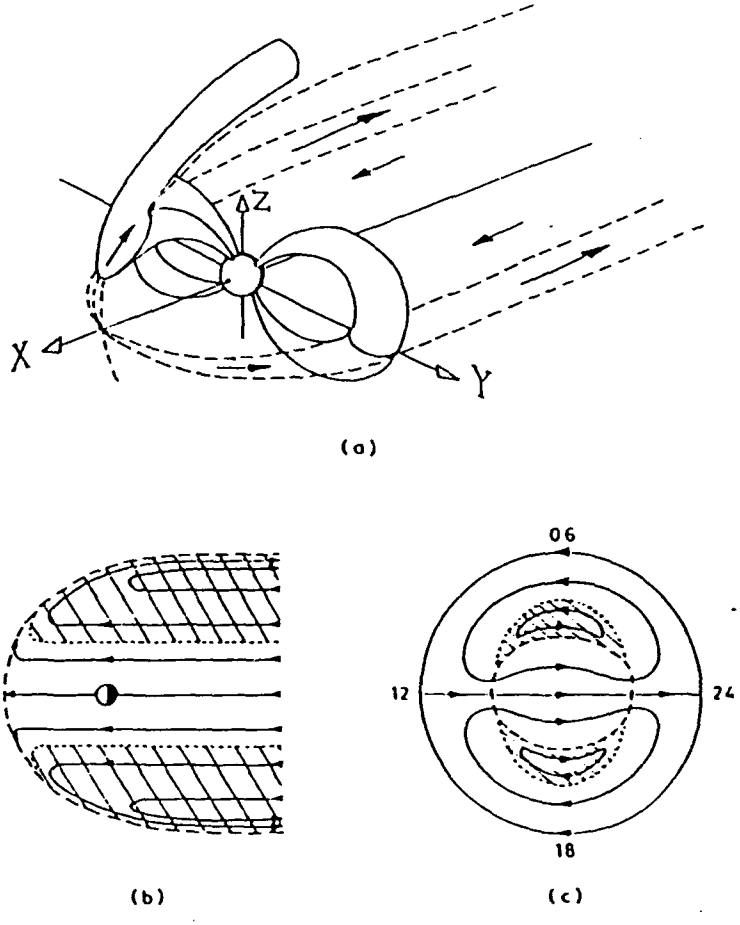

Fig. 4. Composite motion of magnetic field lines resulting from viscous interaction (shaded region) and magnetic reconnection [*Cowley*, 1982].

Charged particles trapped in the plasmasphere (the area within the plasmapause) experience drifts due to curvature of, and gradients in, the earth's magnetic field. The drifts are charge dependent, with positive particles drifting westward and negative particles drifting eastward. This produces a net westward current (Figure 6) that is called the ring current since regions of constant current form toroids around the earth [*McPherron*, 1991].

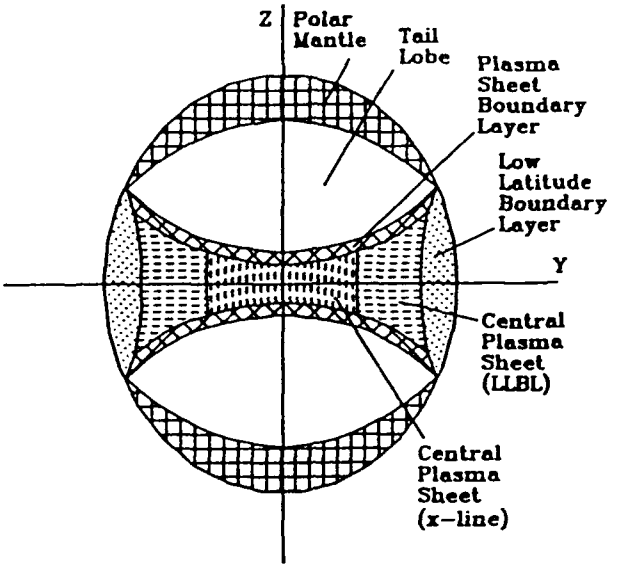

Fig. 5. Cross section of the magnetotail, showing the various boundary layers [*McPherron*, 1991].

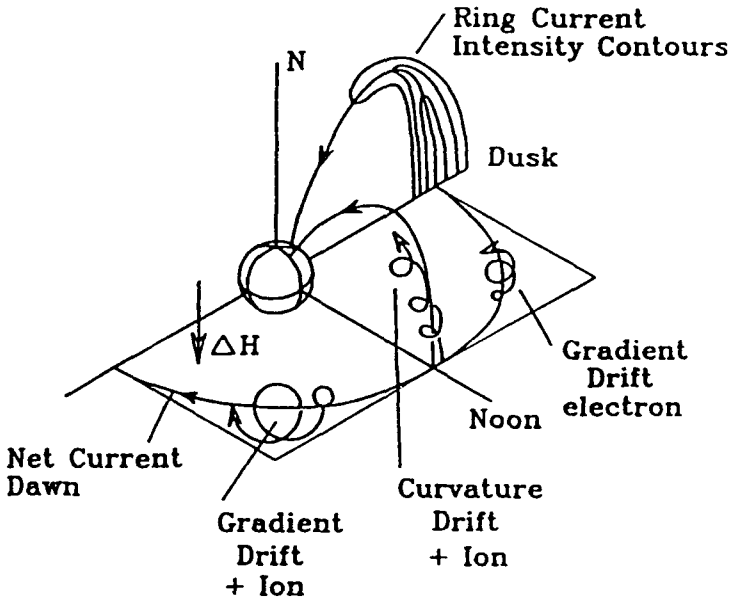

Fig. 6. A perspective view of the dayside plasmasphere showing creation of a westward ring current by particle drifts. Contours of constant current form nested toroids around the earth [*McPherron*, 1991].

Storm/Substorm Morphology and Relationships

Definitions

The definitions of storms and substorms have evolved greatly over the years. Depending on which author is referred to, definitions and especially relationships between storms and substorms can vary greatly. For the purposes of my research, I will use the definitions given by *McPherron* [1991]:

1) A polar magnetic substorm is a description of the temporal and spatial development of magnetic disturbances during a substorm (this is normally described in terms of the ionospheric current systems). An auroral substorm is a description of the sequence of changes in the aurora that accompany the polar magnetic substorm. A magnetospheric substorm is the process that links the magnetosphere to the ionosphere and produces the observed auroral and magnetic activity. The bottom line is that a substorm in general is the enhancement of auroral currents and particle precipitation due to a disturbance in, and increased energy input from, the magnetosphere. This disturbance is in turn rooted in changes in the solar wind's input into the magnetosphere. Substorms generally last one to two hours.

2) A geomagnetic storm is the manifestation in the earth's surface magnetic field of first a compression of the magnetosphere by enhanced solar wind and then an intensification of the ring current. A geomagnetic (or simply magnetic) storm can last for several days and involves frequent substorm activity.

Substorm Phases

As a chiefly auroral phenomenon, substorms are best observed at high latitudes. There is general agreement that substorms have three identifiable phases as outlined below:

1) The growth phase is the period during which disturbances in a variety of phenomena become increasingly apparent. There is a gradual increase in the eastward and westward electrojets, and local auroral brightenings may occur [*McPherron*, 1979]. In the magnetosphere, the magnetic field strength in the tail lobes increases and the plasma sheet thins in the north-south direction [*Tascione*, 1988].

2) Figure 7a shows the auroral regions prior to substorm onset (quiet conditions). Discrete auroral arcs are present in the nighttime auroral oval and in the polar cap. At the onset of the expansive phase the most equatorward auroral arc in the midnight sector brightens (Figure 7b). This arc expands poleward (the poleward bulge, Figure 7c) with the region behind filled with wavelike auroral forms. The duskward edge of this bulge forms a wavelike disturbance called the westward traveling surge (Figure 7d). On the dawn side the aurora forms wavelike, omega-shaped bands (omega bands) that drift eastward and the auroral arcs break up into eastward drifting, pulsating patches [*Akasofu*, 1977]. At the same time as the first brightening, there is a strong increase in the westward electrojet. The enhanced electrojet region expands westward with the westward traveling surge. The eastward electrojet also increases in intensity. At the beginning of the expansion phase in the

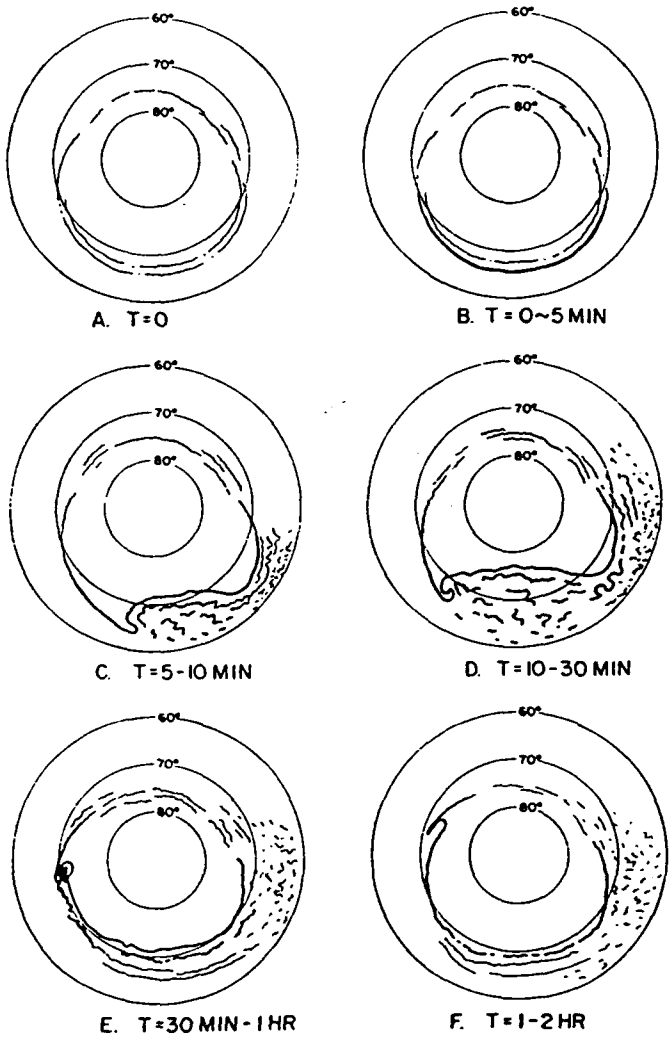

Fig. 7. Schematic showing the growth and decay of an auroral substorm [*Akasofu*, 1964].

magnetotail, the tail field decreases and there is an explosive acceleration of plasma towards the earth as a portion of the tail current is diverted along field lines (by some unknown process). This field-aligned current connects through the ionosphere as the

enhanced westward electrojet; collectively this system is called the substorm current wedge (Figure 8) [*McPherron*, 1979].

3) The recovery phase begins when poleward expansion stops and auroral arcs reform and drift equatorward (Figures 7e and f). The aurora, electrojets, and the magnetotail field return to their prestorm configurations [*McPherron*, 1979].

Many substorms exhibit much more complex behavior than is described in the ideal case. Multiple onsets or intensifications in the expansion phase can occur in which many sudden intensifications in the electrojet are measured. Pseudo break-ups can occur, where brightenings of irregular auroral waves occur and expand poleward. These pseudo break-ups last only a few minutes and are very weak and localized [*Tascione*, 1988].

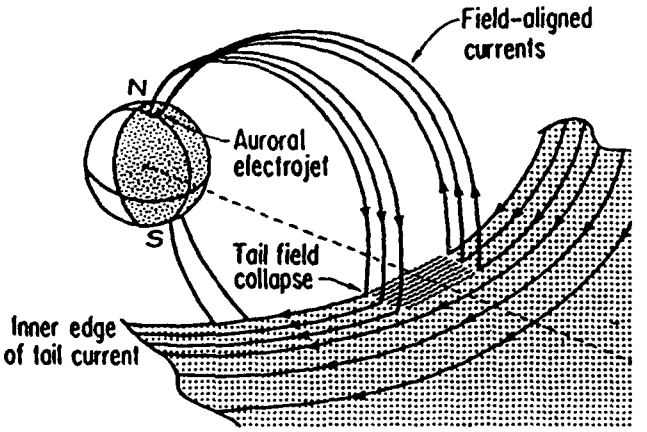

Fig. 8. A perspective view of the substorm current wedge that develops during the substorm expansion phase [*Clauer and McPherron*, 1974].

Storm Phases

Magnetic storms are best observed at mid and low latitudes where the primary effect is a reduction of the horizontal magnetic field. Magnetic storms usually have well defined phases as follows:

1) The initial phase begins with the sudden storm commencement (SSC). The SSC appears as a sudden worldwide increase in the horizontal magnetic field, which is due to a compression of the magnetosphere by a shockwave in the solar wind. This phase lasts from 1 to 16 hours during which time the horizontal field remains increased [*Knecht and Shuman*, 1985].

2) The main phase begins as the horizontal field rapidly decreases to below pre-storm levels. This is due to the enhancement of the westward ring current by particles injected from the solar wind. Coincident with the decrease, the auroral oval expands equatorward and frequent substorms occur. The main phase can last from several hours to a few days [*Knecht and Shuman*, 1985].

3) The recovery phase consists of the cessation of substorm activity and a quiet return of the horizontal field to prestorm levels. The recovery phase can last for several days [*McPherron*, 1991].

Storm/Substorm Relationships

As alluded to earlier, there is some disagreement about how storms and substorms are related. Some believe, as *Akasofu* [1977, p. 294] states, "... a geomagnetic storm period can be identified as the period when intense substorms

occur frequently." In 1978 C. T. Russell said (as quoted by *Feldstein* [1992, p. 85]), "A magnetic storm is not composed of successive substorms. A storm is something different. Substorms are only incidental, not fundamental, of the storm development."

It seems, however, the majority believe that the same mechanisms that produce substorms also produce storms, as is implied by most authors of substorm models. *McPherron* [1991] reasoned that whatever process that produces substorms also creates enhanced plasma convection in the magnetotail. When convection is enhanced, this increases the magnetotail convection electric field and this in turn compresses the plasmapause earthward. Convecting particles now penetrate closer to the earth, gain energy, and join the ring current. As the tail electric field fluctuates, and the plasmapause expands, the new particles in this region become trapped in the plasmasphere and thereby energize the ring current. This view is supported by other authors, such as *Lyons and Schultz* [1989] and *Fairfield* [1992].

Others believe the ionosphere is the primary source of ring current energization during storms. *Cladis and Francis* [1985] used computer simulation to show that storm-time ring current population can mainly be accounted for by ions streaming out of the polar ionosphere along magnetic field lines. *Wrenn* [1989] studied particle lifetimes in the ring current to show that a large fraction of the ring current is of ionospheric origin.

Substorm Processes

Driven Model

The driven model was introduced by *Akasofu* [1981a] to show that substorms are created totally by a driven process. A driven process is one in which energy input from the solar wind is continuously fed into the magnetosphere and ionosphere so that no energy is stored and then released (a loading-unloading system). The solar wind-magnetosphere dynamo, which produces the magnetospheric-ionospheric convection and current systems, is the mechanism that dissipates energy from the solar wind; however, detailed physical processes producing substorms are not specified.

Akasofu defined the epsilon parameter $\epsilon = VB^2l^2\sin^4(\theta/2)$, where V is the solar wind speed, B is the magnitude of the IMF, l^2 is a constant proportional to the area of the magnetopause through which energy is input, and θ is the angle the IMF makes with the horizontal. The ϵ parameter represents the amount of energy flux from the solar wind into the magnetosphere and was derived from the fact that geomagnetic activity is controlled by the strength and orientation of the IMF. Akasofu showed that ϵ correlated well with the total energy dissipated in the magnetosphere during substorms, which implies that substorms are a totally driven process. According to this model, substorms will occur whenever ϵ reaches a critical value (~10^{18} ergs/sec) and they are a result of increased power to the solar wind-magnetosphere dynamo.

Near-Earth Neutral Line Model

The near-earth neutral line (NENL) model is the most widely accepted and probably the most extensively developed model of substorm processes. The basic premise of the model, first developed in the 1970's [e.g., *Russell and McPherron*, 1972; *Schindler*, 1974; *Hones*, 1977] and most recently reviewed by *McPherron* [1991], is the formation of a second neutral line in the magnetotail.

The NENL model growth phase is due to a driven process and begins with erosion of the magnetopause. When magnetic flux from the solar wind increases and exceeds the flux transported to the subsolar neutral line in the magnetosphere, the neutral line must move earthward to balance. The result of this is "erosion" of the dayside magnetopause as successive layers of previously closed field lines are opened to the solar wind. These field lines are transported over the poles and flux accumulates in the tail lobes since tail reconnection does not occur immediately (this delay is mostly due to the time it takes the solar wind to transport the new reconnection discontinuity to the distant neutral line). The added flux causes the distant tail lobes to grow in size and causes an increase in the intensity of the near-earth lobe field. In response, the near-earth tail current flowing between the lobes must increase as the lobe field increases. Also, the near-earth current sheet thins because of increased magnetic pressure in the lobes and the loss of magnetic flux to dayside reconnection. Many of the aspects of the growth phase are shown schematically in Figure 9.

The convection electric field increases due to: 1) a rarefaction wave generated by dayside reconnection that propagates around the earth, where in the plasma sheet it accelerates plasma sunward; 2) increased reconnection that allows the solar wind electric field to be mapped to the polar cap; and 3) the increase in the near-earth tail magnetic field. This increased electric field moves the plasmapause earthward, allowing the tail current to move earthward and letting more particles enter the ring current. The ionospheric electrojets increase due to enhanced conductivity (from the earthward tail current movement which increases particle precipitation) and the

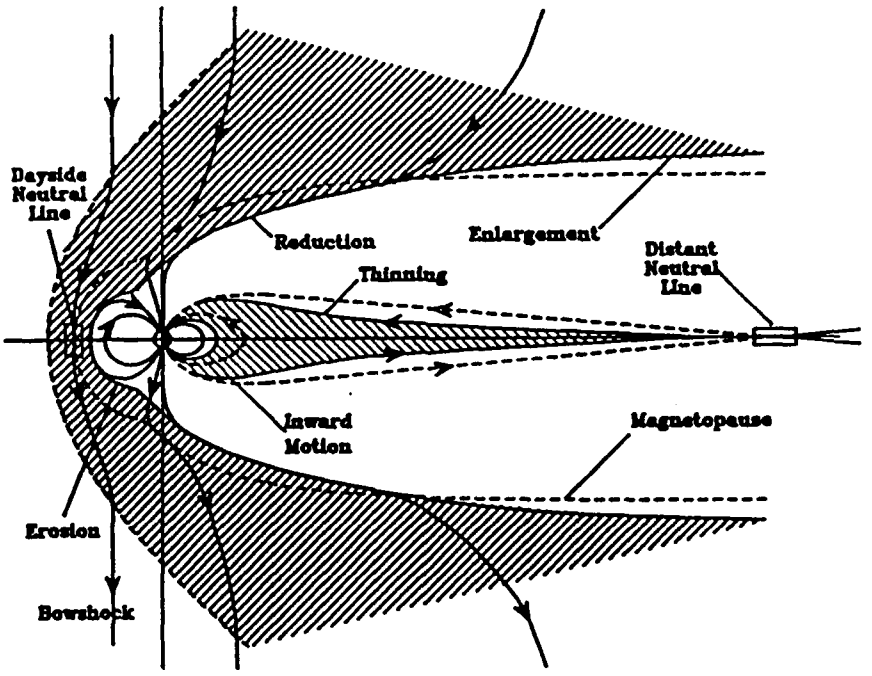

Fig. 9. Changes in the magnetosphere caused by a southward turning of the IMF [*McPherron*, 1991].

enhanced electric field. This in turn causes the Region 1 and 2 currents to increase by current continuity.

The basis of the NENL model is the formation of a neutral line in the magnetotail region of 10-30 R_e (Figure 10). Fast compression and rarefaction waves, which communicate magnetospheric changes to the plasma sheet, can reduce the normal magnetic field component to zero in the closed field line region of the near-earth plasma sheet and form an x-type neutral line [*Coroniti*, 1985]. Also, recent computer simulations using MHD processes support the formation of a near-earth neutral line [*Voigt and Wolf*, 1988; *Birn and Hesse*, 1991; *Scholer and Hautz*, 1991]. The neutral line first forms in the CPS and reconnection begins there. Reconnection is initially slow since the reconnection rate is proportional to the Alvén velocity, which is slow in the CPS. As reconnection continues, it reaches the PSBL and the rate increases due to the increased Alvén velocity. Eventually the last closed field line that defines the plasma sheet boundary is severed and the reconnection rate dramatically increases in the tail lobes. In the tail anti-earthward of the near-earth neutral line, a plasmoid (a "bubble" of closed magnetic field lines) is formed (Figure 11). The onset of the expansion phase, which is due to a loading-unloading process (the accumulation and release of lobe magnetic flux), is defined as the moment the last closed field line is cut and the plasmoid begins to retreat. The plasmoid retreats anti-sunward, as shown in Figure 11, because of the tension in the IMF field lines that now separate it from the near-earth neutral line. The NENL model is largely

based on distant tail observations that seem to show the passage of a plasmoid [*Hones et al.*, 1984; *Baker et al.*, 1987; *Nishida et al.*, 1988; *Slavin et al.*, 1989].

The formation of a plasmoid also requires some kind of current diversion from the reconnection region. To produce an x-line geometry, the tail current in the x-line region must be reduced. This can be done by introducing field-aligned currents that divert current away from the x-line region and close through the ionosphere (Figure 12). This is how the substorm current wedge is formed.

Eventually the NENL retreats tailward, as depicted at the bottom of Figure 11, during the recovery phase. There is no clear cause of this retreat, but when the IMF turns northward and reconnection ceases, there is flux in the magnetotail waiting to be reconnected. The simplest way to solve this problem is for the neutral line to move tailward, adding excess flux to the plasma sheet behind it.

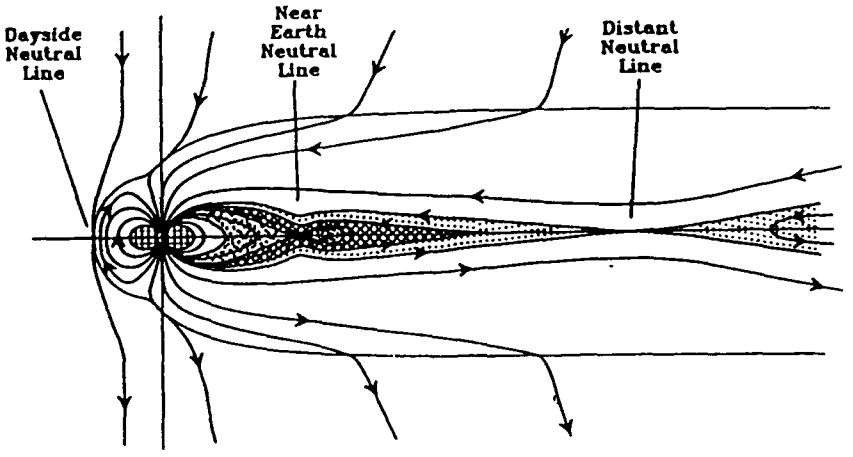

Fig. 10. The formation of a near-earth neutral line within the CPS during the late growth phase [*McPherron*, 1991].

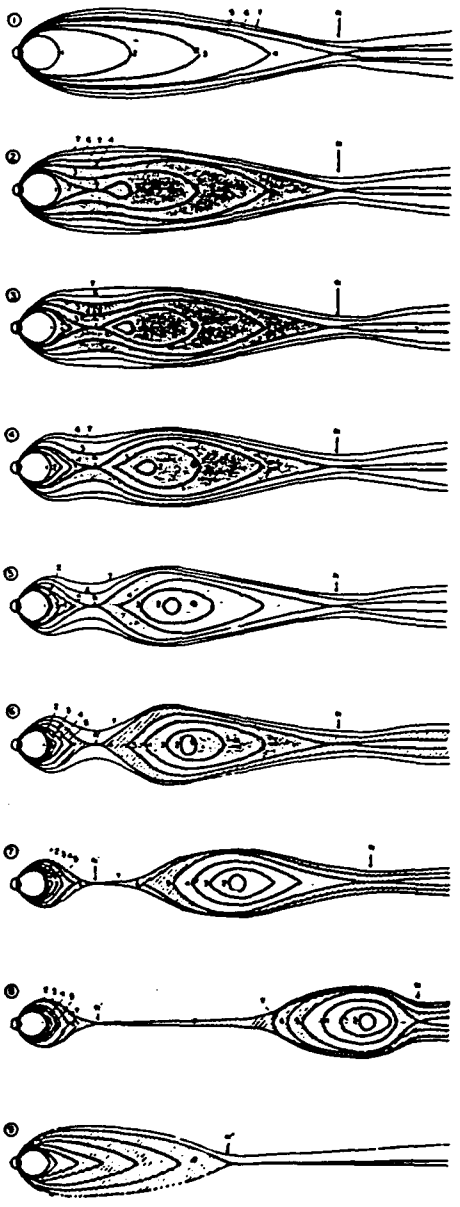

Fig. 11. The formation and retreat of a plasmoid during a substorm [*McPherron*, 1979].

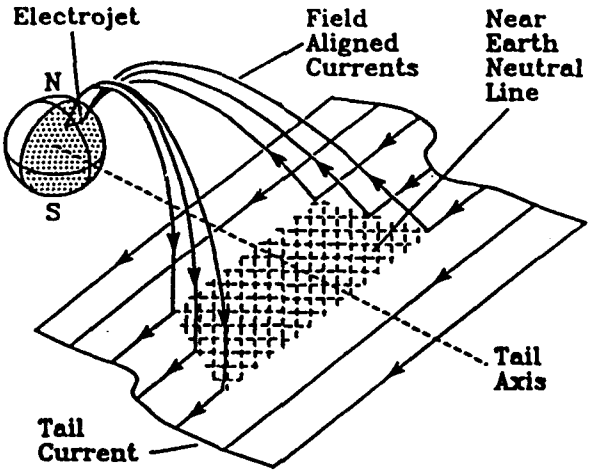

Fig. 12. The diversion of the tail current through the ionosphere during the substorm expansion phase [*McPherron*, 1991].

CHAPTER 3

DATA DESCRIPTION

Geomagnetic Indices

Dst Index

The *Dst* index was first derived both by *Sugiura* [1964] and *Kertz* [1964] and was conceived as a measure of the intensity of the equatorial ring current. Since the ring current is assumed to be mostly a symmetric, equatorial, zonal current, its magnetic field at the surface is parallel to the dipole axis and seen mainly in the horizontal component (H) of the magnetic field [*Rangarajan*, 1989]. The method of Sugiura is essentially that which is in use today, in which the average disturbance of the horizontal field, D, is made up of two parts: 1) a universal-time part *Dst*; and 2) a local-time dependent part *DS*. For a uniform longitudinal distribution of stations, the mean value of D at any instant will not be contaminated by *DS*, so that essentially *Dst* is measured. And since the spatial and temporal variations in ring current intensity are not rapid, a dense network of stations is not needed. Currently, *Dst* is measured by four stations (Table 1) that are located far enough from the magnetic equator so that they are not affected by the equatorial electrojet, yet close enough to the equator to minimize auroral effects [*Rangarajan*, 1989].

In computing the index, hourly observations at each station are taken. The diurnal solar-quiet (*Sq*) variation is computed at each station for each month for the 5 quietest days, then from the series of monthly *Sq* for the year, a double Fourier

Table 1. Coordinates of the magnetic stations of the *Dst* network [adapted from *Rangarajan*, 1989].

Station	Geographic Latitude	Geographic Longitude	Dipole Latitude	Dipole Longitude
Honolulu	21.32	-158.00	21.36	267.97
San Juan	18.12	-66.16	29.41	4.65
Hermanus	-34.42	19.23	-33.59	81.99
Kakioka	36.23	140.18	26.31	207.25

series is expanded:

$$\sum_{n=1}^{6}\sum_{m=1}^{6} A_n^m \cos(mT+\alpha_m)\cos(nM+\beta_n) \qquad (1)$$

where T is local time and M is the month. One then has 12×24 experimental data to determine the 48 unknown coefficients. The hour values of a synthetic *Sq* variation are computed from the Fourier series and are subtracted from the original hourly values. The reference level at each station is determined by a parabola fitted to the annual means of H for the 5 quietest days each month [*Mayaud*, 1980].

Although a synthetic *Sq* is used to remove regular variations, some residual variation may remain in the index. Also, the effects of the partial ring current and magnetospheric compression by the solar wind are not removed. This leaves the symmetric ring current, partial ring current, and magnetospheric compression as the primary sources for *Dst*. During quiet periods magnetospheric compression is

removed along with *Sq*, but during storms the effect can be 10 to 40 nT [*Baumjohann*, 1986].

Auroral Indices

The auroral indices *AE, AL, AU*, and *AO* (hereafter called the *AE* indices) were first introduced by *Davis and Sugiura* [1966] to measure the auroral electrojets and are discussed in detail by *Mayaud* [1980]. Using a chain of 12 auroral stations (Figure 13), a quiet time reference level is derived for each month at each station from the 5 quietest days. This level is subtracted from the 2.5 or 1-minute *H* data for each station, the data is superposed in universal time, and the extreme positive and negative values at each instant define *AU* and *AL*, respectively. The 2.5 or 1-minute values are averaged to produce hourly values which are the ones used in this study. *AL* should measure the intensity of the westward electrojet, while *AU* should measure the intensity of the eastward electrojet. However, these indices also contain contributions from any other zonal currents (in the ionosphere and beyond), mainly the ring current, so *AE* is defined as *AU–AL* so as to remove any symmetric zonal contribution. *AO*, defined as *(AU+AL)/2*, is then intended to be an approximate measure of the equivalent zonal current. Since there is asymmetry between the eastward and westward electrojets, however, *AO* really measures this asymmetry plus zonal current effects.

Some problems with the *AE* indices that must be remembered are [*Mayaud*, 1980]:

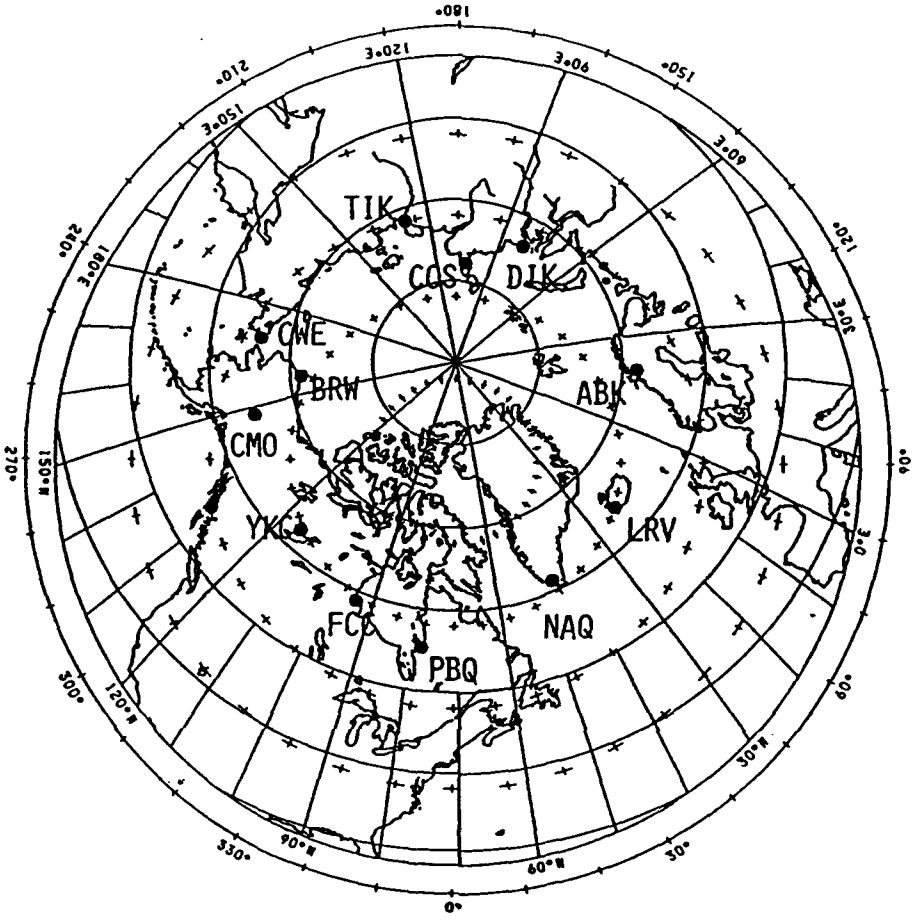

Fig. 13. The chain of *AE* stations. Geographic coordinates are indicated by solid lines, and geomagnetic coordinates are shown by plus signs [from *Data Book 21*, WDC-C2 for Geomagnetism, Kyoto, Japan, 1992].

1) Underground effects induced by the rapidly fluctuating currents.

2) The direction of *H* (magnetic north) in which the measurements are made may not be normal to the electrojets.

3) The present network of stations is not ideal. Since longitudinal gaps are present, a low *AE* does not preclude substorm activity.

4) Ring current effects are present in *AU* and *AL* and are important when *Dst* is large.

5) The daily regular variation of *H* is not eliminated. Although this is not significant during active periods (the daily variation is tens of nT while the electrojet variations are hundreds of nT), the daily variation itself can define *AU* and *AL* during quiet periods.

6) The indices cannot distinguish between movement of the auroral oval away from (or towards) the station and weakening (or strengthening) of the electrojet.

7) According to *Berthelier* [1976], the B_y component of the IMF makes some contribution to the *AE* index.

Akasofu et al. [1983] addressed the question of the accuracy of the *AE* indices by comparing them to *AE* from a chain of 70 stations used during the IMS (International Magnetospheric Study). They found that the relative accuracy of the *AE* indices became progressively worse for lower values (although the overall correlation was ~0.93) and suggested a critical value of 250 nT, below which one should be cautious of the value of *AE*. Overall, however, the advantages of the *AE* indices far outweigh the deficiencies as the indices are directly related to physical processes.

Data Period and Data Sets

Storm Criteria and Data

The problem of how to define a storm is not simple since one can be defined in so many ways. They can be classified in terms of the indices *Ap*, *ap*, *Kp*, or *Dst*. A storm can also be defined in terms of its effects, both terrestrial and orbital. For this study I will adopt but modify the criteria used by NOAA's Space Environmental Services Center (SESC). Their criterion for a severe geomagnetic storm is $Ap \geq 100$, however, I will use $Ap^{*} \geq 100$ (*Ap* is taken from 0000 to 2400 GMT, while Ap^{*} is the maximum possible value over any 24 hour period). I will also supplement this with the additional criterion of $Dst \leq -200$ nT to insure no storms with large ring current intensifications are missed.

The data used for most of this study is geomagnetic indices and IMF data from solar cycle 21, from 1978 to 1986. Table 2 shows data for the 21 storms that meet the above criteria, and Figure 14 shows the superposed *Dst* traces for the 21 storms.

Storm Examples

Figure 15 shows an example of *AE* and *Dst* for a "normal" storm. In the top figure is the 1-minute *AE* for the storm. It exhibits very rapid fluctuations and has an almost noisy appearance. The middle figure is the 1-hour *AE* index, which is an average of the 1-minute data. The trace still shows that the *AE* index is subject to rapid temporal changes since the substorm time scale is relatively short (1-2 hours).

Table 2. Summary of data for the 21 storms selected from solar cycle 21.

Storm Number	Date	81 Day F10.7	Ap*	Min Dst	Max 3hr Kp
1	May 1-4, 1978	142	130	-150	8_+
2	Aug 27-30, 1978	135	128	-226	8_+
3	Sep 27-30, 1978	152	122	-224	8_o
4	Apr 3-6, 1979	178	91	-202	8_o
5	Apr 24-28, 1979	177	126	-149	8_o
6	Dec 19-22, 1980	193	80	-240	8_-
7	Mar 5-8, 1981	209	82	-215	7_+
8	Apr 11-14, 1981	212	134	-311	8_+
9	Jul 24-27, 1981	206	161	-226	8_+
10	Mar 1-4, 1982	202	140	-211	8_o
11	Jul 13-16, 1982	172	230	-325	9_o
12	Aug 6-9, 1982	166	116	-155	8_-
13	Sep 5-8, 1982	163	201	-289	9_-
14	Sep 21-24, 1982	163	148	-210	8_+
15	Jan 9-12, 1983	155	86	-213	8_+
16	Feb 4-8, 1983	128	158	-183	8_o
17	Apr 25-29, 1984	128	103	-93	8_-
18	Sep 22-25, 1984	77	115	-75	7_o
19	Nov 15-18, 1984	73	125	-141	8_o
20	Apr 19-23, 1985	78	118	-158	8_+
21	Feb 7-10, 1986	76	229	-307	9_o

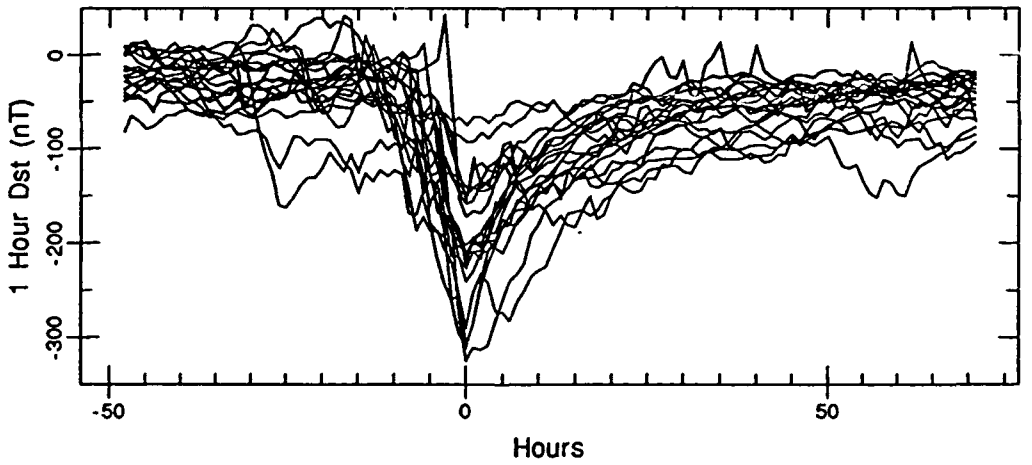

Fig. 14. Superposed *Dst* traces for the 21 storms from solar cycle 21. The peak of each trace occurs at t=0.

At the bottom is a classic *Dst* storm profile, where each storm phase is visible. From an initial baseline of low activity (*Dst*~0), the trace exhibits a sharp increase associated with magnetospheric compression (the sudden storm commencement). The field then decreases rapidly as the ring current is intensified (main phase), reaches its maximum, and decays slowly back to the baseline level (recovery phase). It is evident from Figure 15 that very different time scales are at work in the two current systems.

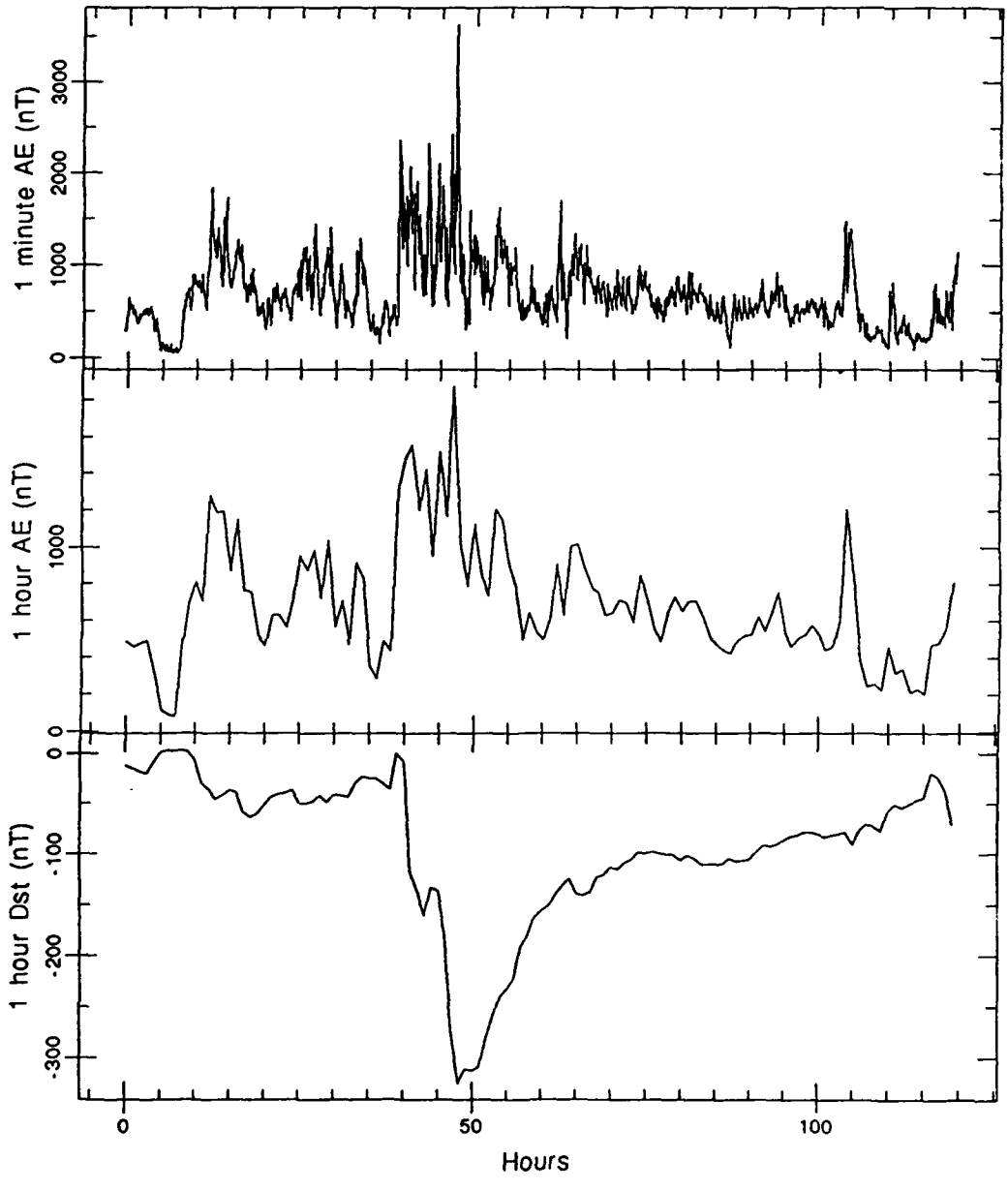

Fig. 15. Example of a normal storm in 1 minute *AE*, 1 hour *AE*, and 1 hour *Dst*. This storm is from July 13-16, 1982 (Storm 11).

CHAPTER 4

COMPARISONS OF DST AND AE

Rationale

While a relationship between the auroral electrojets and the ring current seems plausible, since both are driven by the same basic source (the solar wind), very rarely has this relationship been explored. The very nature of what the relationship might be is unknown, and some doubt one even exists. Are substorms a fundamental part of storm development, or are they coincident but not necessary? An investigation of the association between the storm and substorm current systems should be able to provide at least a start on answering this question.

Previous Work

One of the first direct comparisons of *Dst* and *AE* was made by *Davis and Parthasarathy* [1967]. They found that 1) the onset of *AE* activity precedes *DR* (similar to *Dst*) enhancement by as much as 15 hours for geomagnetic storms; 2) the amplitude of the maximum *DR* is directly proportional to the sum of the *AE* values for the previous 10 hours (they achieved a correlation coefficient of 0.82 for 32 magnetic storms in 1958); and 3) the energy injection function to the ring current (derived by them) looks very similar to the time variation of *AE*, indicating that both are energized by the same process.

Akasofu [1981c] made a direct comparison of the *AE* and *Dst* indices for several different solar rotation periods. Figure 16 shows a scatter plot of a quiet rotation period and Figure 17 shows a plot for a period that contained a geomagnetic storm. Akasofu concluded that while there is a linear relationship at relatively quiet periods (*Dst* > -50 nT), during storms there is no longer a relationship between the two indices since during the lowest *Dst* values the *AE* index could be relatively low.

Siscoe [1982] used an electrical circuit analogy to study the energy coupling between the ring current, ionospheric currents, and field-aligned currents. He found that while *AE* varies linearly with the B_z component of the IMF, *Dst* varies as B_z^2, so that the two indices would necessarily have different responses to a southward IMF.

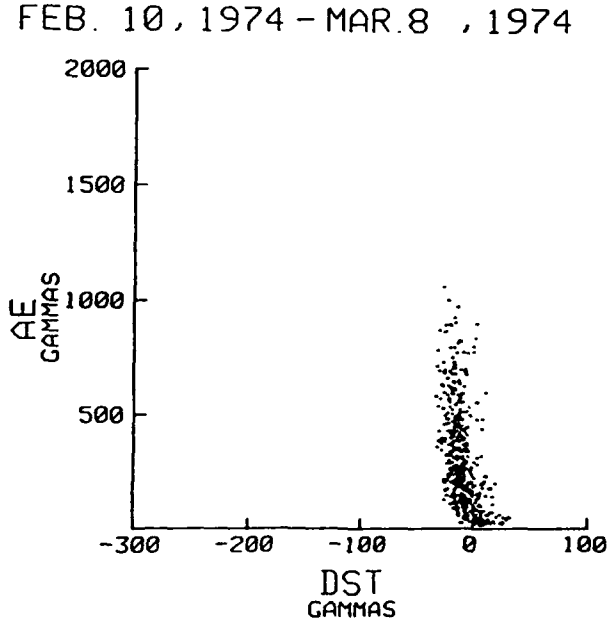

Fig. 16. The relationship between *AE* and *Dst* indices for the Bartel's rotation period 1922 (February 10-March 8, 1974) [*Akasofu*, 1981b].

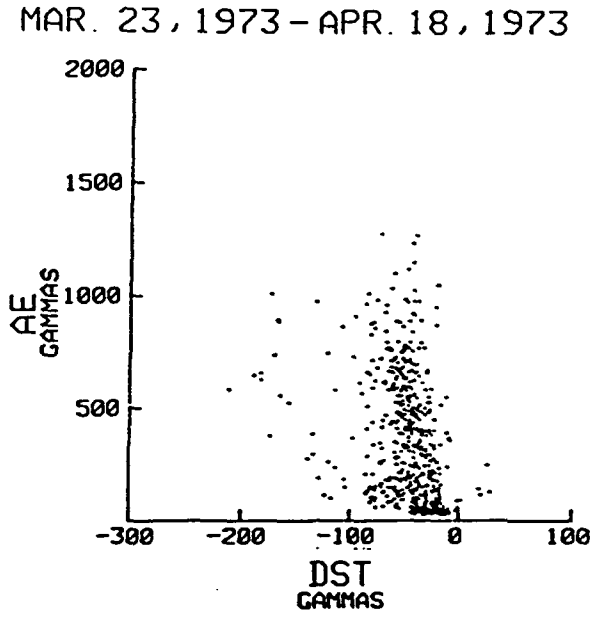

Fig. 17. The relationship between *AE* and *Dst* indices for the Bartel's rotation period 1910 (March 23-April 18, 1973) [*Akasofu*, 1981b].

While not using the *AE* index, *Wrenn* [1989] compared 3-hour *ap* to *Dst* by using a weighting factor τ applied to *ap*. This attenuation factor τ was first introduced by *Wrenn* [1987] in comparing *ap* to ionospheric parameters. This factor (which can vary between 0 and 1) added increased weighting to previous values and imposed an exponential decay time constant of $3/(1-\tau)$ hours. The new time-weighted index was given by:

$$ap_t(\tau) = ap_{t-1}(\tau)+(1-\tau)[ap-ap_{t-1}(\tau)]/3 \qquad (2)$$

Although Wrenn compared $ap(\tau)$ to *Dst*, he disregarded intense storms by eliminating

data 100 hours after *Dst* < 150 nT and 6 hours after a sudden storm commencement. From his comparisons he concluded that ring current particles have longer lifetimes during solar maximum than solar minimum and that a significant portion of ring current particles is of ionospheric origin.

In the recent review of current storm and substorm research by *Fairfield* [1992], he gave Figure 18 as a summary of the current thinking on substorm research. This figure indicates that *AE* is dominated by directly driven processes (i.e., magnetospheric convection) while the actual impulsive substorm component (from loading-unloading processes) is superposed on the directly driven part. This view is shared by *Lee et al.* [1985] and *Liu et al.* [1988] who both state that the *AE* index is composed of an enhanced level component that is directly driven, with an impulsive component (from plasmoid formation) superposed on this background level. Not shown in Figure 18 is the ring current, which is largely believed to also be directly driven by magnetospheric convection. This implies that some relationship should exist between *Dst* and the directly driven component of *AE*.

Smoothing/Weighting Techniques Applied to AE

From Akasofu's work, it seems clear that no elementary relationship can exist between *AE* and *Dst* because the current systems they measure have fundamentally different time constants. While *Dst* exhibits a fairly fast rise and very slow decline, *AE* can fluctuate greatly over a period of hours (see Figure 15), hence the large scatter in Figure 17. If one were able to compensate for the different time constants,

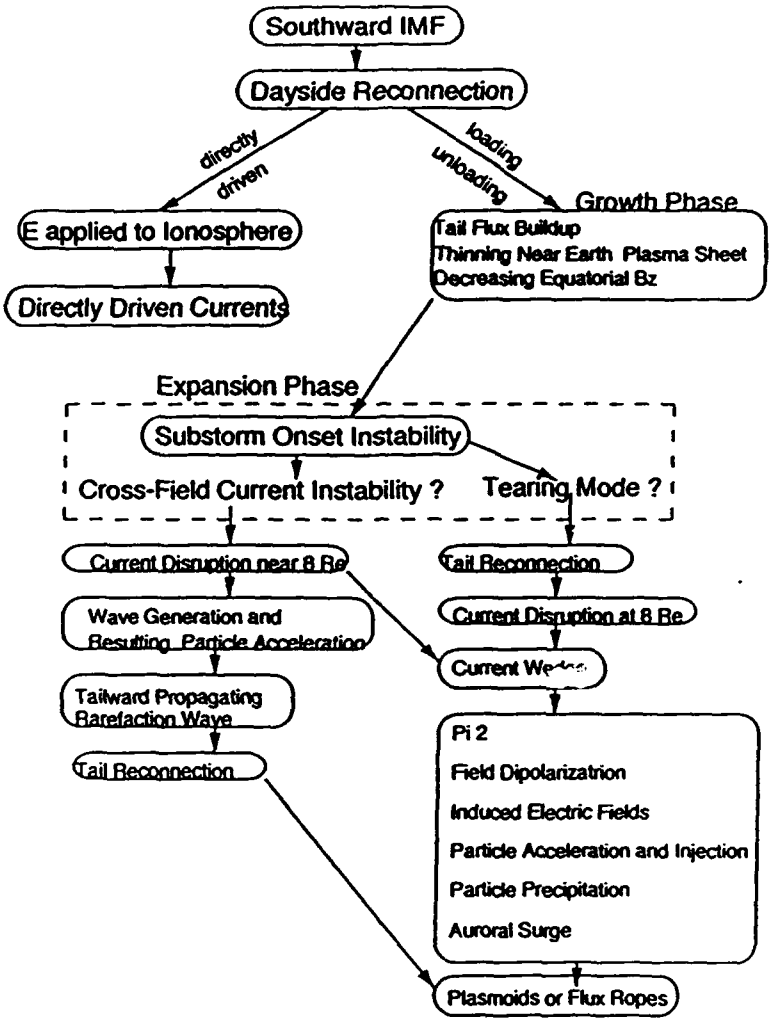

Fig. 18. Summary of much of current thinking on magnetospheric storms [*Fairfield*, 1992].

a clearer picture might emerge. This was attempted on a limited basis by Davis and Parthasarathy when they found that the maximum *DR* of a storm was related to the integrated *AE* activity over the past 10 hours. In addition, by looking at Figure 18,

one might also find a better relationship if *Dst* is compared to only the directly driven component of *AE*.

A simple space-centered smoothing technique was applied to the 1-hour *AE* data for each of the 21 storms selected for this study. This procedure was used to attempt to estimate the trend of the data and recover an average baseline that might better approximate the directly driven currents. An example of this technique for different smoothing iterations is shown in Figure 19.

The technique of time-weighted accumulations applied by *Wrenn* [1987] to *ap* appears to be able to resolve, at least partially, the problem of the differing time constants. If the τ technique were applied to *AE*, this might produce a better correlation to *Dst*, especially during storms. The following formula was used to apply the τ weighting to the *AE* indices:

$$AE_t(\tau) = AE_{t-1}(\tau)+(1-\tau)[AE_t-AE_{t-1}(\tau)] \qquad (3)$$

This was done for several values of τ, examples of which are shown in Figure 20. It is apparent in the figure that as the value of τ increases, more weight is given to previous indices and the curve becomes smoother and flatter. This has the physical significance of injecting the auroral energy into a system with a much slower response time or time constant. The new time constant for a $1/e$ decay can be defined as $\approx 1/(1-\tau)$ hours, which for a τ of 0.9 is 10 hours.

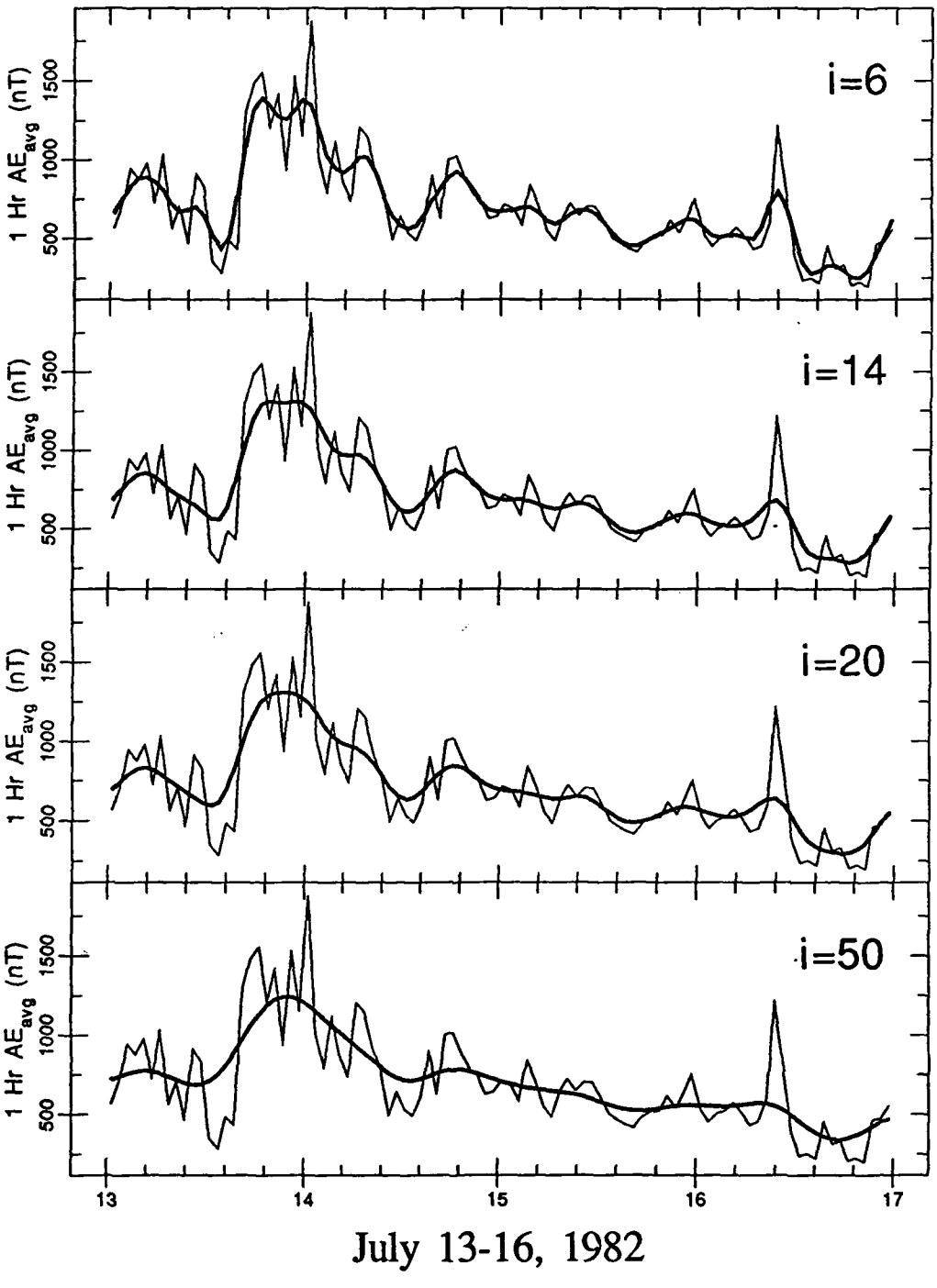

Fig. 19. Examples of space-centered smoothing of *AE* (thin line) for 6, 14, 20, and 50 averaging iterations to achieve AE_{avg} (bold line) (i is the number of iterations).

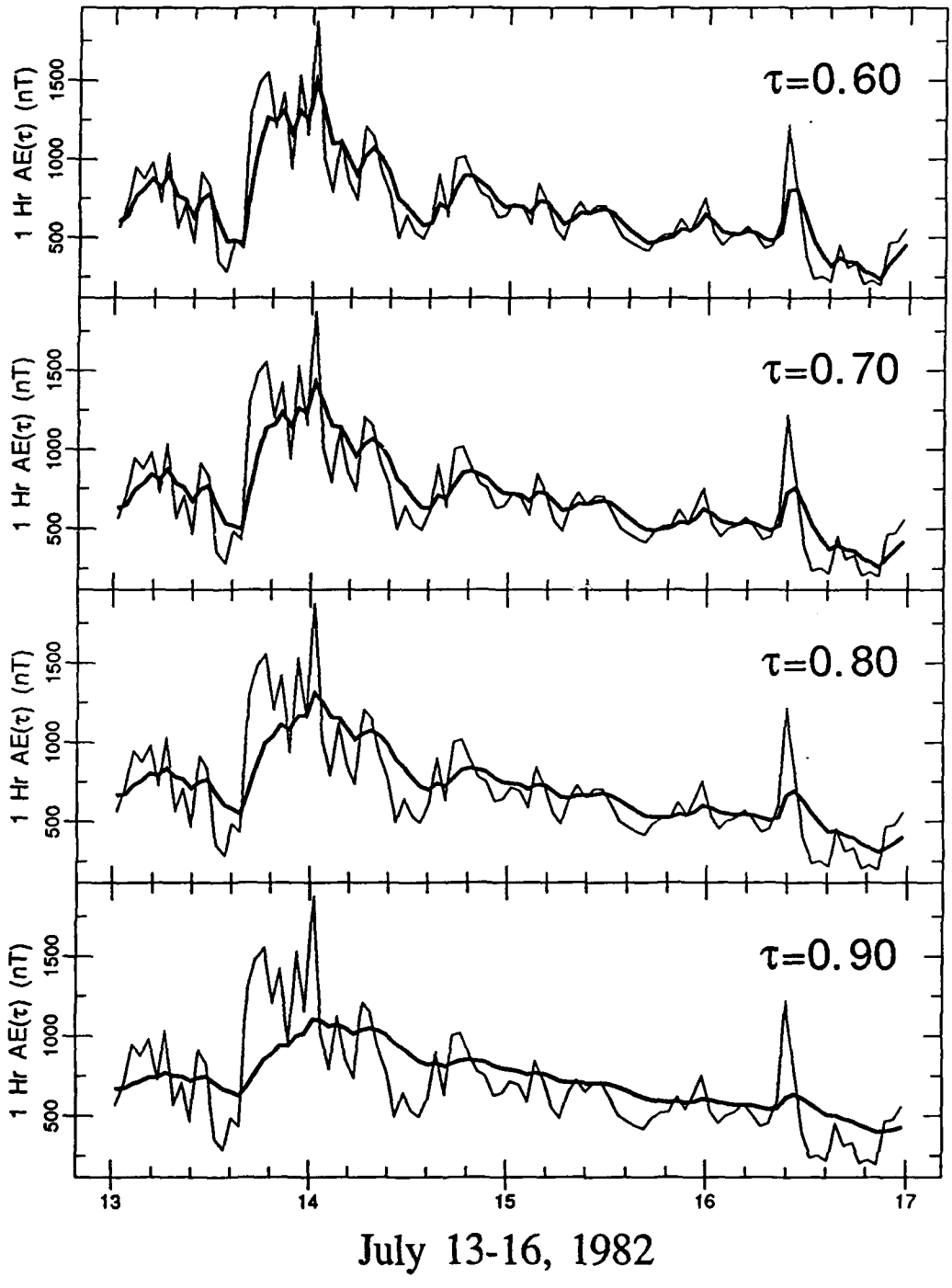

Fig. 20. Examples of time-weighted accumulations of *AE* (thin line) for τ values of 0.6, 0.7, 0.8, and 0.9 to achieve $AE(\tau)$ (bold line).

Before proceeding, a note should be made on the use of 1-hour *AE* versus 1-minute *AE*. Applying Fourier analysis to the 1-minute *AE* gives several interesting results relating to the 1-hour index. When a Fourier transform of the 1-minute index is reconstructed with the higher frequencies removed, the data becomes very close to the 1-hour index. Therefore, the 1-hour index can arguably be said to represent the lower frequency variations of the electrojets. Also, as the high-end frequency cut-off is lowered, the reconstructed index approaches that derived by simple space centered smoothing on the 1-hour index, so that this method approximates even lower frequency components of the electrojet variations. When τ weighting is applied to the 1-minute index (as well as reconstructed indices with higher frequencies removed), it is almost identical to that derived from the 1-hour *AE* index. All of these results are discussed in more detail (with examples) in Appendix B.

Correlations with Dst

Applying the two above techniques to the *AE* series of indices produced two new sets of adjusted indices, referred to as AE_{avg} (for space centered smoothing) and $AE(\tau)$ (for time-weighted accumulations). These new sets for the 21 storms were generated for 48 hours before and 72 hours after the minimum *Dst* value, then compared to *Dst*. After trial and error to determine the best values to use, the comparisons were made for 50 iterations of averaging, and τ values of 0.75 and 0.9. Plots of these for each of the storms are shown in Appendix A. Correlation coefficients were computed for each of the indices *AE*, *AL*, *AU*, and *AO* compared

to *Dst*, then each index with the averaging and τ weighing. As can be seen from the plots in Appendix A, in some cases there is an apparent time shift between the two curves. Therefore, the curves were time shifted to achieve a maximum correlation. The resulting correlation coefficients are shown in Figures 21-24, each with a histogram of the time shifts needed to achieve maximum correlation (a positive offset shifts the *AE* indices forward). The figures show that the *AO* set of indices has the best correlations, followed by *AL*, with the τ weighing of 0.9 being the best for all indices. The time shift plots demonstrate that *AE* correlates with *Dst* using a time shift centered on ~6 hours, while a τ of 0.9 reduces the time shift to near 0. Similar results are found for *AL*. The results for *AU* are less consistent, with the maximum correlation for the straight index often shifted by 24 hours (the maximum allowed), while *AO* is very consistent in being clustered near 0 for most values. The similarity of *AE* and *AL* is expected, since *AL* makes a much greater contribution than *AU*. The poorer results of *AU* can be explained by the fact that the eastward electrojet is less correlated to substorm activity and is not well understood. The good correlation of *AO* is justified since *AO* is intended to measure the zonal currents, of which the ring current is a part. *AL* should also be slightly better than *AE* since *Al* contains a ring current contribution and *AE* does not.

The most significant result is the close correlation between *Dst* and $AE(\tau)$ (ranging from 0.73 to 0.93 except for storm 3, which was 0.58) and $AL(\tau)$ (ranging from 0.78 to 0.95 except for storm 3, which was 0.67) for τ=0.9. By introducing a

time constant of ~10 hours to the *AE* and *AL* data, one can achieve very close correlations with *Dst* during intense storms.

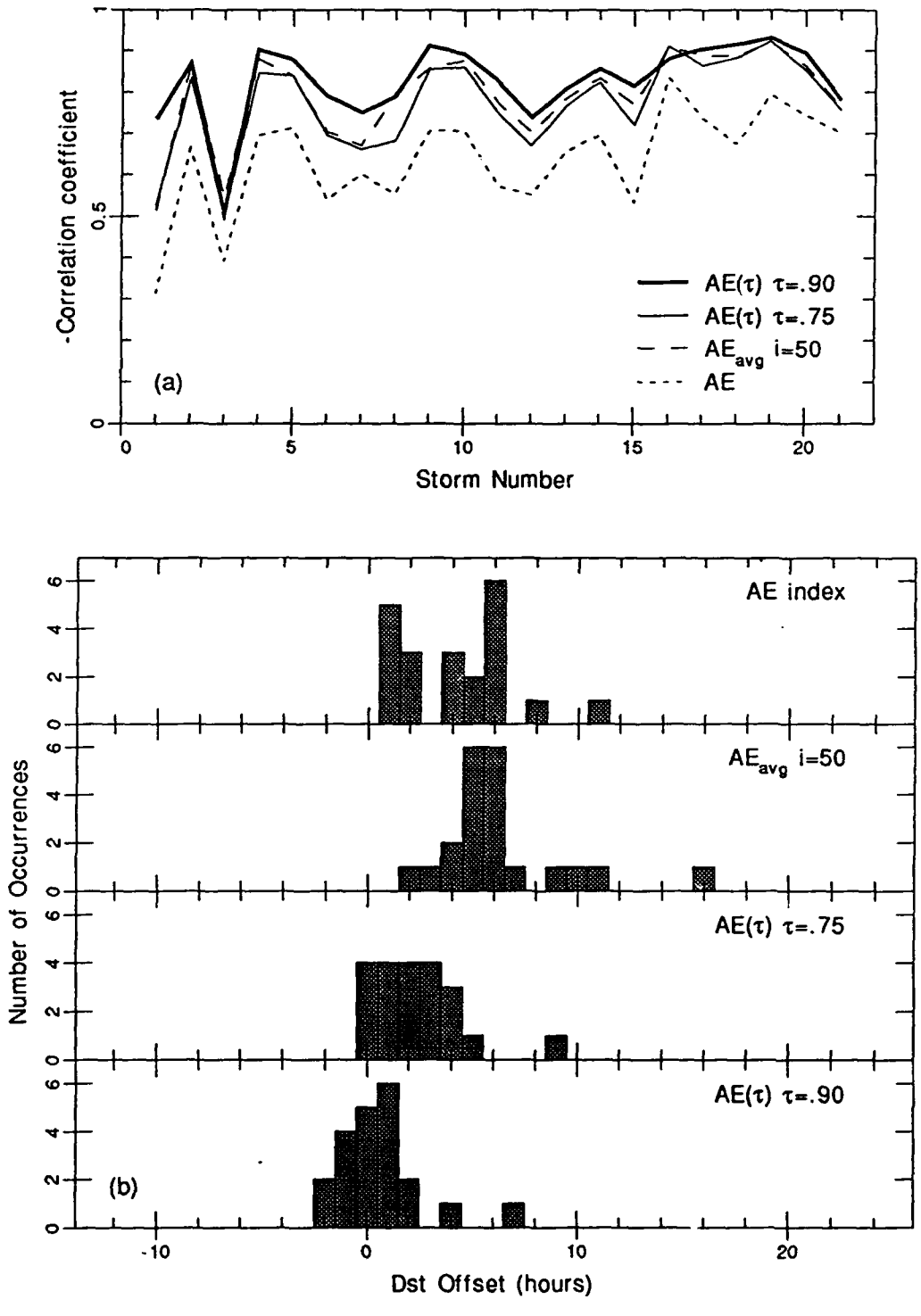

Fig. 21. Correlation coefficients (a) and time shifts needed to achieve maximum correlation (b) for AE, AE_{avg}, and $AE(\tau)$.

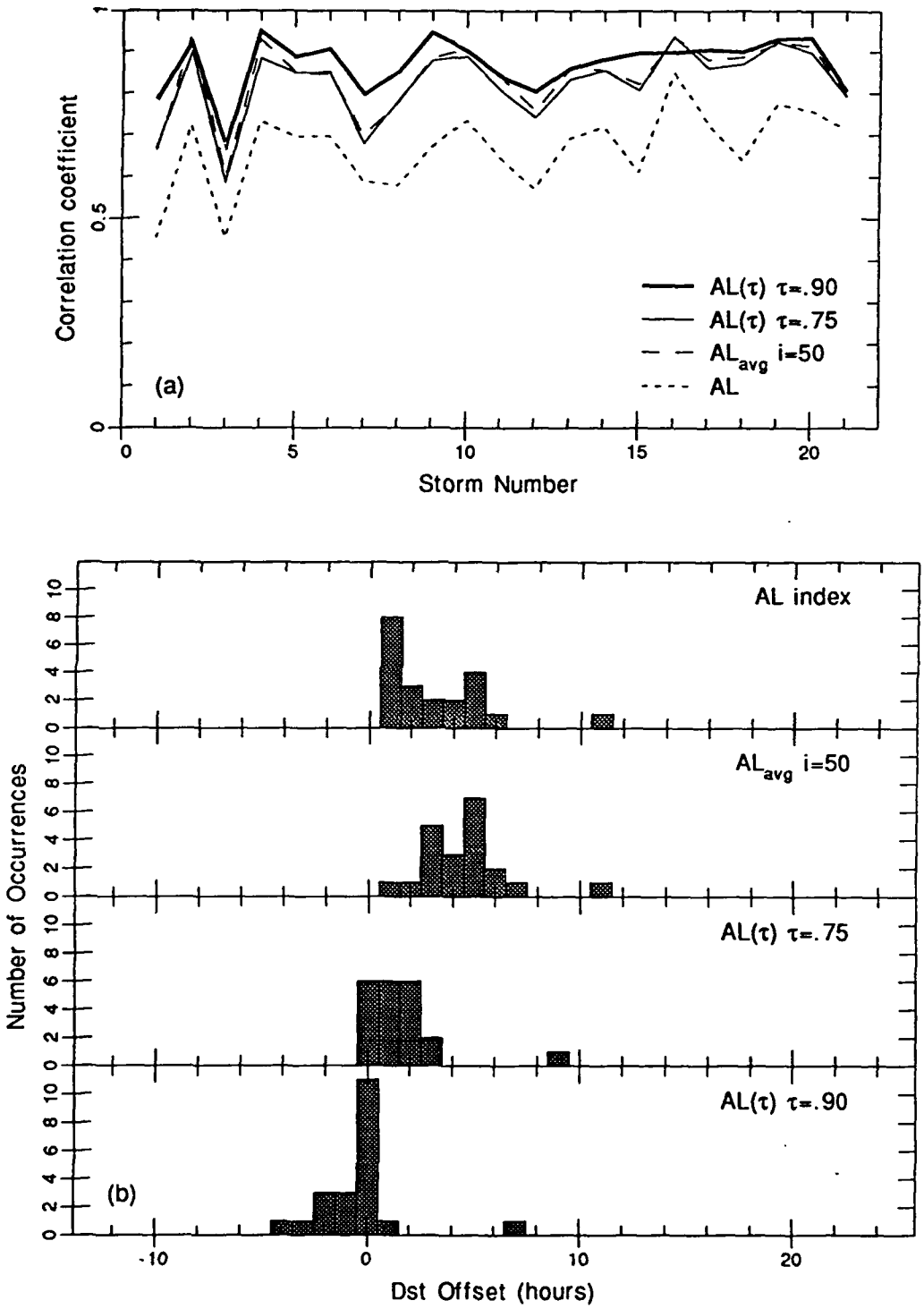

Fig. 22. Correlation coefficients (a) and time shifts needed to achieve maximum correlation (b) for AL, AL_{avg}, and $AL(\tau)$.

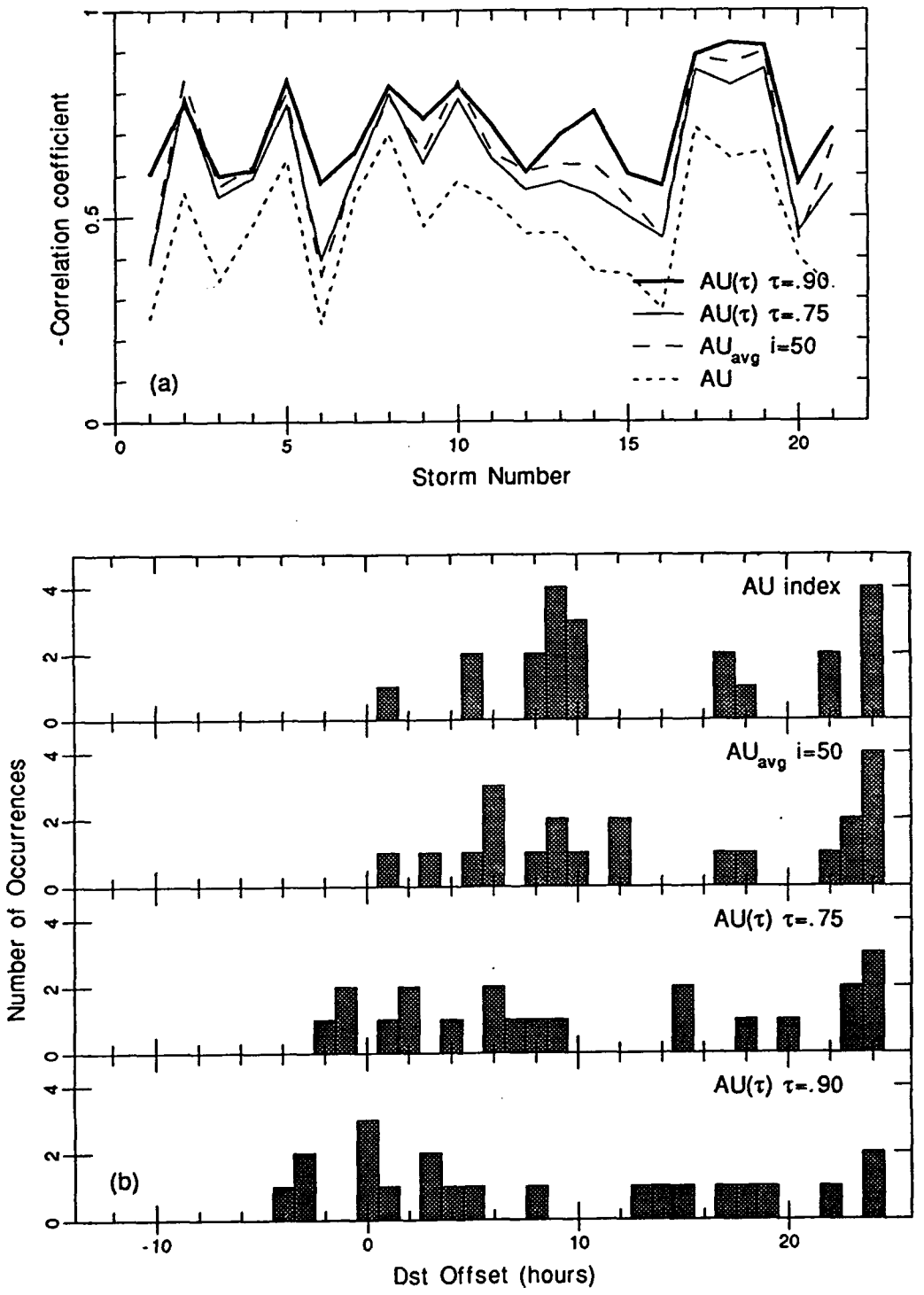

Fig. 23. Correlation coefficients (a) and time shifts needed to achieve maximum correlation (b) for AU, AU_{avg}, and $AU(\tau)$.

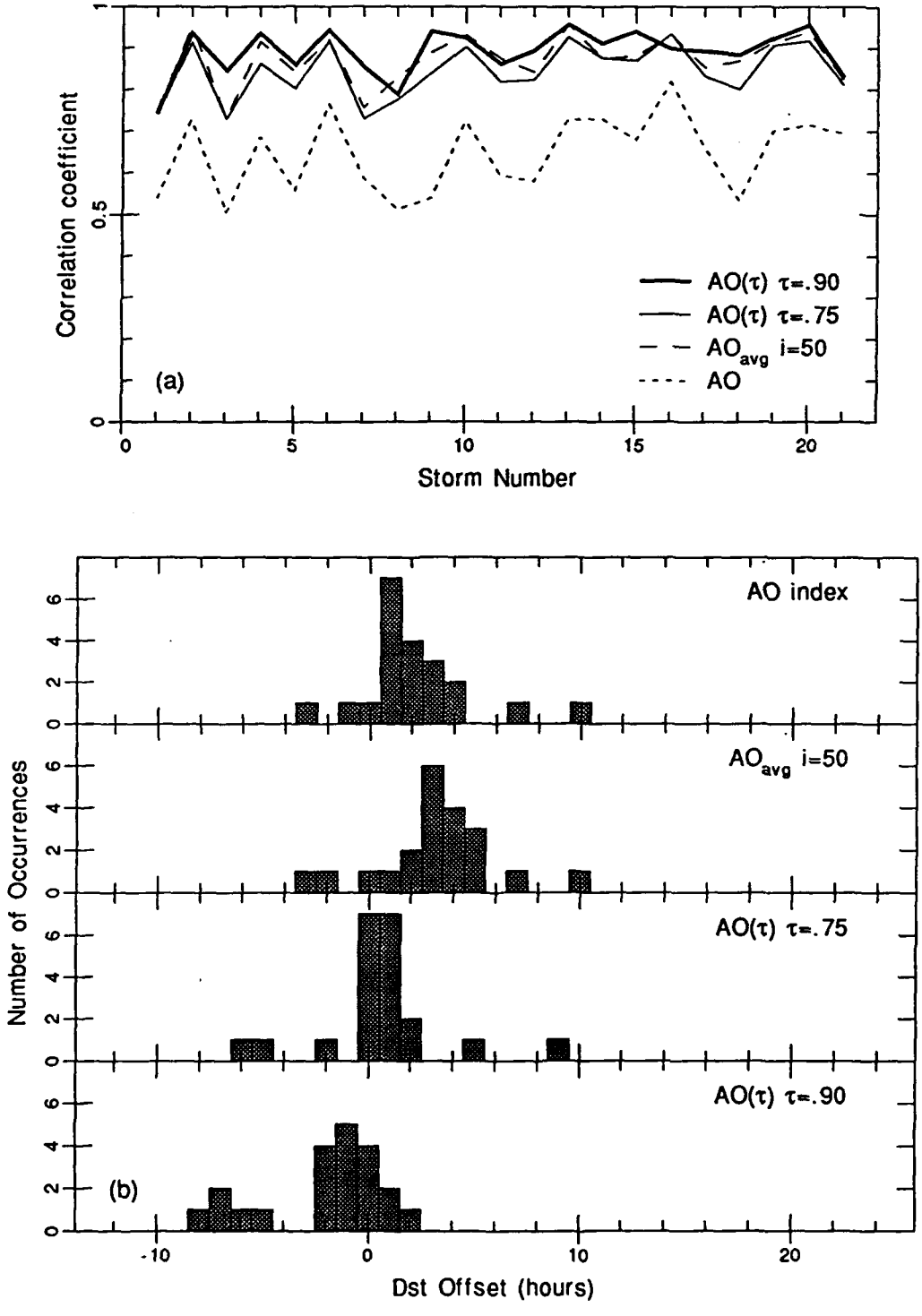

Fig. 24. Correlation coefficients (a) and time shifts needed to achieve maximum correlation (b) for AO, AO_{avg}, and $AO(\tau)$.

CHAPTER 5

DST MODELING FROM AE AND AL

Previous Modeling Efforts

Several methods for modeling *Dst* (and hence the ring current) have been developed over the past 30 years. An early effort by *Kamide and Fukushima* [1971] attempted to use *AE* times an exponential function to model the energy input into the symmetric ring current. By varying the decay time in the equation for energy change of the ring current, they were able to represent *Dst* fairly well. However, this was done for only one storm and no further work in this area was ever pursued.

Akasofu [1981b] used his ϵ parameter to model *AE* and *Dst* to show that both are directly driven by the solar wind. He achieved good agreement for a few storms and indicated the possibility of forecasting these indices from IMF measurements.

The most current methods are reviewed by *Feldstein* [1992]. All of these methods are alike in that they use IMF parameters to model *Dst*. Feldstein tested several of them and determined that the method developed by *Pisarsky et al.* [1989] was one of the best. The Pisarsky et al. method was applied to those storms of the 21 which had close to a complete set of IMF data and the results are given in Appendix C. One problem with the Pisarsky et al. method is that it requires a prior knowledge of the peak *Dst* so that it cannot model *Dst* in real time. Other methods, such as that introduced by *Burton et al.* [1975], could model *Dst* in real time if IMF

were always available. However, another difficulty is that IMF data is not always available for a storm, much less available without delay.

General Relationship Between AE/AL and Dst

Given the high correlations found between the *AE* indices and *Dst* in the previous chapter, and the close representations to the *Dst* traces shown in Appendix A, it is possible that *AE* could be used to model *Dst* and demonstrate a current system relationship, with $AE(\tau)$ and $AL(\tau)$ (with τ=0.9) being the best candidates [$AO(\tau)$ will not be considered, even though it had the best correlation, since it has a smaller lead time (see Figure 24) and would be less useful for forecasting -- it also has less physical significance]. The year 1982 was chosen for use in determining the relationship between the indices since it contained a large number of intense storms. $AE(\tau)$ and $AL(\tau)$ with τ=0.9 [afterwards referred to as $AE(90)$ and $AL(90)$] were then calculated for the entire year and compared to *Dst*. The correlation coefficients for the year were −0.751 for $AE(90)$ and 0.792 for $AL(90)$, compared to −0.571 for *AE* and 0.584 for *AL*. Figure 25 shows a scatter plot for the entire 1982 data set. It is apparent in the plot that a linear relationship exists for lower values, while an exponential function might better represent the higher values.

A least-squares fit was performed on the data points in Figure 25. Since the higher-valued, nonlinear points were relatively few, they did not affect the fitting. The resulting equations were:

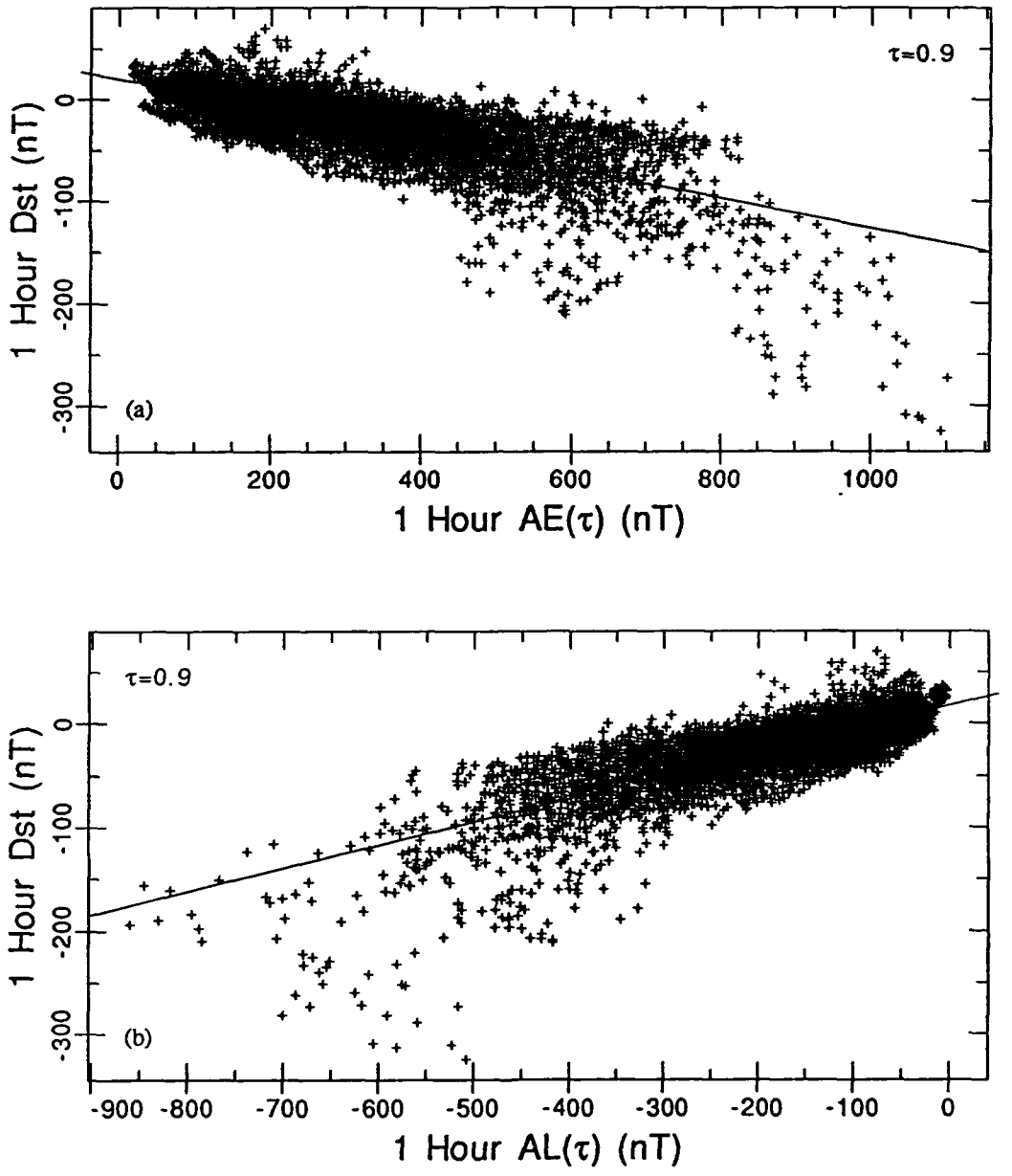

Fig. 25. Plot of *Dst* versus $AE(\tau)$ (a) and $AL(\tau)$ (b) for 1982. The line fits were determined from a least-squares method.

$$Dst(AE(90)) = [-0.147 \times AE(90)] + 20.2 \quad (4)$$

$$Dst(AL(90)) = [0.224 \times AL(90)] + 17.2 \quad (5)$$

Values of *Dst*, *AE*(90), and *AL*(90) were then taken for 65 *Dst* peaks during the year. These values were plotted on a logarithmic scale and fitted with a least-squares fit to produce the following relations:

$$Dst(AE(90)) = -13.2 \times 10^{[0.00119 \times AE(90)]} \quad (6)$$

$$Dst(AL(90)) = -13.8 \times 10^{[-0.00174 \times AL(90)]} \quad (7)$$

The peak values used and the least-squares fit are shown in Figure 26.

To use these two relationships together, it must be determined when to use each. For *AE*, the curves for the two equations intersect at *AE*(90)=450 (*Dst*=-46) and *AE*(90)=575 (*Dst*=-64), while for *AL* they intersect at *AL*(90)=-220 (*Dst*=-32) and *AL*(90)=-450 (*Dst*=-83). For both cases, the higher values were chosen since from Figure 25 the linear relation clearly holds up to those points. This results in the following composite relationships:

$$Dst(AE(90)) = [-0.147 \times AE(90)] + 20.2; \quad AE(90) \le 575 \quad (8a)$$
$$Dst(AE(90)) = -13.2 \times 10^{[0.00119 \times AE(90)]}; \quad AE(90) > 575 \quad (8b)$$

$$Dst(AL(90)) = [0.224 \times AL(90)] + 17.2; \quad AL(90) \ge -450 \quad (9a)$$
$$Dst(AL(90)) = -13.8 \times 10^{[-0.00174 \times AL(90)]}; \quad AL(90) < -450 \quad (9b)$$

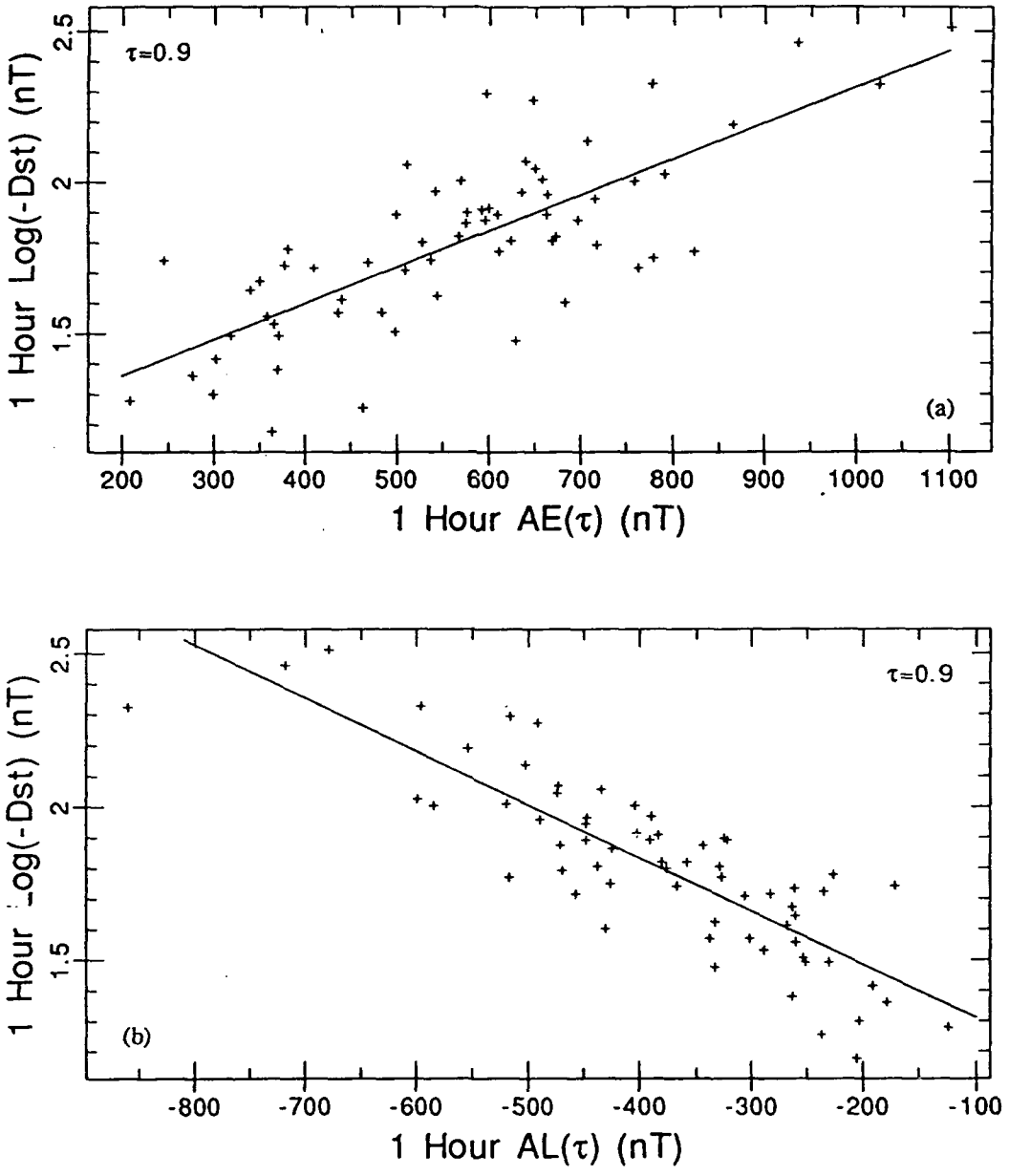

Fig. 26. Plot of 65 *Dst* peaks in 1982 versus $AE(\tau)$ (a) and $AL(\tau)$ (b) values. The line fits were determined from a least-squares method.

When equations (8) and (9) are applied to the data for 1982, the correlation coefficient for $Dst(AE(90))$ is 0.775 and for $Dst(AL(90))$ is 0.793. Monthly plots for *Dst* versus $Dst(AE(90))$ and $Dst(AL(90))$ for 1982 are in Figures 27 and 28. In these plots it can be seen that for the majority of the time, $Dst(AE(90))$ and $Dst(AL(90))$ give quite an accurate representation of *Dst*.

Since (8) and (9) were developed from the 1982 data, one would expect a reasonable correlation. To test the validity of the derived relations, (8) and (9) were applied to the other years of this study (1978-1986) and the results are given in Table 3. For most years the relationships work just as well, and for some years (1981 and 1984) they are even superior, with correlations reaching 0.8 or better.

Relationships Between AE/AL and Dst for Storms 1-21

As can be seen in Figures 27 and 28, the general relationships (8) and (9) model *Dst* quite well for most of the year. However, during intense storm periods (8) and (9) sometimes work well and other times do not. To try to determine the nature of these discrepancies, the relationships between *Dst* and $AE(90)$ and $AL(90)$ were investigated in detail for storms 1-21. The functional relationships derived are of linear or exponential form of these two types:

$$Dst = [a \times (index)] + b \tag{10}$$

$$Dst = c \times 10^{[d \times (index)]} \tag{11}$$

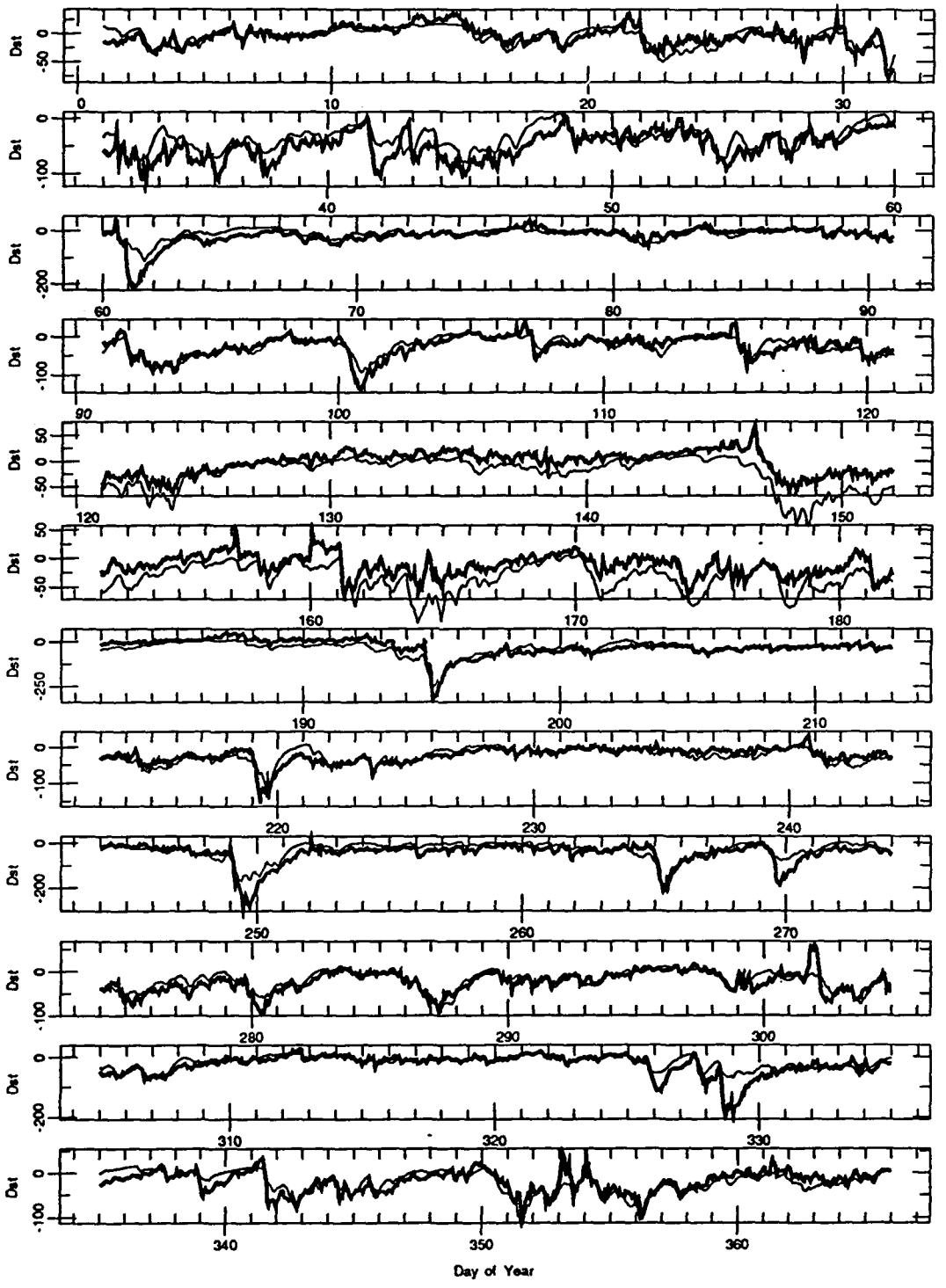

Fig. 27. *Dst* (bold) and *Dst*(*AE*(90)) for 1982. Notice that the *Dst* scale is different for each month.

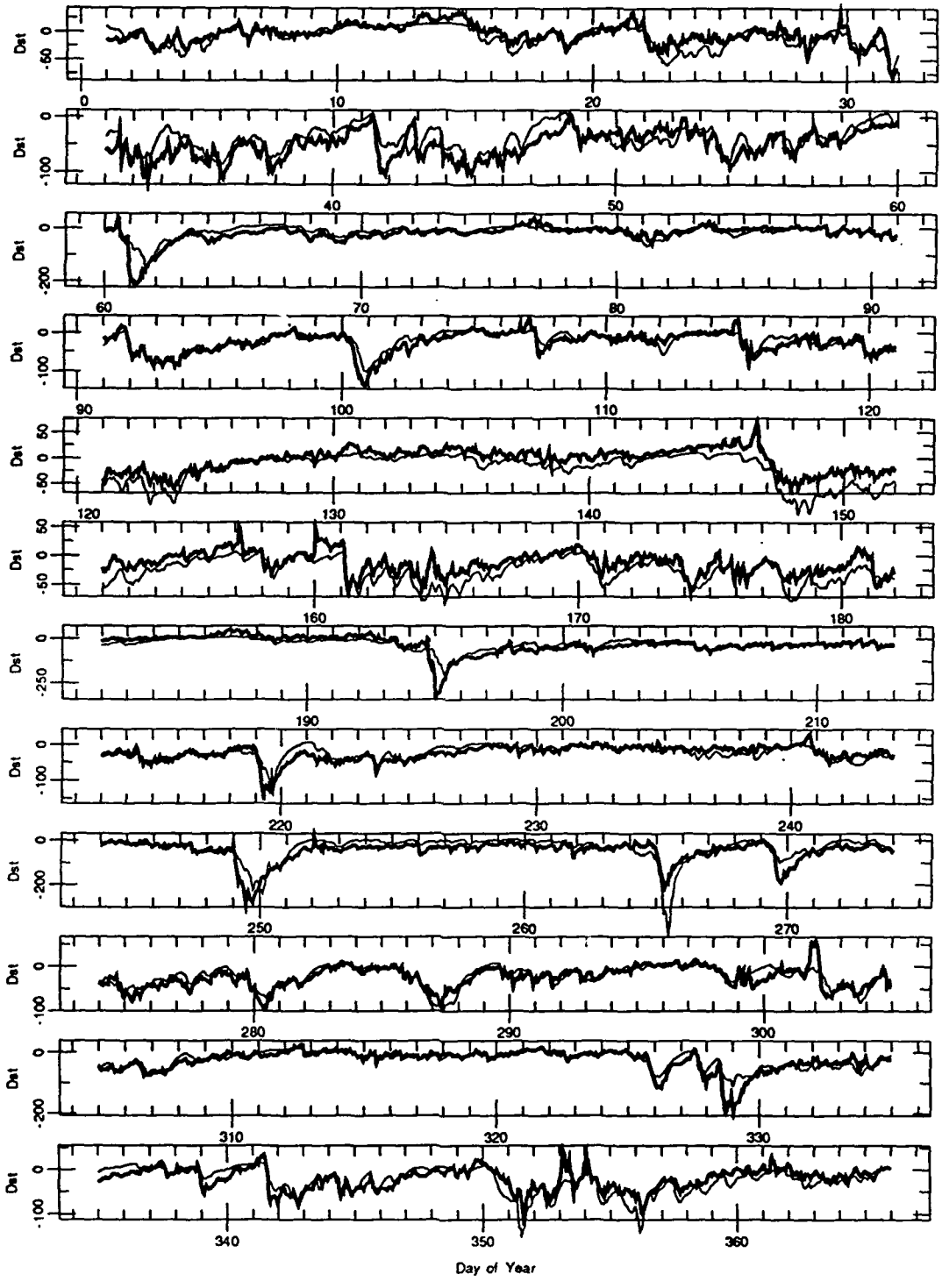

Fig. 28. *Dst* (bold) and *Dst*(*AL*(90)) for 1982. Notice that the *Dst* scale is different for each month.

Table 3. Correlation coefficients for *Dst* versus *Dst* as a function of $AE(90)$ and $AL(90)$ for the years 1978-1986.

Year	Correlation Coefficients	
	Dst(AE(90))	Dst(AL(90))
1978	0.7645	0.8012
1979	0.7032	0.7654
1980	0.7113	0.7920
1981	0.7722	0.8180
1982	0.7753	0.7927
1983	0.7224	0.7755
1984	0.8081	0.8242
1985	0.7525	0.7898
1986	0.7453	0.6050

The coefficients for these relations for each storm are shown in Table 4 and the functions are plotted in comparison to relations (8) and (9) in Figure 29. The resulting correlation coefficients are given in Table 5. Possible reasons for these functional differences are discussed in the next chapter.

Table 4. Functional relationship between *Dst* and *AE*(90)/*AL*(90) for storms 1-21.

Storm	Functional Dependence of Dst on AE(90)	Functional Dependence of Dst on AL(90)
1	eq. (8a); AE(90)≤575 eq. (11) with c=−19.6, d=.000891; AE(90)>575	eq. (9a); AL(90)≥−450 eq. (11) with c=−29.7, d=−.000992; AL(90)<−450
2	eq. (8a); AE(90)≤575 eq. (11) with c=−3.47, d=.0022; AE(90)>575	eq. (9a); AL(90)≥−450 eq. (11) with c=−9.01, d=−.00214; AL(90)<−450
3	eq. (8a); AE(90)≤575 eq. (11) with c=−1.87, d=.00267; AE(90)>575	eq. (9a); AL(90)≥−450 eq. (11) with c=−3.49, d=−.00306; AL(90)<−450
4	eq. (10) with a=−.209, b=25.1; AE(90)≤550 eq. (10) with a=−.60, b=240; AE(90)>550	eq. (10) with a=.330, b=19.8; AL(90)≥−393 eq. (10) with a=.709, b=169; AL(90)<−393
5	eq. (8a); AE(90)≤575 eq. (11) with c=−9.95, d=.00141; AE(90)>575	eq. (9a); AL(90)≥−450 eq. (11) with c=−5.19, d=−.00268; AL(90)<−450
6	eq. (10) with a=−.605, b=90.7	eq. (10) with a=.587, b=58.7
7	eq. (10) with a=−.336, b=16.8	eq. (10) with a=.434, b=17.4
8	eq. (10) with a=−.311, b=35.7; AE(90)≤546 eq. (10) with a=−1.31, b=582; AE(90)>546	eq. (10) with a=.505, b=30.2; AL(90)≥−335 eq. (10) with a=2.13, b=574; AL(90)<−335
9	eq. (8)	eq. (9)
10	eq. (10) with a=−.337, b=50.5	eq. (10) with a=.395, b=23.7
11	eq. (8a); AE(90)≤575 eq. (11) with c=−10.8, d=.00134; AE(90)>575	eq. (9a); AL(90)≥−450 eq. (11) with c=−5.68, d=−.00259; AL(90)<−450
12	eq. (8a); AE(90)≤547 eq. (11) with c=−11.7, d=0.0013; AE(90)>547	eq. (9a); AL(90)≥−300 eq. (11) with c=−13.1, d=−.00193; AL(90)<−300
13	eq. (8a); AE(90)≤575 eq. (11) with c=−5.80, d=.00181; AE(90)>575	eq. (9a); AL(90)≥−450 eq. (11) with c=−10.2, d=−.00202; AL(90)<−450
14	eq. (8)	eq. (9a); AL(90)≥−450 eq. (11) with c=−30.0, d=−.000983; AL(90)<−450
15	eq. (10) with a=−.517, b=77.6	eq. (10) with a=.474, b=28.5
16	eq. (10) with a=−.269, b=40.4	eq. (10) with a=.251, b=15.1
17	eq. (8a); AE(90)≤547 eq. (10) with a=−.0585, b=−28; AE(90)>547	eq. (9a); AL(90)≥−344 eq. (10) with a=.080, b=−32.8; AL(90)<−334
18	eq. (10) with a=−.102, b=15.2	eq. (10) with a=.129, b=7.75
19	eq. (8)	eq. (9a); AL(90)≥−450 eq. (11) with c=−33.8, d=−.000869; AL(90)<−450
20	eq. (8)	eq. (9a); AL(90)≥−450 eq. (11) with c=−29.1, d=−.00101; AL(90)<−450
21	eq. (10) with a=−.11, b=−38; AE(90)≤1205 eq. (10) with a=−1.9, b=2120; AE(90)>1205	eq. (10) with a=.155, b=−17.3; AL(90)≥−1165 eq. (10) with a=2.01, b=2242; AL(90)<−1165

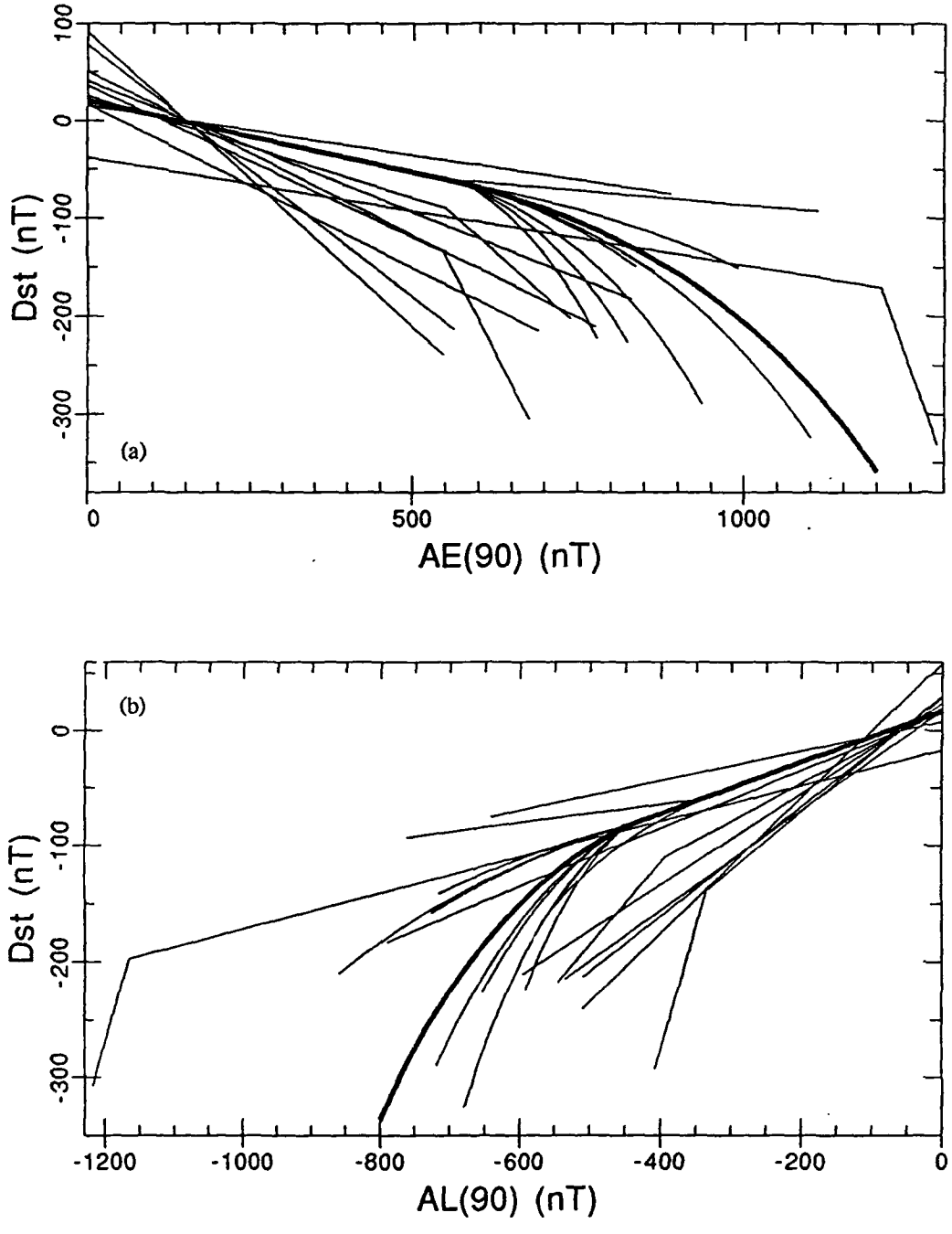

Fig. 29. The relationships for *Dst* as a function of *AE*(90) (a) and *AL*(90) (b). The general relationships from equations (8) and (9) are bold and the relationships for storms 1-21 are thin.

Table 5. Correlation coefficients for *Dst* versus *Dst*(*AE*(90)) and *Dst*(*AL*(90)) for storms 1-21.

Storm	Corr. Coeff. for Dst(AE(90))	Corr. Coeff. for Dst(AL(90))
1	0.711	0.779
2	0.845	0.895
3	0.711	0.799
4	0.925	0.960
5	0.897	0.897
6	0.790	0.905
7	0.745	0.797
8	0.768	0.884
9	0.931	0.944
10	0.881	0.879
11	0.883	0.768
12	0.755	0.799
13	0.919	0.852
14	0.906	0.897
15	0.795	0.896
16	0.869	0.886
17	0.939	0.943
18	0.908	0.888
19	0.892	0.910
20	0.911	0.931
21	0.777	0.816

CHAPTER 6

DISCUSSION

Results of Dst-AE Comparisons

The results of Chapter 4 seem to show that during storms there is a clear relationship between the ring current and electrojets. Both are energized by the same source and are primarily directly driven. While most researchers use the 1-hour *AE* index regularly to track substorm activity, FFT analysis (see Appendix B) shows (and *Fairfield* [1992] agrees) that the 1-hour *AE* is primarily directly driven, especially since the actual substorm component from cross-tail current disruption has a higher frequency (*Lee et al.* [1985]; *Liu et al.* [1988]; and L. Zhu, private communication, 1993). This is justified by the result of AE_{avg} (and AL_{avg}) giving a better correlation than *AE* (and *AL*) since the smoothing technique was shown to be equivalent to removing higher frequencies. It is more likely that the 1-hour *AE* index contains primarily the directly driven component of the auroral currents and very little (if any) loading-unloading (substorm) component (this view is supported by *Fairfield* [1992]). This would explain the disagreement of those who claim that substorms are directly driven (i.e., *Akasofu* [1981a]) by comparison with the solar wind (since the solar wind components used drive magnetospheric convection) and those who claim that a substorm has both directly driven and loading-unloading components based on magnetic reconnection and plasmoid observations (i.e., *McPherron* [1991] and references therein).

From this, then, one can assume that when the IMF turns southward, plasma flow due to convection increases and reaches some steady-state value, and this is reflected in the elevated *AE* level. As magnetic reconnection and current disruption occur in the magnetotail, substorms occur and are superposed on the baseline (as stated by Lee et al. and Liu et al.) but are of little additional influence on the 1-hour *AE* (see Appendix B where τ applied to the 1-minute *AE* is roughly equal to τ applied to the 1-hour *AE*), so the 1-hour *AE* continues to reflect the directly driven baseline value. At the same time, the ring current is being energized by the increased convection and is also directly driven. This continues until the IMF turns northward and the enhanced activity returns to quiet levels.

With this picture in mind the results of using the τ weighting on the *AE* indices are understandable, since 1-hour *AE* and *Dst* are both measuring a directly driven current (driven by the same source) that differ only by how the currents respond to injection (this is also supported by the work of *Kamide and Fukushima* [1971]). The time-weighted accumulation method is equivalent to simulating the *AE* current injection as an injection into another current system with a slower response time. The result is that the new indices derived from τ=0.9 bear a very close resemblance to the *Dst* index, indicating that the theoretical picture outlined above has some degree of authenticity.

While $AU(\tau)$ did not correlate well to *Dst*, its inclusion in $AE(\tau)$ did not cause a significant reduction in the correlation of $AE(\tau)$. Although it could be argued that *AU* contributes much less to *AE* and is not as much of a factor, it could also be

argued that the eastward electrojet closes through the partial ring current (*Kamide and Fukushima* [1971]) and so should be included in the analysis since the partial ring current contributes to *Dst*.

Modeling Dst from AE(τ) and AL(τ)

Extending the above comparisons for τ=0.9 to an entire year of data demonstrated the possibility that *Dst* could actually be modeled or forecasted from *AE*(90) and *AL*(90). The fact that the derived *Dst* followed the actual *Dst* very closely at low values shows that even during a quieter period the current systems are closely tied together in their source, indicating that the above relationship between the current systems is a permanent one.

Even though the initial comparisons of *Dst* to *AE*(90) and *AL*(90) for storms showed some similarity, different functional relationships between *Dst* and *AE*(90) and *Dst* and *AL*(90) were found for many of the storms, although many of the relationships were very similar to the original relationships (8) and (9). This indicates the possibility that some other physical process is not being included during storm periods, which makes the relationships different. While there could be a variety of other factors to consider, an initial analysis of the data showed no dependence on solar cycle or season. The different relationships could also suggest a deficiency in the measurement of the current systems, which is possible given all the inadequacies already noted in Chapter 3.

Although the general relationships (8) and (9) work very well in spite of the many problems with the indices, it is useful to speculate on the reasons why they do not work better:

1) While the partial ring current may or may not be reflected in the *AU* index, it no doubt has a different time constant (as shown by Kamide and Fukushima) than the symmetric ring current. It would therefore reduce the relationship between *Dst* and $AE(\tau)/AL(\tau)$ using a τ that fits the symmetric ring current.

2) During the first few hours of ring current energization, the ring current cannot be symmetric; therefore, that assumption about the *Dst* index is no longer valid.

3) The *AE* stations are not always in position to measure the full intensity of the electrojets so that measurements are missing that would change the character of $AE(\tau)$.

4) The application of τ to the *AE* indices means that one time constant is chosen and remains constant, while most ring current researchers have established that the time constant of ring current decay changes during the course of most storms.

5) The effect of magnetospheric compression is not removed from *Dst* so that the ring current is not always the only current being measured.

6) It is possible that electrojet effects are included in the ring current, especially during intense storms when the electrojet moves equatorward.

7) It is possible, as *Akasofu et al.* [1983] stated, that *AE* becomes saturated during intense storms and is not really representing the electrojets, although no evidence of this is found.

CHAPTER 7

CONCLUSIONS AND FURTHER RESEARCH

Conclusions

The conclusions that can be drawn from the discussion in the previous chapter are summarized as follows:

1) The 1-hour *AE* indices are totally (or nearly so) directly driven in that they contain almost no contribution from the substorm current wedge. This would resolve the apparent conflict between those researchers who argue that substorms are directly driven versus those who say that substorms have both a directly driven and a loading-unloading component.

2) A time-weighted accumulations method applied to the 1-hour *AE* indices gives a high correlation to 1-hour *Dst* during intense storms.

3) The time-weighted accumulation results show a close relationship between the ring current and the electrojets, with a difference of only response time to injection.

4) Most of the time there is a clear one-to-one relationship between *Dst* and *AE*(90)/*AL*(90). During storms this relationship may change but one still exists. The reason for the changing relationship remains to be explored.

5) The possibility exists of modeling *Dst* in real time if *AE* data is available. The U. S. Air Force is currently developing a chain of magnetometer stations which

would provide real-time *Kp* data with 15-minute resolution. This could easily be configured to provide an estimate of the *AE* indices from the magnetometer data.

The main thrust of magnetospheric research for the past 25 years has been in the area of substorms, with the belief that this would in turn lead to a better understanding of storms (i.e., the ring current). These results seem to suggest that this notion may be somewhat misguided in that substorms make very little contribution to the overall auroral current system, which has already been greatly enhanced. These enhanced background currents are the ones that show a direct relationship to *Dst* (and hence the ring current) during a storm, while the short-term fluctuations from the substorm current wedge are left out of the picture entirely.

Areas For Further Research

Some possible areas to pursue in connection with this research are:

1) Finding the physical mechanism responsible for the different functional relationships between *Dst* and *AE*(90)/*AL*(90) during intense storms.

2) Adjusting τ to maximize correlations. Although τ=0.9 was found to give the best overall results, different values of τ worked better for some storms. A different τ for each storm would undoubtedly produce better correlations.

3) Varying τ throughout the storm to maximize correlations. This would be an extension of the previous topic and would parallel the work of most researchers who model *Dst* from IMF data and use a variable decay parameter (i.e., the methods reviewed by *Feldstein* [1992]).

7) It is possible, as *Akasofu et al.* [1983] stated, that *AE* becomes saturated during intense storms and is not really representing the electrojets, although no evidence of this is found.

CHAPTER 7

CONCLUSIONS AND FURTHER RESEARCH

Conclusions

The conclusions that can be drawn from the discussion in the previous chapter are summarized as follows:

1) The 1-hour *AE* indices are totally (or nearly so) directly driven in that they contain almost no contribution from the substorm current wedge. This would resolve the apparent conflict between those researchers who argue that substorms are directly driven versus those who say that substorms have both a directly driven and a loading-unloading component.

2) A time-weighted accumulations method applied to the 1-hour *AE* indices gives a high correlation to 1-hour *Dst* during intense storms.

3) The time-weighted accumulation results show a close relationship between the ring current and the electrojets, with a difference of only response time to injection.

4) Most of the time there is a clear one-to-one relationship between *Dst* and *AE*(90)/*AL*(90). During storms this relationship may change but one still exists. The reason for the changing relationship remains to be explored.

5) The possibility exists of modeling *Dst* in real time if *AE* data is available. The U. S. Air Force is currently developing a chain of magnetometer stations which

REFERENCES

Akasofu, S. I., The development of the auroral substorm, *Planet. Space Sci.*, *12*, 273, 1964.

Akasofu, S. I., *Physics of Magnetospheric Substorms*, D. Reidel, Boston, 1977.

Akasofu, S. I., Energy coupling between the solar wind and the magnetosphere, *Space Sci. Rev.*, *28*, 121, 1981a.

Akasofu, S. I., Prediction of development of geomagnetic storms using the solar wind-magnetosphere energy coupling function ϵ, *Planet. Space Sci.*, *29*, 1151, 1981b.

Akasofu, S. I., Relationships between the AE and Dst indices during geomagnetic storms, *J. Geophys. Res.*, *86*, 4820, 1981c.

Akasofu, S. I., B. H. Ahn, Y. Kamide, and J. H. Allen, A Note on the accuracy of the auroral electrojet indices, *J. Geophys. Res.*, *88*, 5769, 1983.

Axford, W. I., Viscous interaction between the solar wind and the Earth's magnetosphere, *Planet. Space Sci.*, *12*, 45, 1964.

Baker, D. N., R. C. Anderson, R. D. Zwickl, and J. A. Slavin, Average plasma and magnetic field variations in the distant magnetotail associated with near-earth substorm effects, *J. Geophys. Res.*, *92*, 71, 1987.

Baumjohann, W., Merits and limitations of the use of geomagnetic indices in solar wind-magnetosphere coupling studies, In *Solar Wind-Magnetosphere Coupling*, edited by Kamide, Y., and J. A. Slavin, 3-15, Terra Scientific Publishing, Tokyo, 1986.

Berthelier, A., Influence of the polarity of the interplanetary magnetic field on the annual and diurnal variations of magnetic activity, *J. Geophys. Res.*, *81*, 4546, 1976.

Birn, J. and M. Hesse, MHD simulations of magnetic reconnection in a skewed three-dimensional tail configuration, *J. Geophys. Res.*, *96*, 23, 1991.

Burton, R. K., R. L. McPherron, and C. T. Russell, An empirical relationship between interplanetary conditions and Dst, *J. Geophys. Res.*, *80*, 4204, 1975.

Chapman, S. and J. Bartels, *Geomagnetism, Vol. 2*, Clarendon Press, Oxford, 1940.

Chatfield, C., *The Analysis of Time Series: Theory and Practice*, Chapman and Hall, London, 1975.

Cladis, J. B. and W. E. Francis, The polar ionosphere as a source of the storm time ring current, *J. Geophys. Res.*, *90*, 3465, 1985.

Clauer, C. R. and R. L. McPherron, Mapping the local time-universal time development of magnetospheric substorms using mid-latitude magnetic observations, *J. Geophys. Res.*, *79*, 2811, 1974.

Coroniti, F. V., Explosive tail reconnection: the growth and expansion phases of magnetospheric substorms, *J. Geophys. Res.*, *90*, 7427, 1985.

Cowley, S. W. H., The causes of convection in the Earth's magnetosphere: a review of developments during the IMS, *Rev. Geophys. Space Phys.*, *20*, 531, 1982.

Data Book 21, WDC-C2 for Geomagnetism, Kyoto, Japan, 1992.

Davis, T. N. and R. Parthasarathy, The relationship between polar magnetic activity Dp and growth of the geomagnetic ring current, *J. Geophys. Res.*, *72*, 5825, 1967.

Davis, T. N. and M. Sugiura, Auroral electrojet activity index AE and its universal time variations, *J. Geophys. Res.*, *71*, 785, 1966.

Dungey, J. W., Interplanetary magnetic field and the auroral zones, *Phys. Res. Lett.*, *6*, 47, 1961.

Fairfield, D. H., Advances in magnetospheric storm and substorm research: 1989-1991, *J. Geophys. Res.*, *97*, 10865, 1992.

Feldstein, Y. I., Modeling of the magnetic field of magnetospheric ring current as a function of interplanetary medium parameters, *Space Sci. Rev.*, *59*, 85, 1992.

Hones, E. W. Jr, Substorm processes in the magnetotail: comments on 'On hot tenuous plasmas, fireballs, and boundary layers in the Earth's magnetotail' by L. A. Frank, K. L. Ackerson, and R. P. Lepping, *J. Geophys. Res.*, *82*, 5633, 1977.

Hones, E. W. Jr, D. N. Baker, S. J. Bame, W. C. Feldman, J. T. Gosling, D. J. McComas, R. D. Zwickl, J. A. Slavin, E. J. Smith, and B. T. Tsurutani, Structure of the magnetotail at 220 Re and its response to geomagnetic activity, *Geophys. Res. Lett.*, *11*, 5, 1984.

Kamide, Y. and N. Fukushima, Analysis of magnetic storms with DR-indices for equatorial ring current field, *Rep. Ionosph. Space Res. Japan, 25*, 125, 1971.

Kertz, W., Ring current variations during the IGY, *Ann. Int. Geophys. Year, 35*, 49, 1964.

Knecht, D. J. and B. M. Shuman, The geomagnetic field, In *Handbook of Geophysics and the Space Environment*, edited by A. S. Jursa, Chapter 4, 4-1 to 4-37, Air Force Geophysics Laboratory, United States Air Force, 1985.

Lee, L. C., Z. F. Fu, and S. I. Akasofu, A simulation study of forced reconnection processes and magnetospheric storms and substorms, *J. Geophys. Res., 90*, 10896, 1985.

Liu, Z. X., L. C. Lee, C. Q. Wei, and S. I. Akasofu, Magnetospheric substorms: an equivalent circuit approach, *J. Geophys. Res., 93*, 7366, 1988.

Lyons, L. R. and M. Schultz, Access of energetic particles to stormtime ring current through enhanced radial diffusion, *J. Geophys. Res., 94*, 5491, 1989.

Mayaud, P. N., *Derivation, Meaning, and Use of Geomagnetic Indices*, Geophysical Monograph 22, AGU Washington DC, 1980.

McDiarmid, I. B., J. R. Burrows, and M D. Wilson, Comparison of magnetic field perturbations and solar electron profiles in the polar cap, *J. Geophys. Res., 85*, 1163, 1980.

McPherron, R. L., Magnetospheric substorms, *Rev. Geophys. Space Phys., 17*, 657, 1979.

McPherron, R. L., Physical processes producing magnetospheric substorms and magnetic storms, In *Geomagnetism, Vol. 4*, edited by J. A. Jacobs, Chapter 7, 593-739, Academic Press, London, 1991.

Ness, N. F., The Earth's magnetotail, *J. Geophys. Res., 70*, 2989, 1965.

Nishida, A., S. J. Bame, D. N. Baker, G. Gloeckler, M. Scholer, E. J. Smith, T. Teresawa, and B. Tsurutani, Assessment of the boundary layer model of the magnetospheric substorm, *J. Geophys. Res., 93*, 5579, 1988.

Pisarsky, V. Y., Y. I. Feldstein, N. M. Rudneva, and A. Prigancova, Ring current and interplanetary medium parameters, *Studia Geophys. Geod., 33*, 61, 1989.

Rangarajan, G. K., Indices of geomagnetic activity, In *Geomagnetism, Vol. 3*, edited by J. A. Jacobs, Chapter 5, 323-384, Academic Press, London, 1989.

Russell, C. T. and R. L. McPherron, The magnetotail and substorms, *Space Sci. Rev.*, *11*, 111, 1972.

Schindler, K. A., A theory of substorm mechanism, *J. Geophys. Res.*, *79*, 2803, 1974.

Scholer, M. and R. Hautz, On acceleration of plasmoids in magnetohydrodynamic simulations of magnetotail reconnection, *J. Geophys. Res.*, *96*, 3581, 1991.

Siscoe, C. L., Energy coupling between region 1 and 2 Birkeland current systems, *J. Geophys. Res.*, *87*, 5124, 1982.

Slavin, J. A., D. N. Baker, J. D. Craven, R. C. Elphic, D. H. Fairfield, L. A. Frank, A. B. Galvin, W. J. Hughs, R. H. Manka, D. G. Mitchell, I. G. Richardson, T. R. Sanderson, D. J. Sibeck, E. J. Smith, and R. D. Zwickl, CDAW 8 observations of plasmoid signatures in the geomagnetic tail: An assessment, *J. Geophys. Res.*, *94*, 15153, 1989.

Stern, D. P. and I. I. Alexeev, Where do field lines go in the quiet magnetosphere?, *Rev. of Geophys.*, *26*, 782, 1988.

Sugiura, M., Hourly values of equatorial Dst for the IGY, *Ann. Int. Geophys. Year*, *35*, 9, 1964.

Tascione, T. F., *Introduction to the Space Environment*, Orbit Book Company, Malabar, Florida, 1988.

Voigt, G. H. and R. A. Wolf, Quasi-static MHD processes and the "ground state" of the magnetosphere, *Rev. of Geophys.*, *26*, 823, 1988.

Wrenn, G. L., Time-weighted accumulations ap(τ) and Kp(τ), *J. Geophys. Res.*, *92*, 10125, 1987.

Wrenn, G. L., Persistence of the ring current, 1958-1984, *Geophys. Res. Lett.*, *16*, 891, 1989.

APPENDICES

APPENDIX A. STORM PLOTS

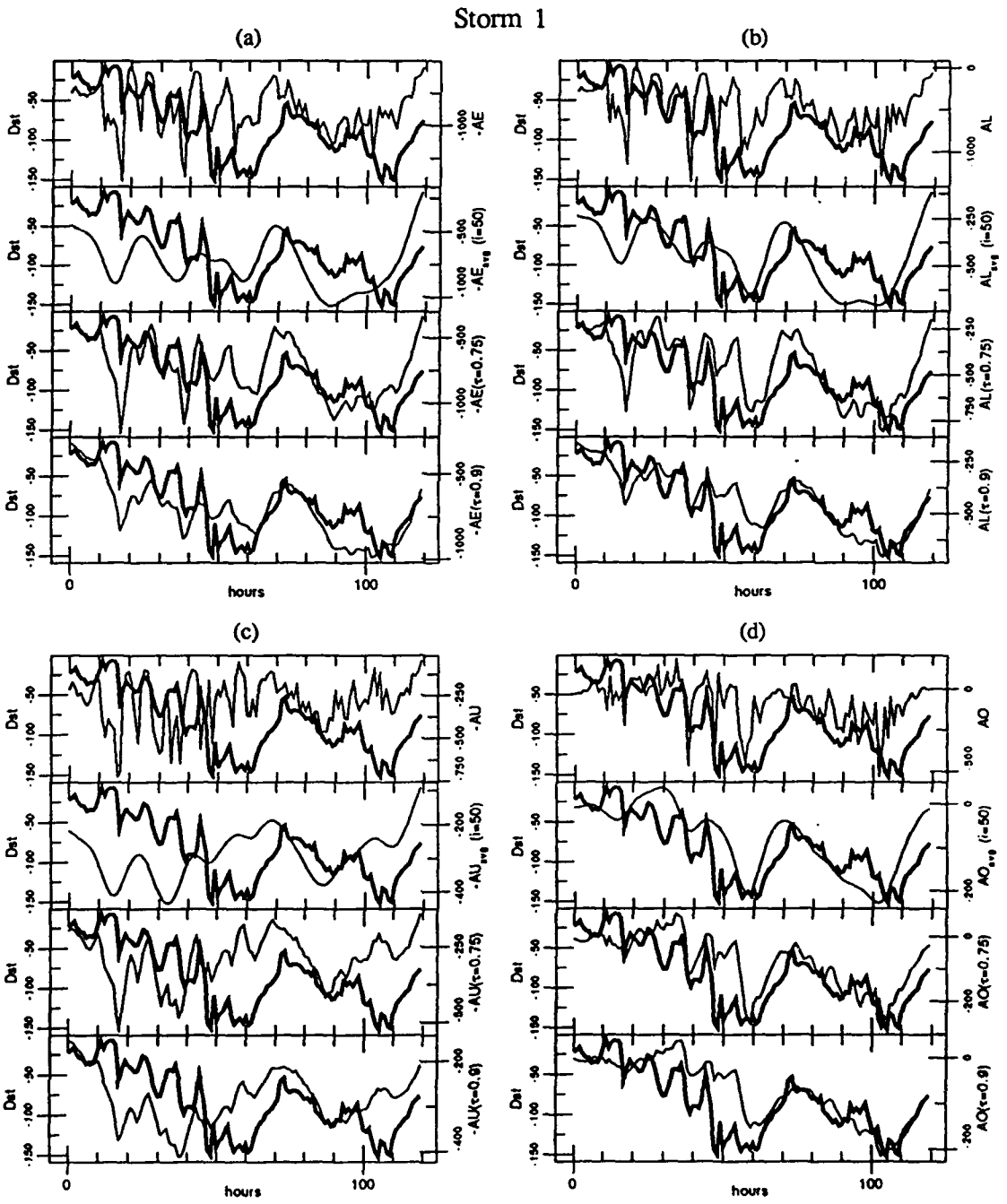

Fig. A.1. Plots for storm 1. *Dst* (bold) is plotted versus AE, AE_{avg}, $AE(\tau=0.75)$, and $AE(\tau=0.9)$ (a). The same is done for AL (b), AU (c), and AO (d).

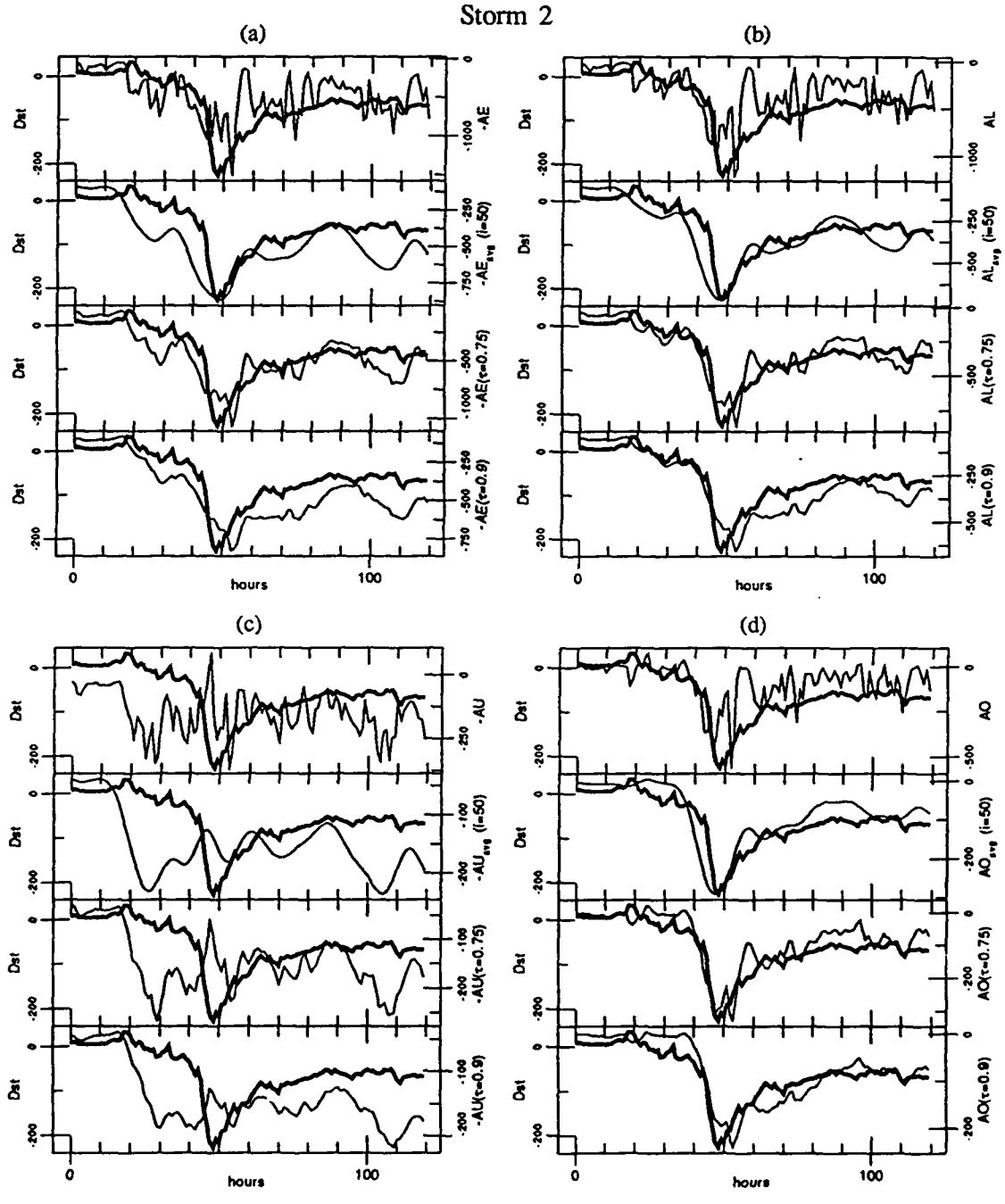

Fig. A.2. Plots for storm 2. *Dst* (bold) is plotted versus AE, AE_{avg}, $AE(\tau=0.75)$, and $AE(\tau=0.9)$ (a). The same is done for AL (b), AU (c), and AO (d).

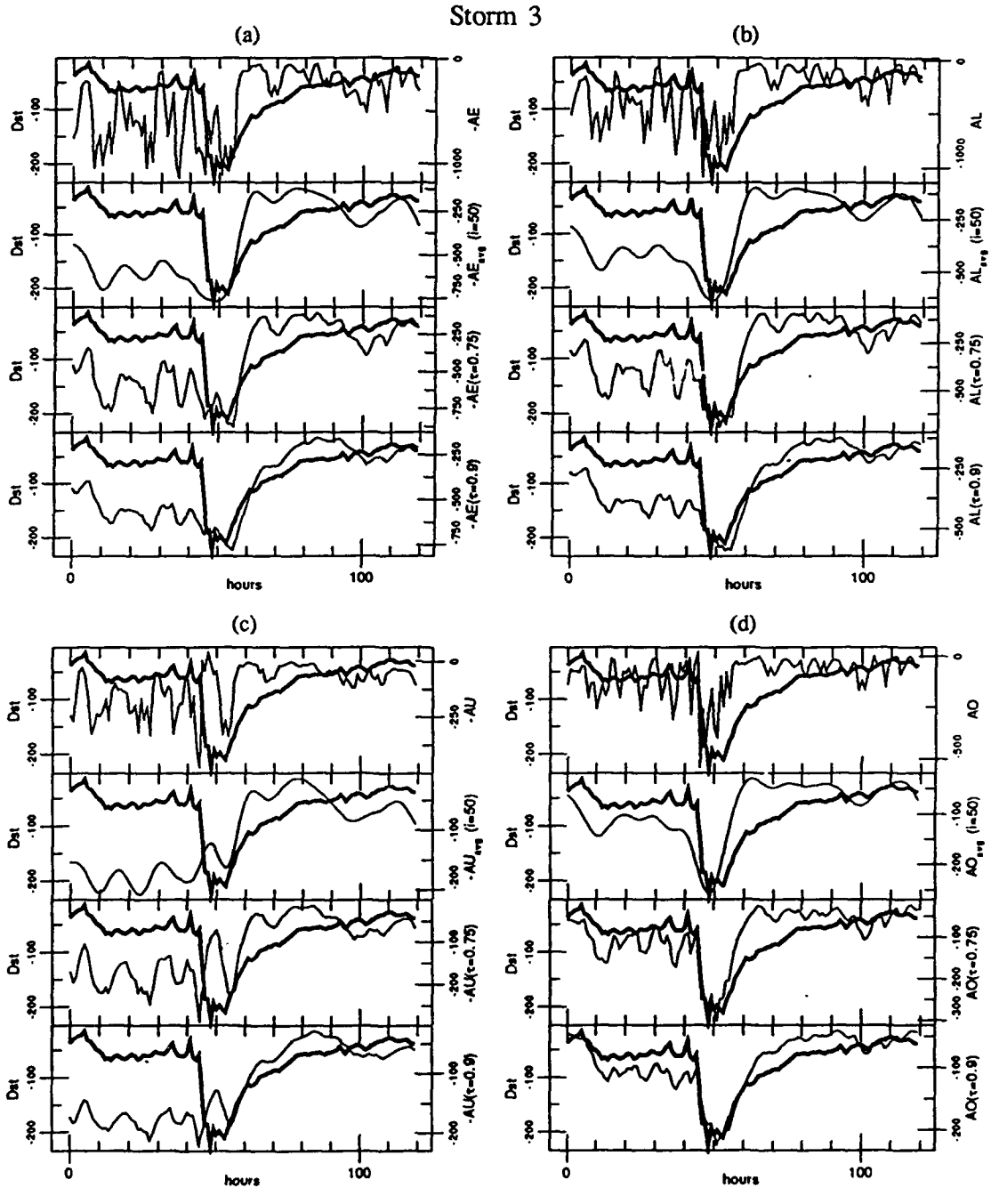

Fig. A.3. Plots for storm 3. *Dst* (bold) is plotted versus AE, AE_{avg}, $AE(\tau=0.75)$, and $AE(\tau=0.9)$ (a). The same is done for AL (b), AU (c), and AO (d).

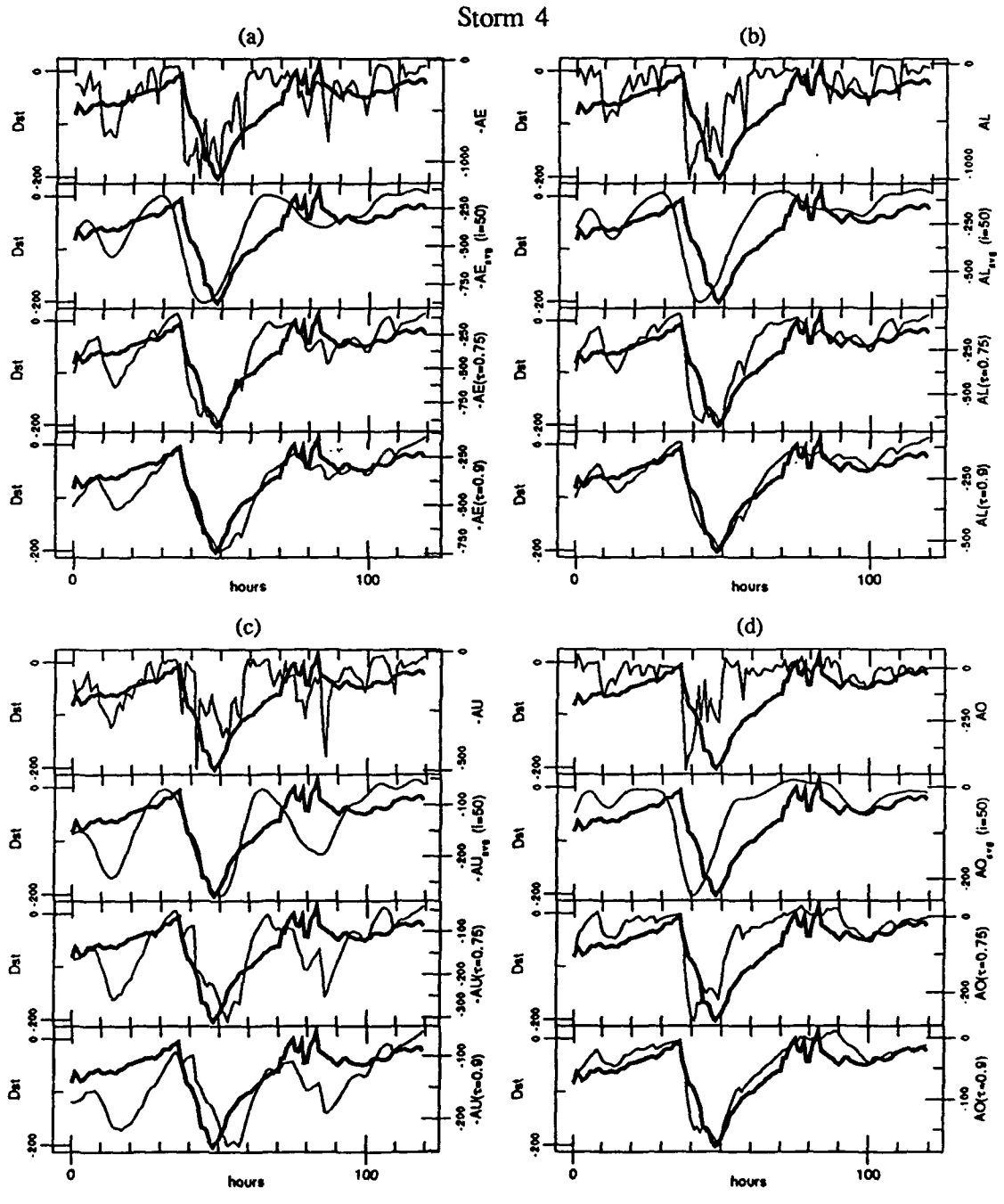

Fig. A.4. Plots for storm 4. *Dst* (bold) is plotted versus *AE*, AE_{avg}, $AE(\tau=0.75)$, and $AE(\tau=0.9)$ (a). The same is done for *AL* (b), *AU* (c), and *AO* (d).

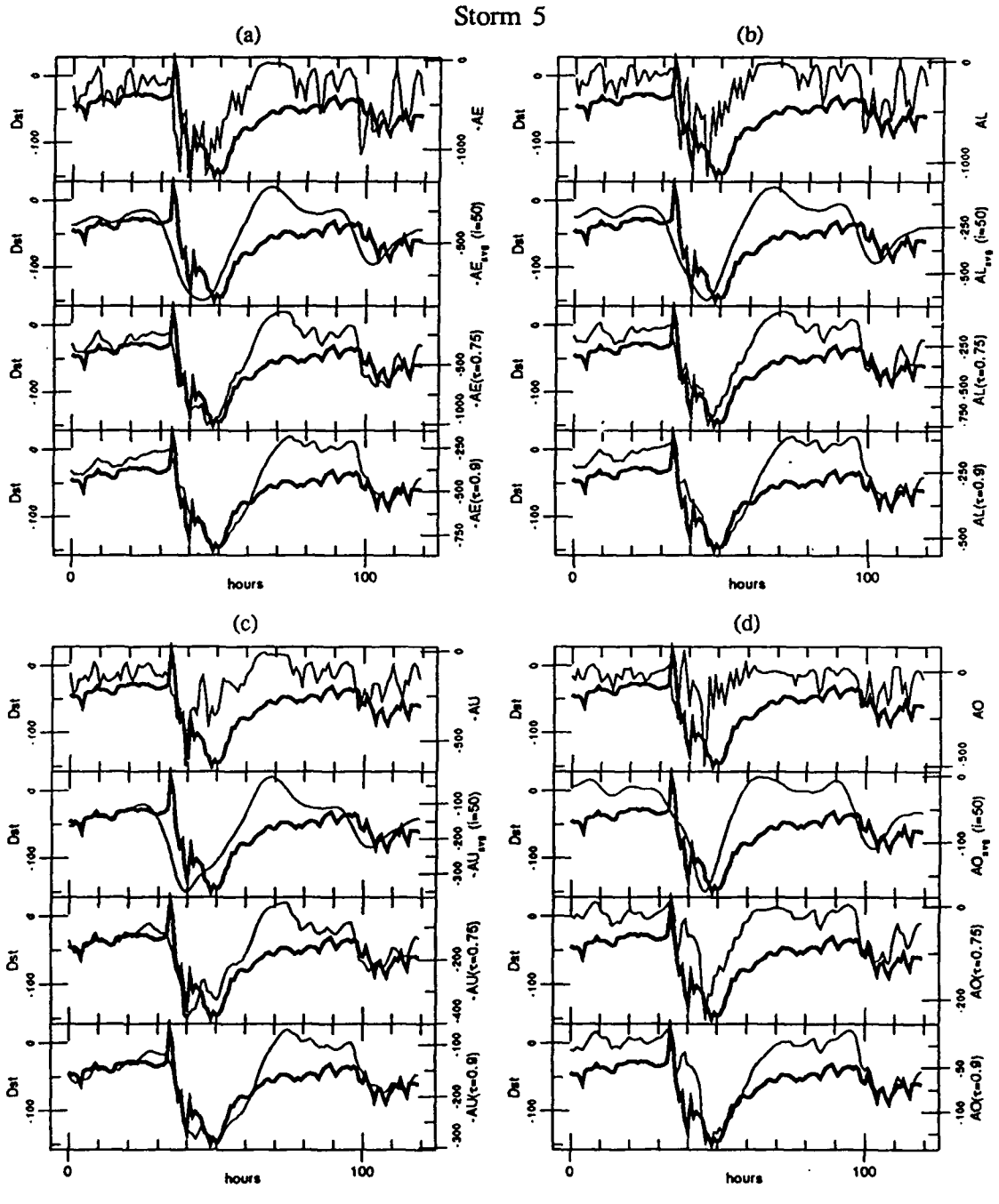

Fig. A.5. Plots for storm 5. *Dst* (bold) is plotted versus *AE*, AE_{avg}, $AE(\tau=0.75)$, and $AE(\tau=0.9)$ (a). The same is done for *AL* (b), *AU* (c), and *AO* (d).

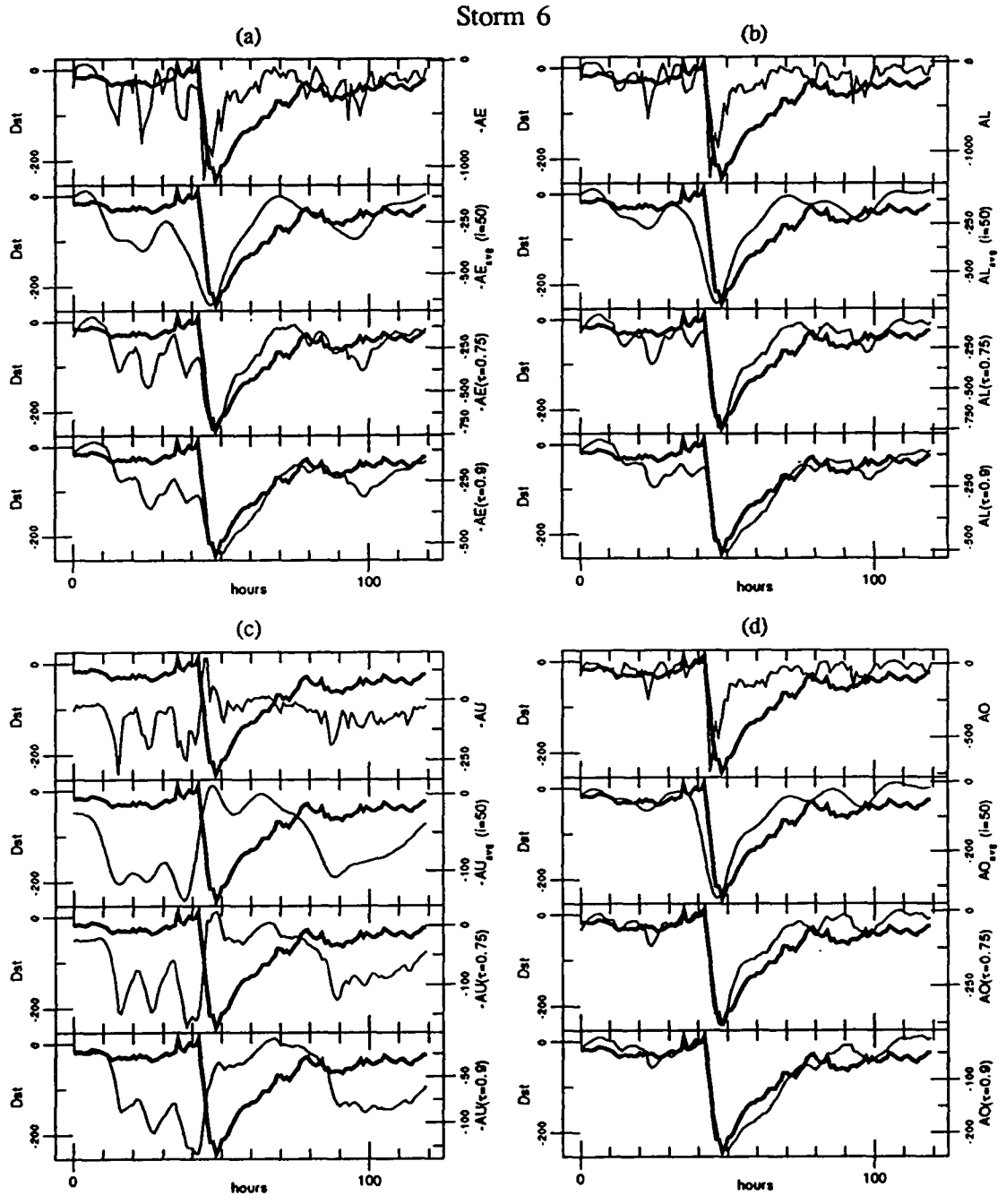

Fig. A.6. Plots for storm 6. *Dst* (bold) is plotted versus AE, AE_{avg}, $AE(\tau=0.75)$, and $AE(\tau=0.9)$ (a). The same is done for AL (b), AU (c), and AO (d).

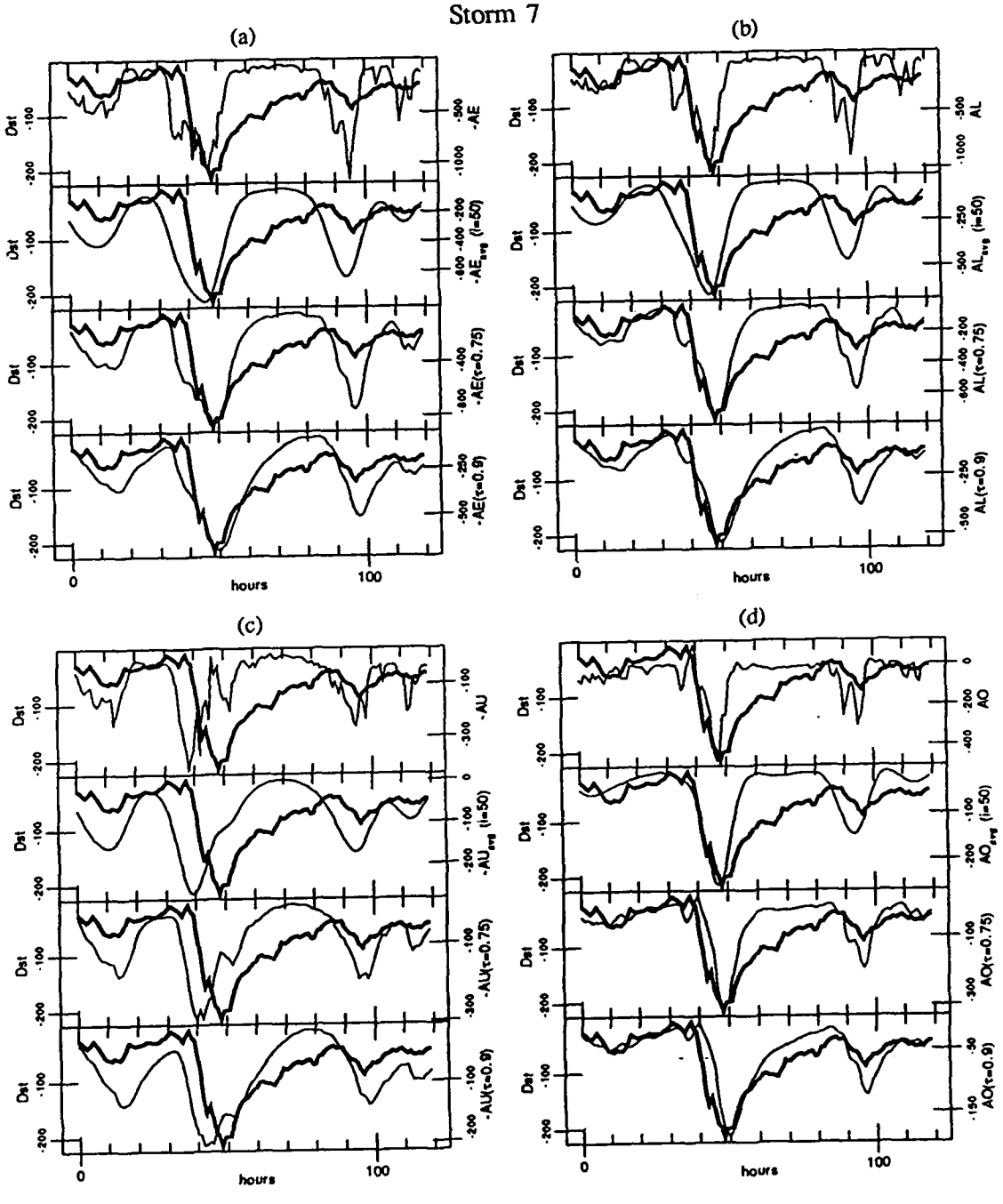

Fig. A.7. Plots for storm 7. *Dst* (bold) is plotted versus AE, AE_{avg}, $AE(\tau=0.75)$, and $AE(\tau=0.9)$ (a). The same is done for AL (b), AU (c), and AO (d).

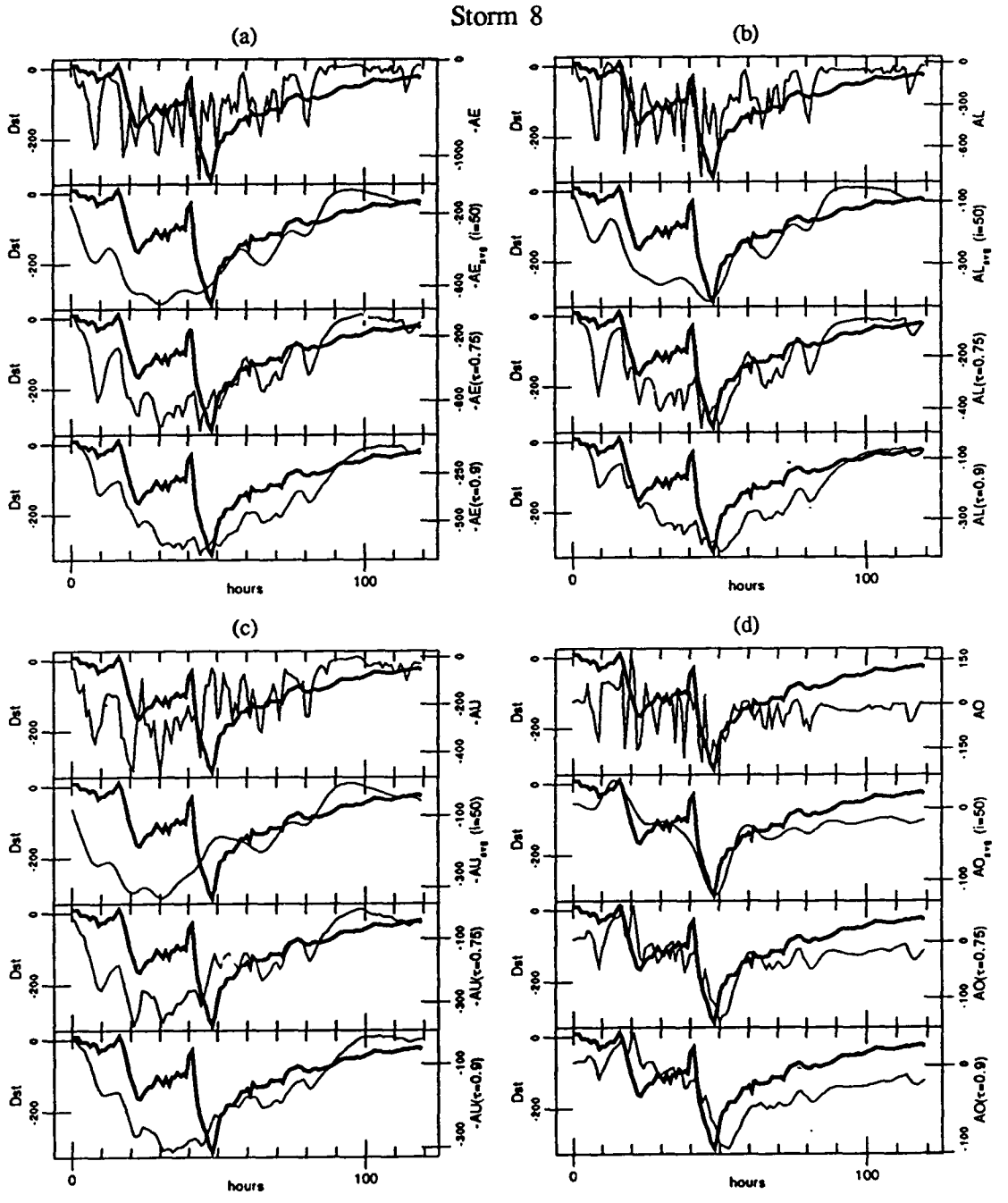

Fig. A.8. Plots for storm 8. *Dst* (bold) is plotted versus AE, AE_{avg}, $AE(\tau=0.75)$, and $AE(\tau=0.9)$ (a). The same is done for AL (b), AU (c), and AO (d).

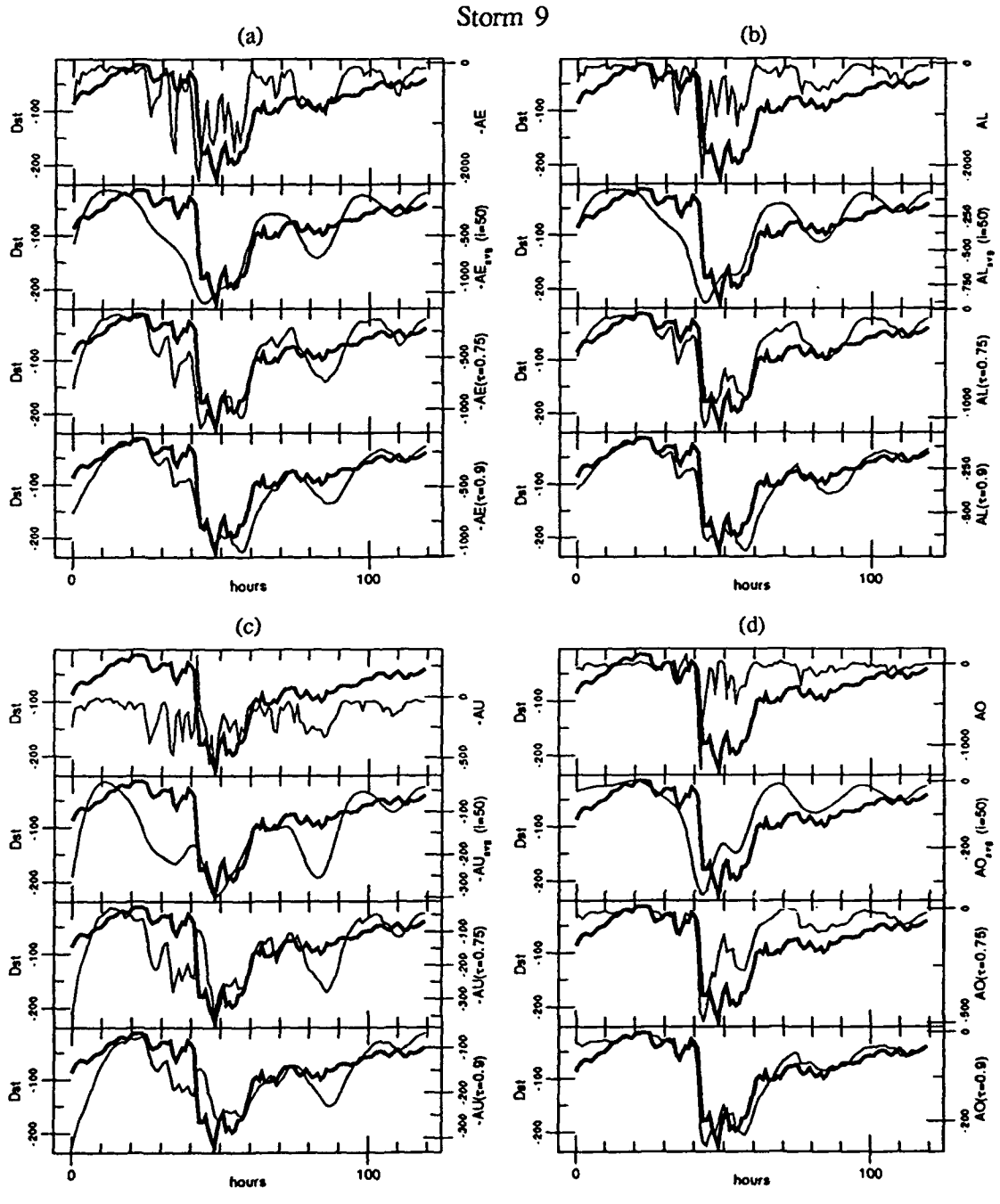

Fig. A.9. Plots for storm 9. *Dst* (bold) is plotted versus *AE*, AE_{avg}, $AE(\tau=0.75)$, and $AE(\tau=0.9)$ (a). The same is done for *AL* (b), *AU* (c), and *AO* (d).

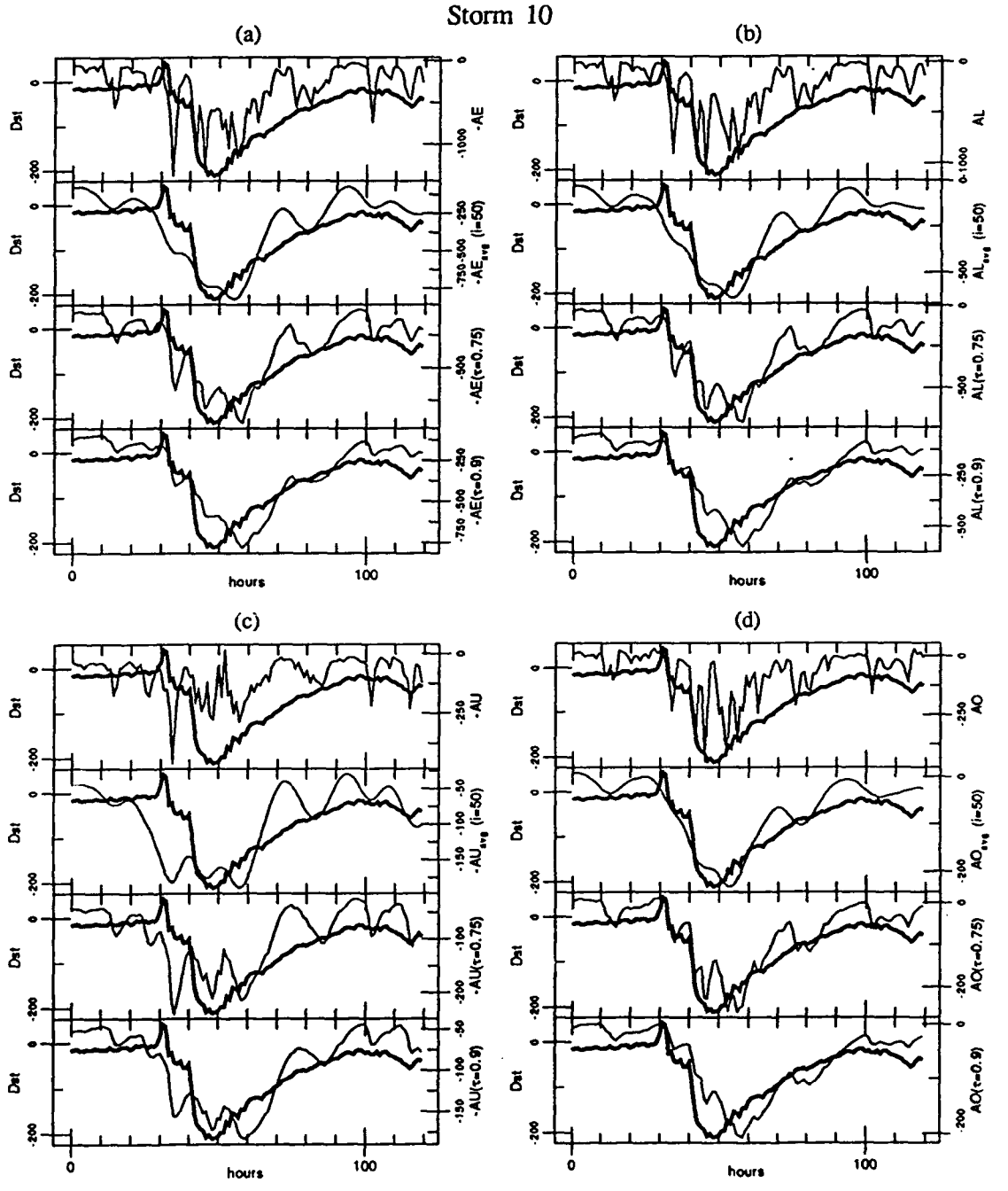

Fig. A.10. Plots for storm 10. *Dst* (bold) is plotted versus AE, AE_{avg}, $AE(\tau=0.75)$, and $AE(\tau=0.9)$ (a). The same is done for AL (b), AU (c), and AO (d).

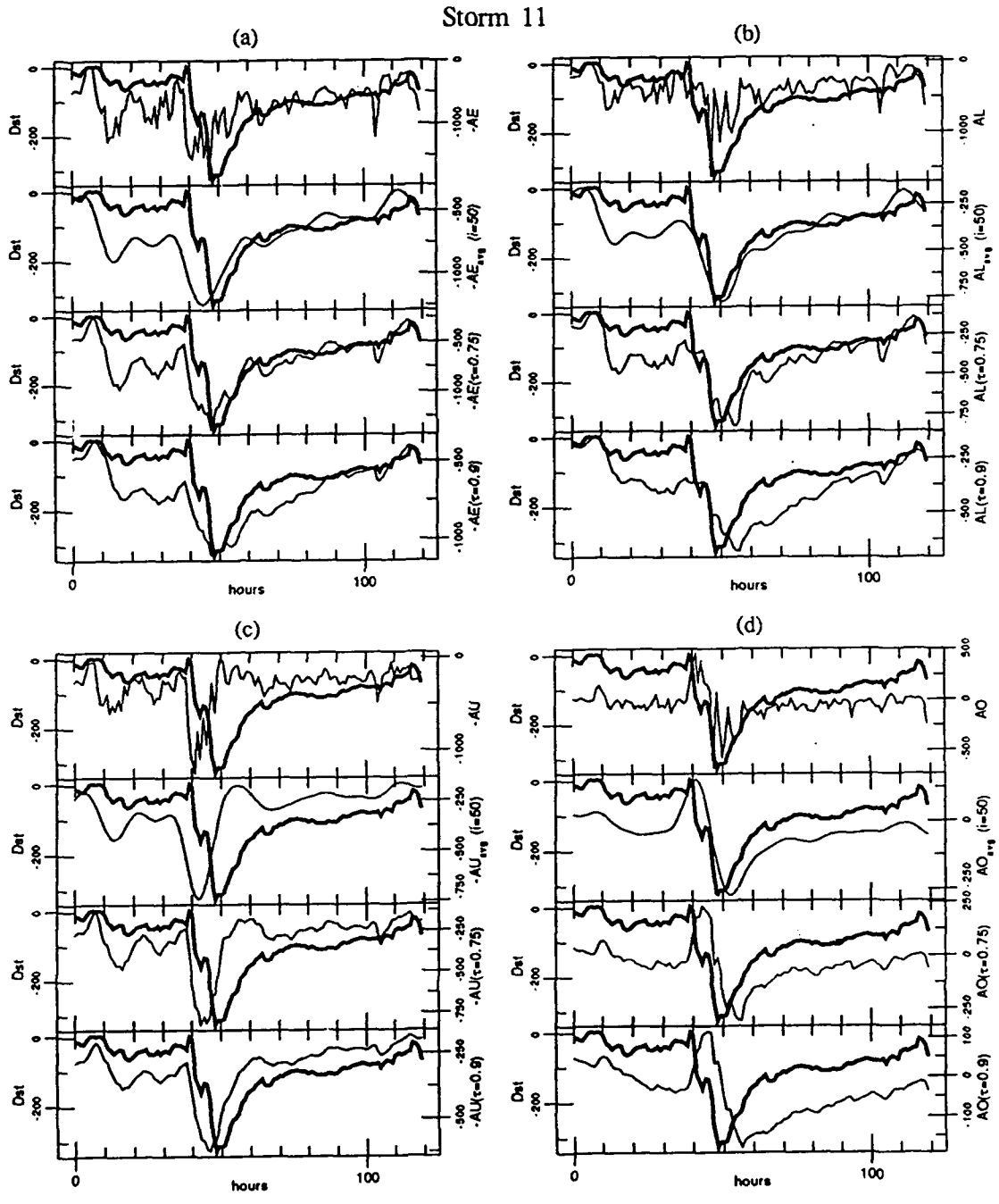

Fig. A.11. Plots for storm 11. *Dst* (bold) is plotted versus AE, AE_{avg}, $AE(\tau=0.75)$, and $AE(\tau=0.9)$ (a). The same is done for AL (b), AU (c), and AO (d).

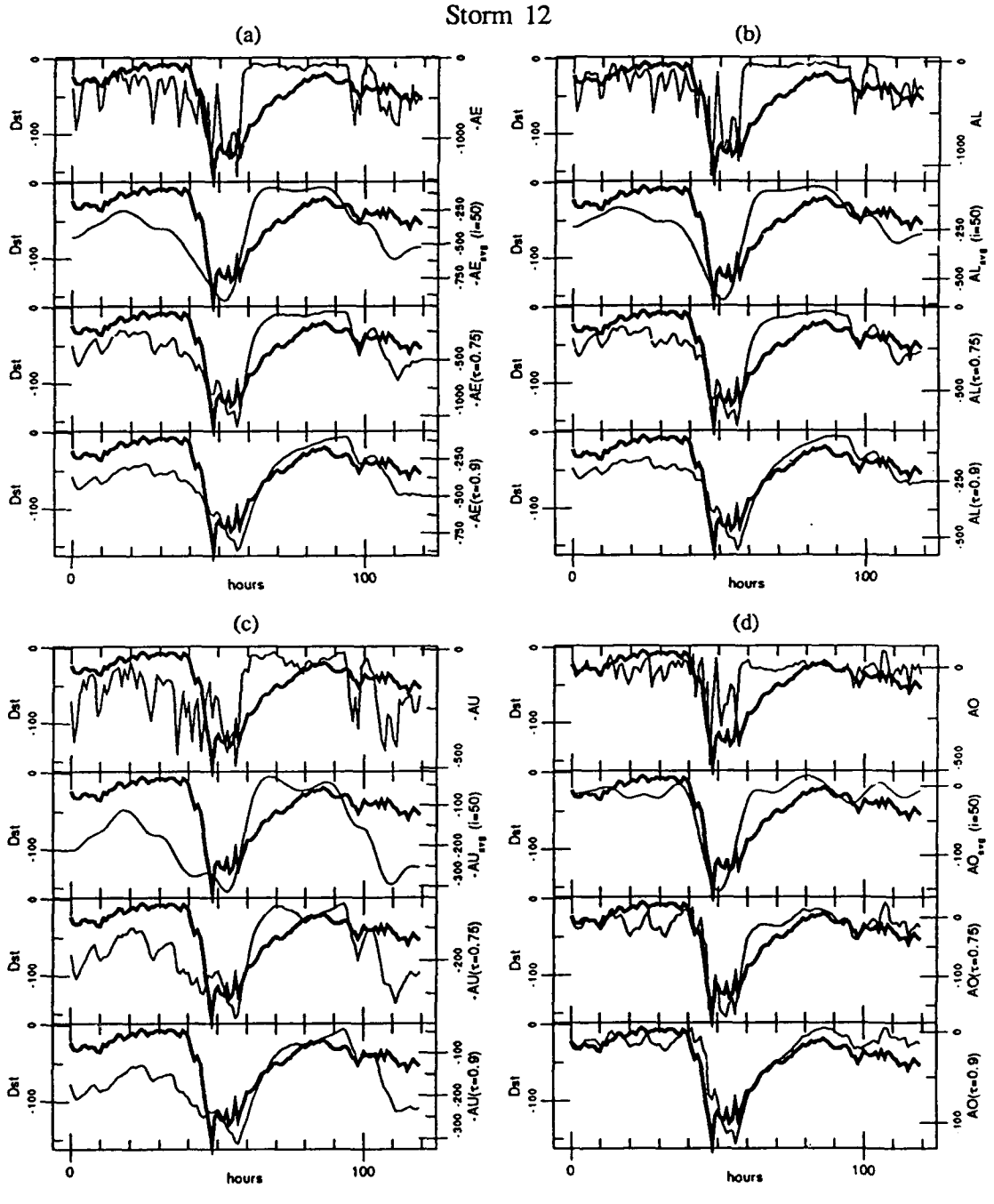

Fig. A.12. Plots for storm 12. *Dst* (bold) is plotted versus AE, AE_{avg}, $AE(\tau=0.75)$, and $AE(\tau=0.9)$ (a). The same is done for AL (b), AU (c), and AO (d).

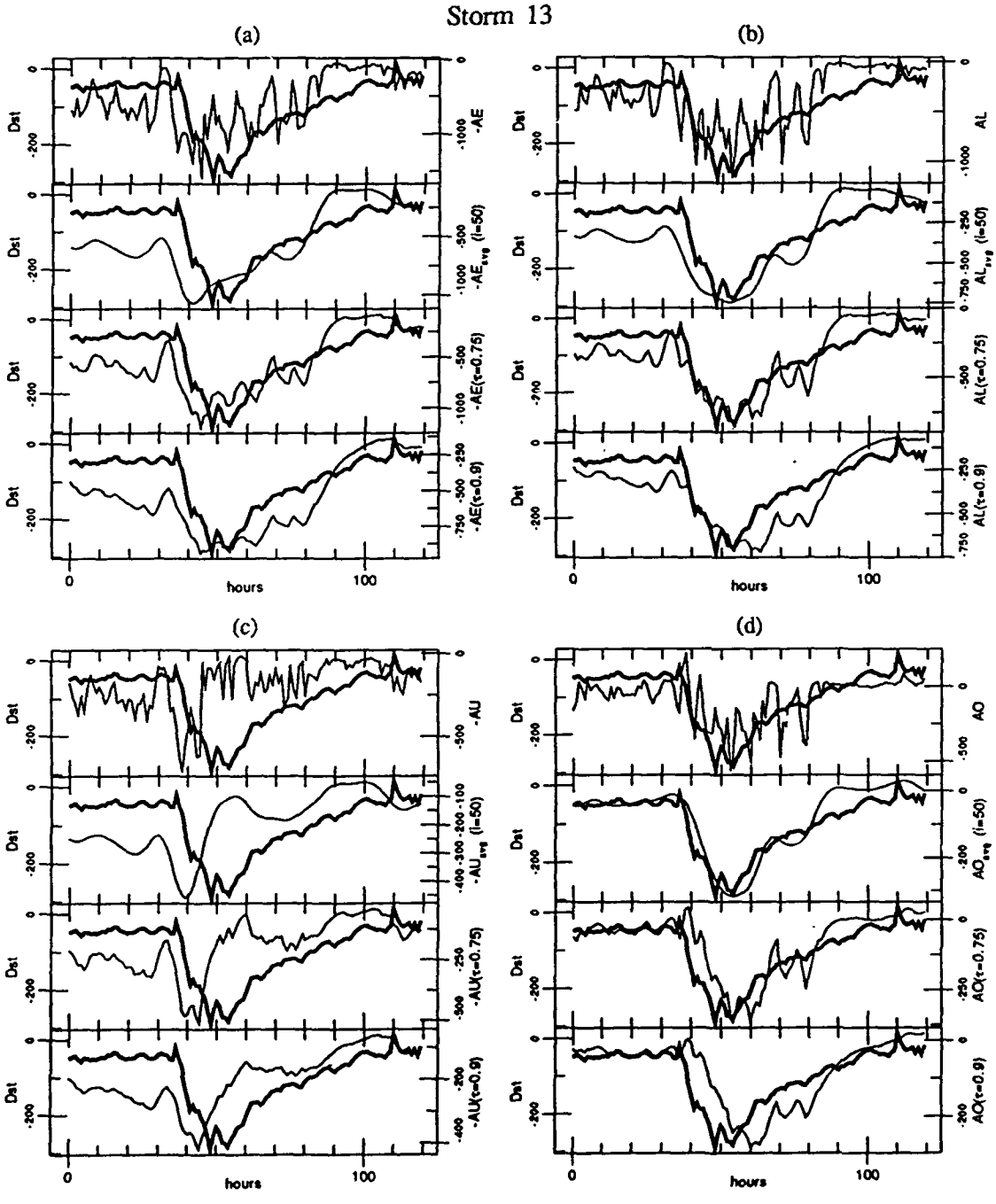

Fig. A.13. Plots for storm 13. *Dst* (bold) is plotted versus AE, AE_{avg}, $AE(\tau=0.75)$, and $AE(\tau=0.9)$ (a). The same is done for AL (b), AU (c), and AO (d).

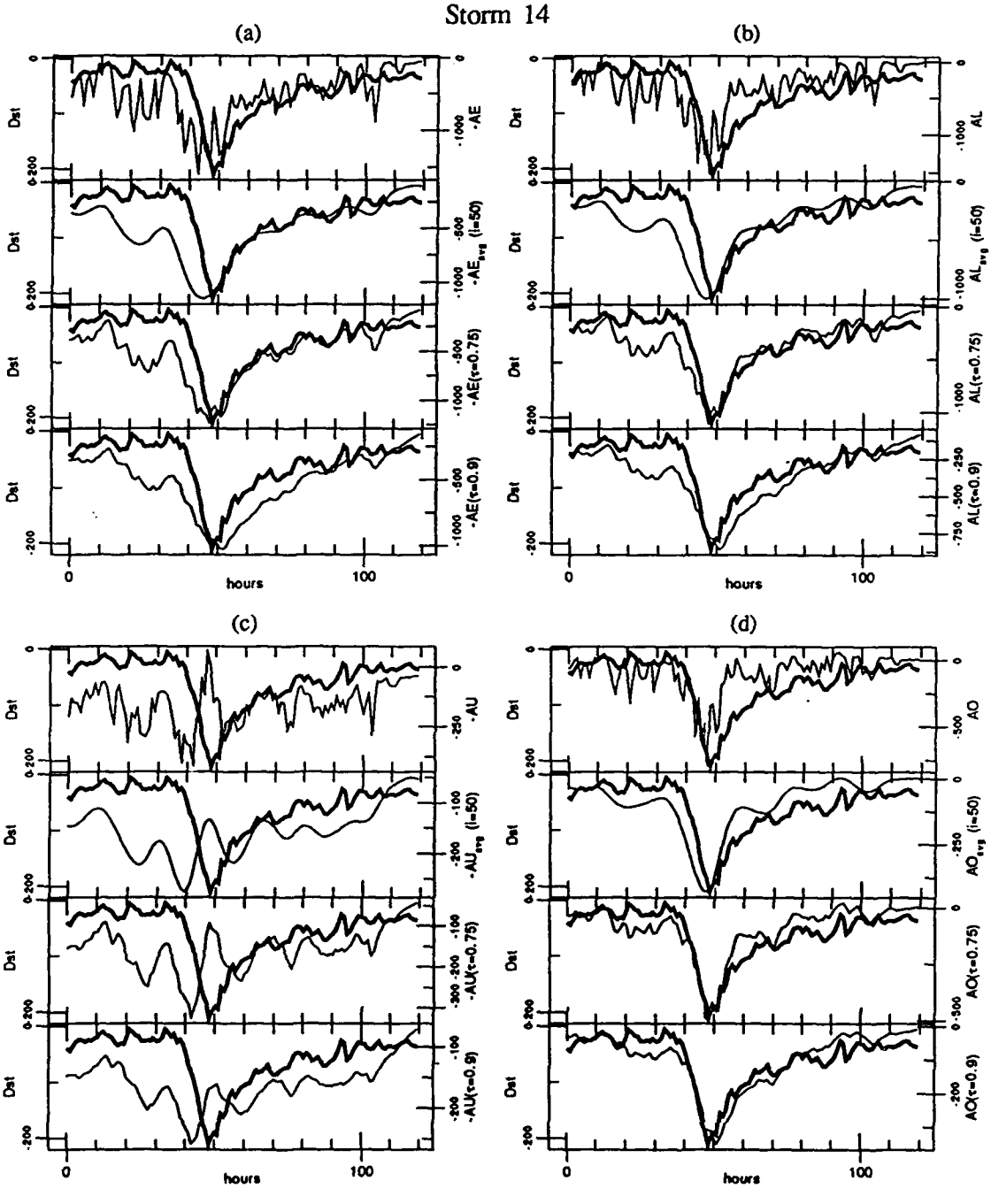

Fig. A.14. Plots for storm 14. *Dst* (bold) is plotted versus AE, AE_{avg}, $AE(\tau=0.75)$, and $AE(\tau=0.9)$ (a). The same is done for AL (b), AU (c), and AO (d).

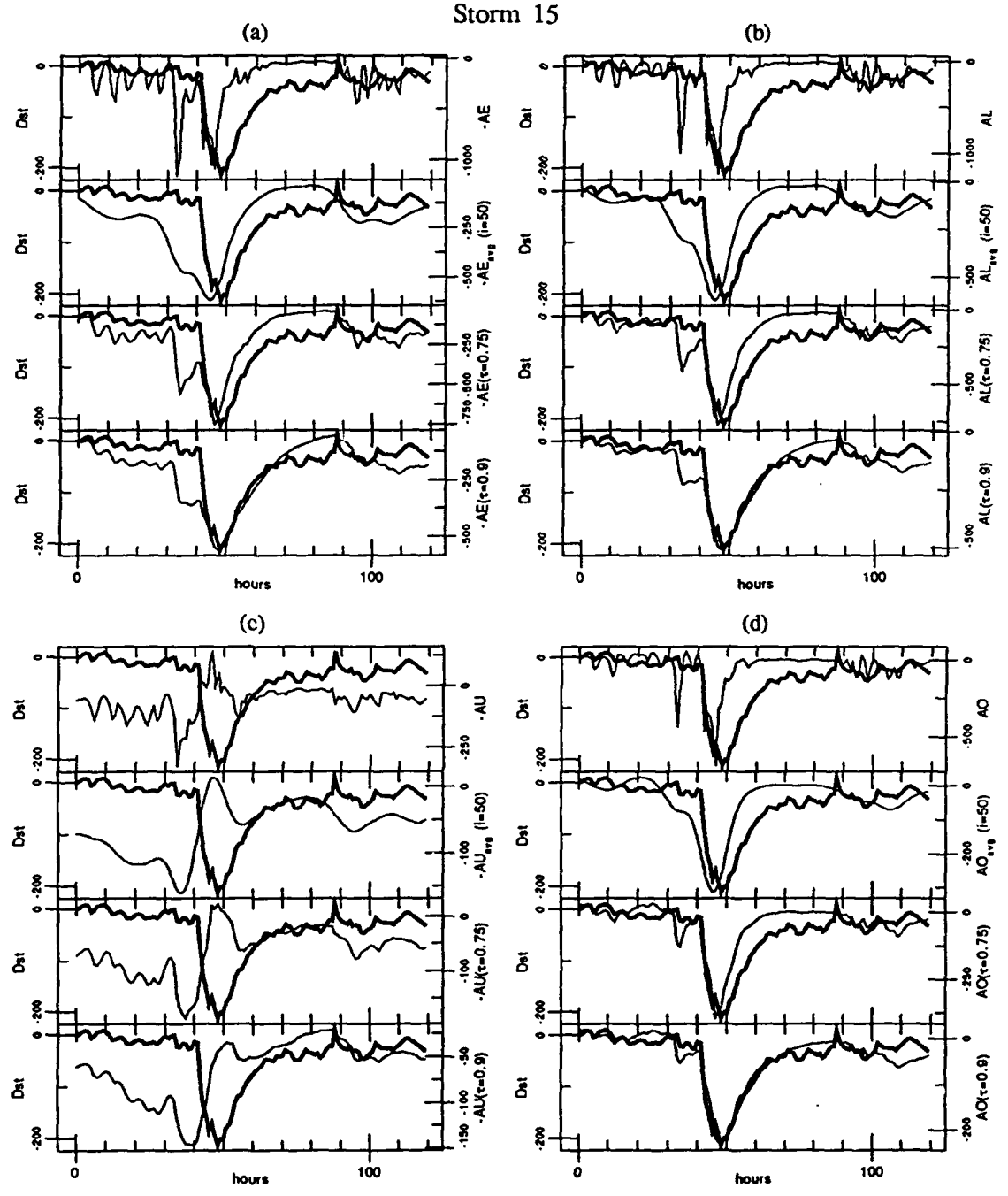

Fig. A.15. Plots for storm 15. *Dst* (bold) is plotted versus AE, AE_{avg}, $AE(\tau=0.75)$, and $AE(\tau=0.9)$ (a). The same is done for AL (b), AU (c), and AO (d).

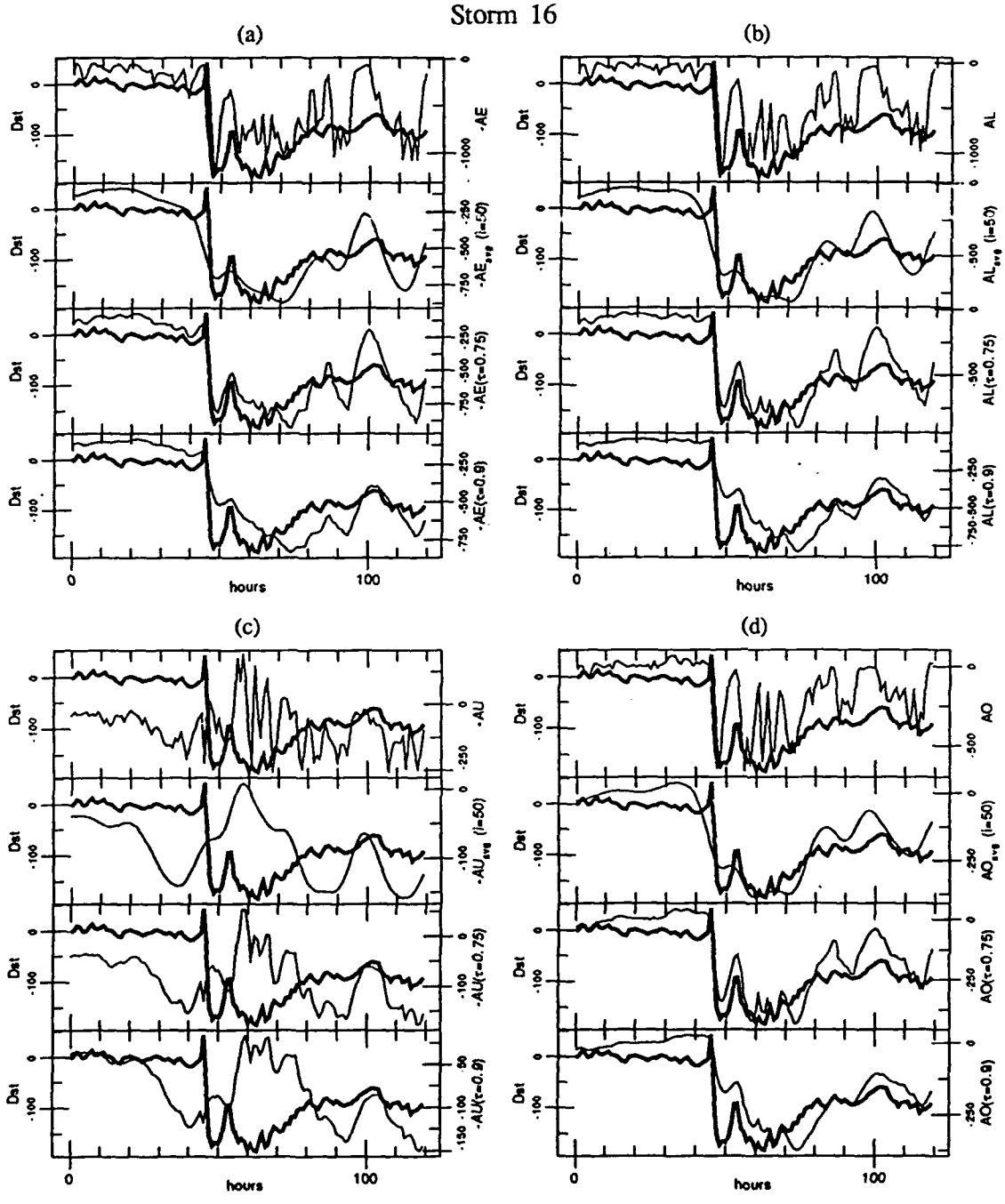

Fig. A.16. Plots for storm 16. *Dst* (bold) is plotted versus AE, AE_{avg}, $AE(\tau=0.75)$, and $AE(\tau=0.9)$ (a). The same is done for AL (b), AU (c), and AO (d).

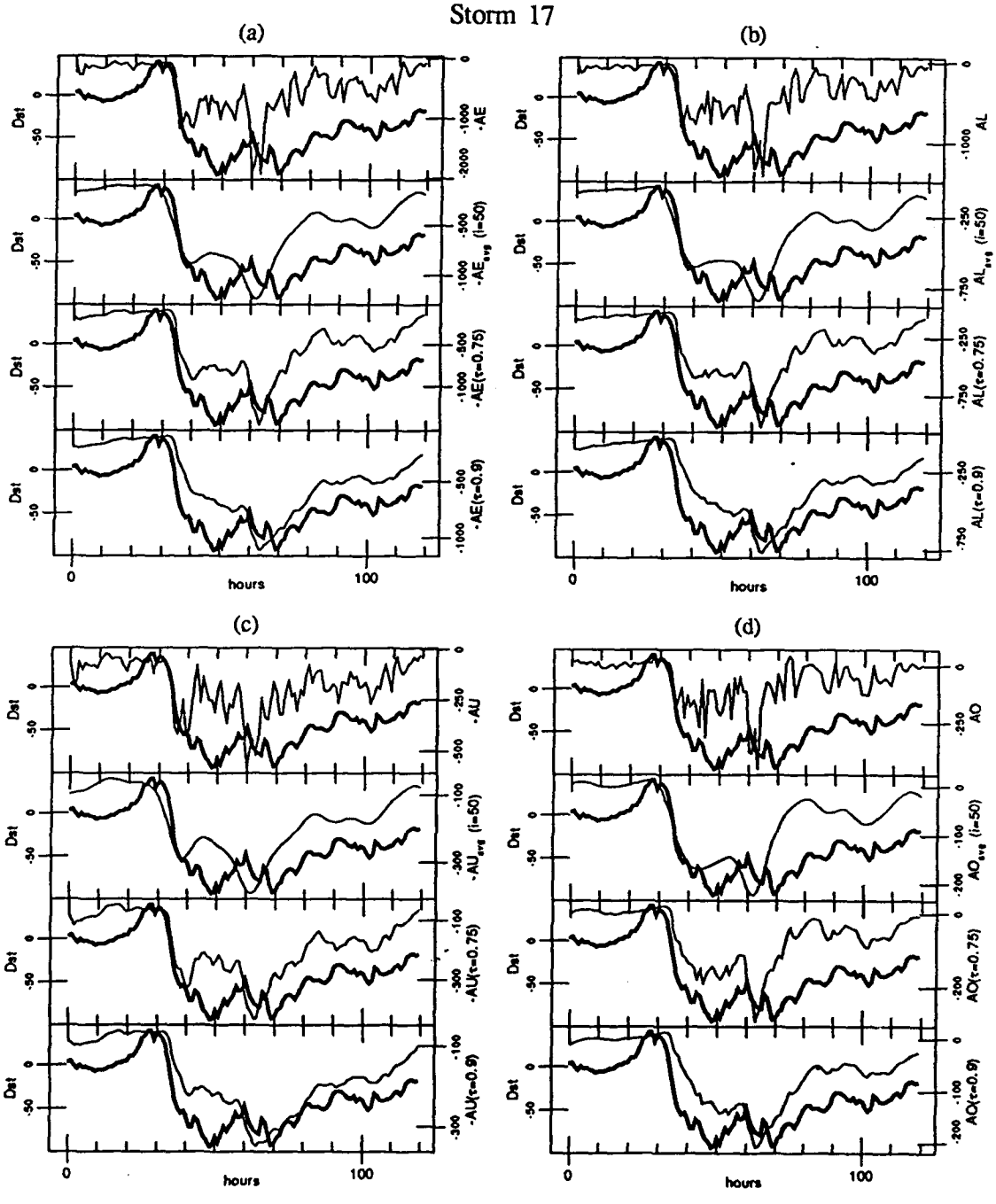

Fig. A.17. Plots for storm 17. *Dst* (bold) is plotted versus *AE*, AE_{avg}, $AE(\tau=0.75)$, and $AE(\tau=0.9)$ (a). The same is done for *AL* (b), *AU* (c), and *AO* (d).

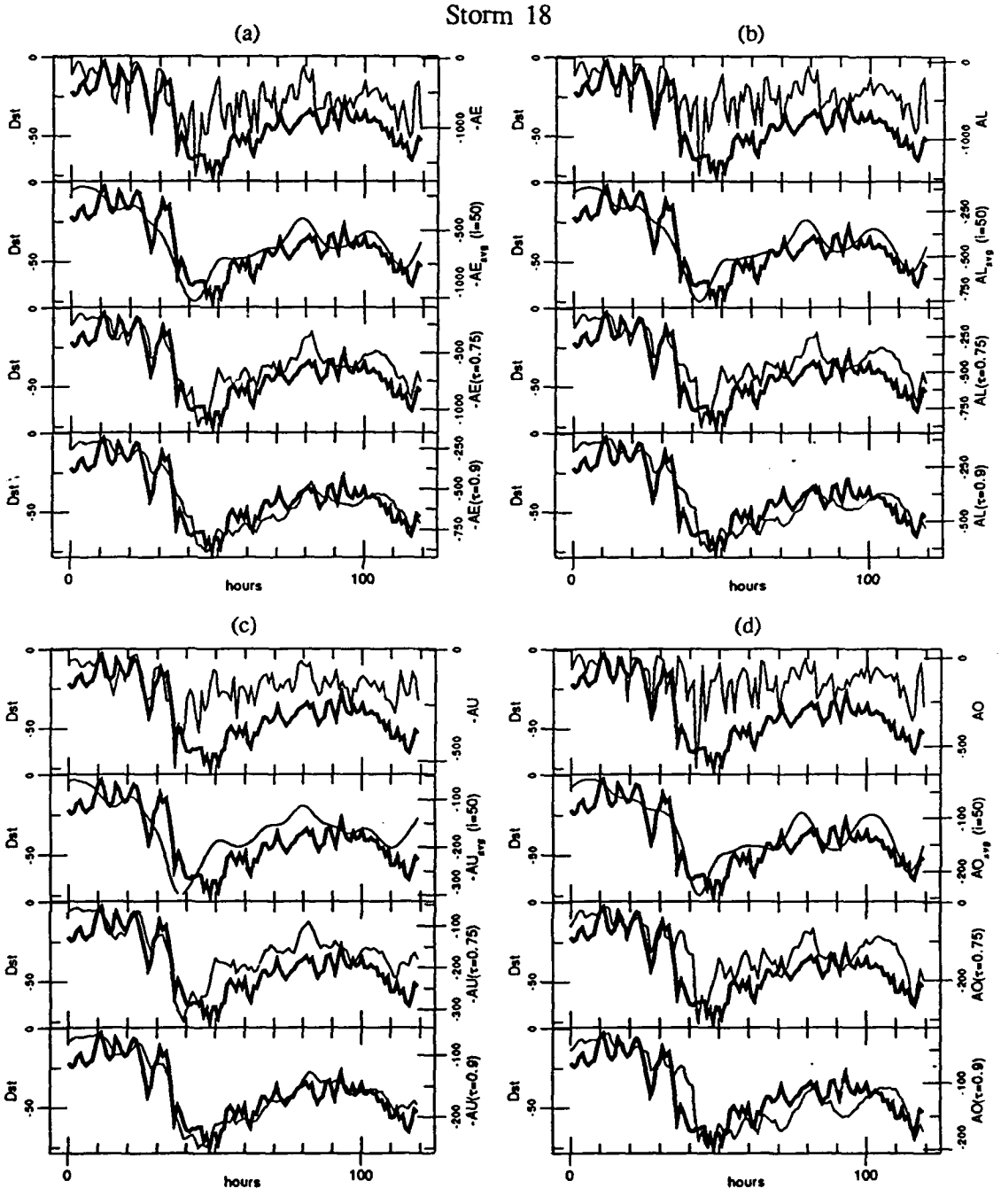

Fig. A.18. Plots for storm 18. *Dst* (bold) is plotted versus AE, AE_{avg}, $AE(\tau=0.75)$, and $AE(\tau=0.9)$ (a). The same is done for AL (b), AU (c), and AO (d).

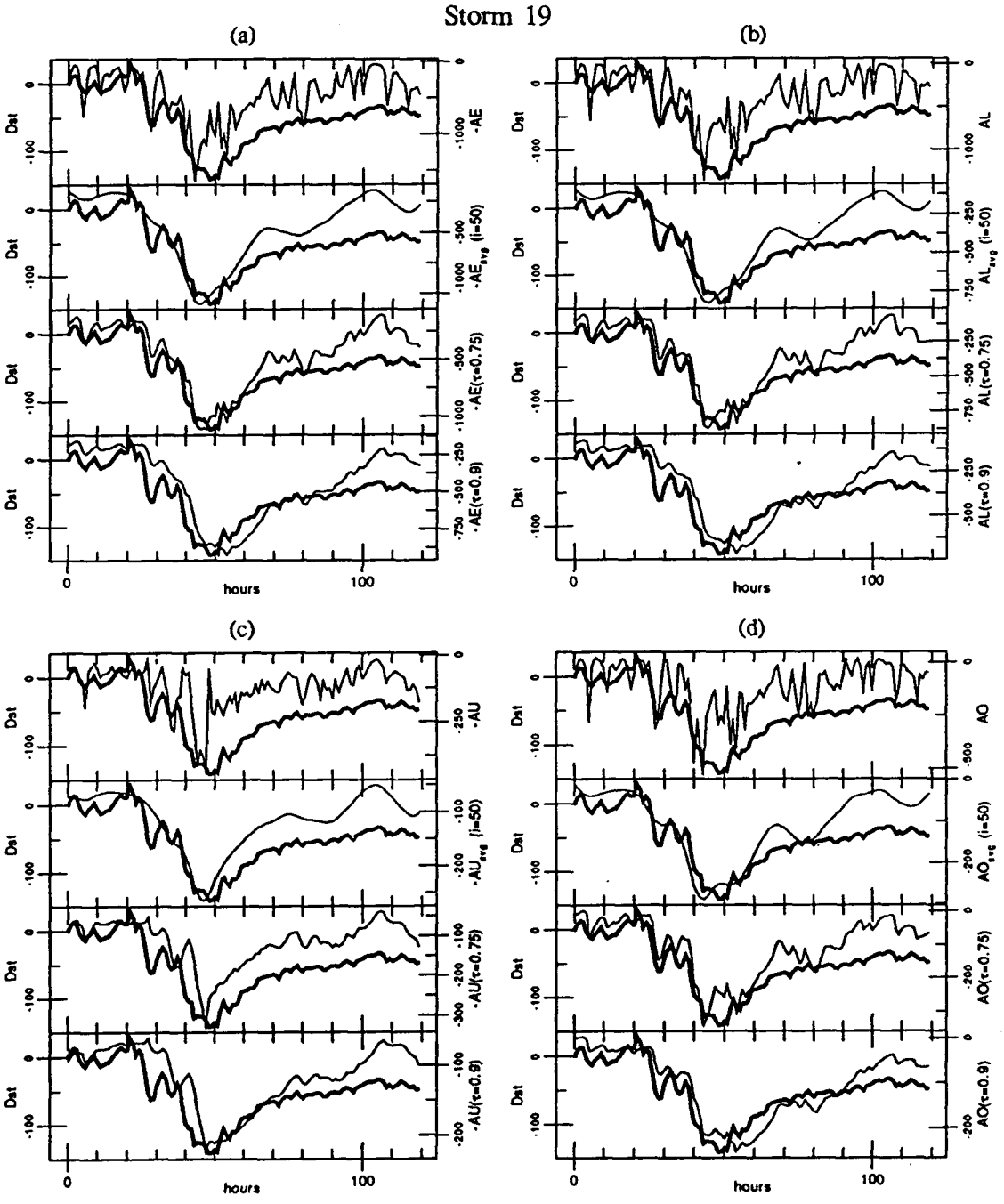

Fig. A.19. Plots for storm 19. *Dst* (bold) is plotted versus AE, AE_{avg}, $AE(\tau=0.75)$, and $AE(\tau=0.9)$ (a). The same is done for AL (b), AU (c), and AO (d).

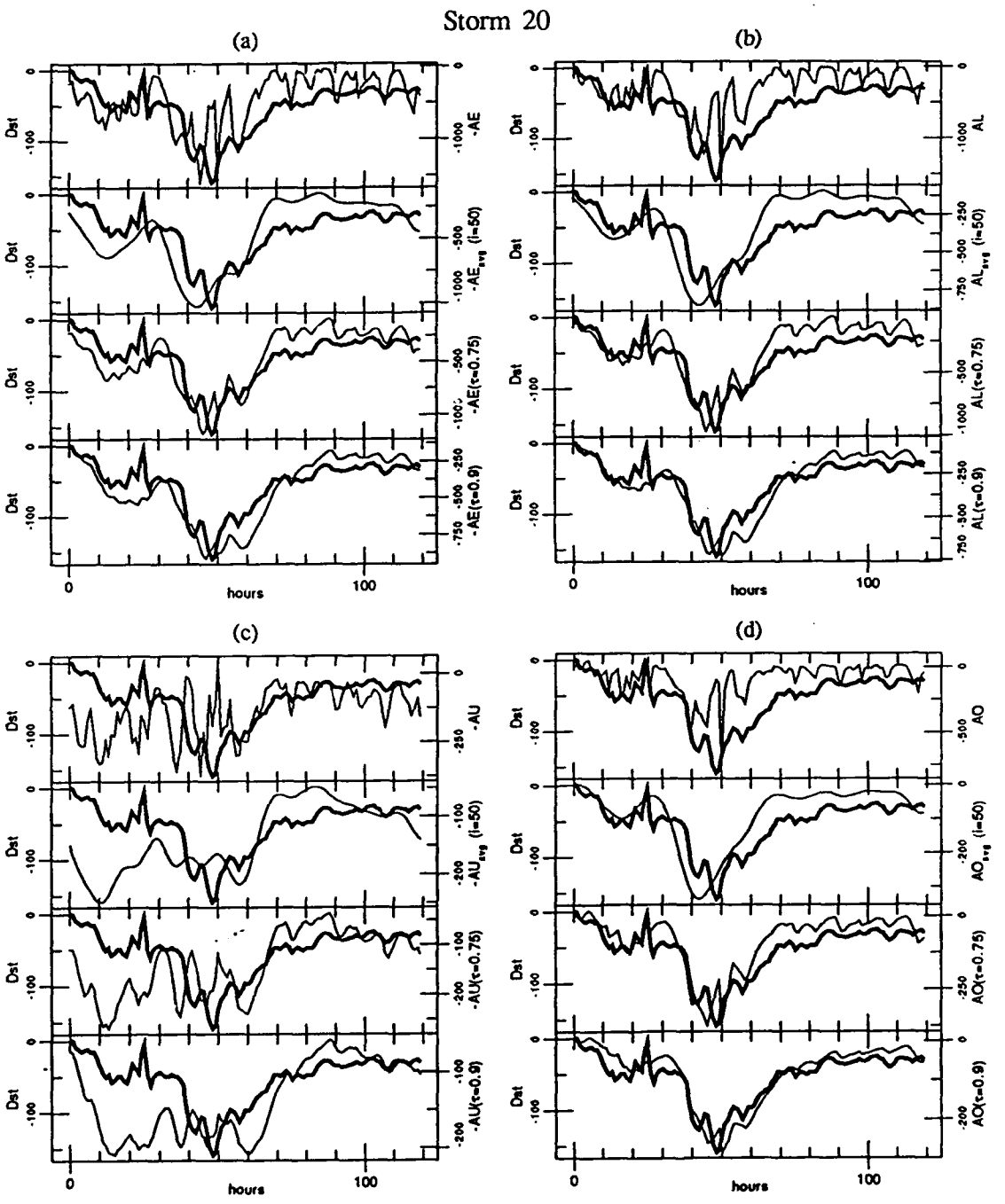

Fig. A.20. Plots for storm 20. *Dst* (bold) is plotted versus AE, AE_{avg}, $AE(\tau=0.75)$, and $AE(\tau=0.9)$ (a). The same is done for AL (b), AU (c), and AO (d).

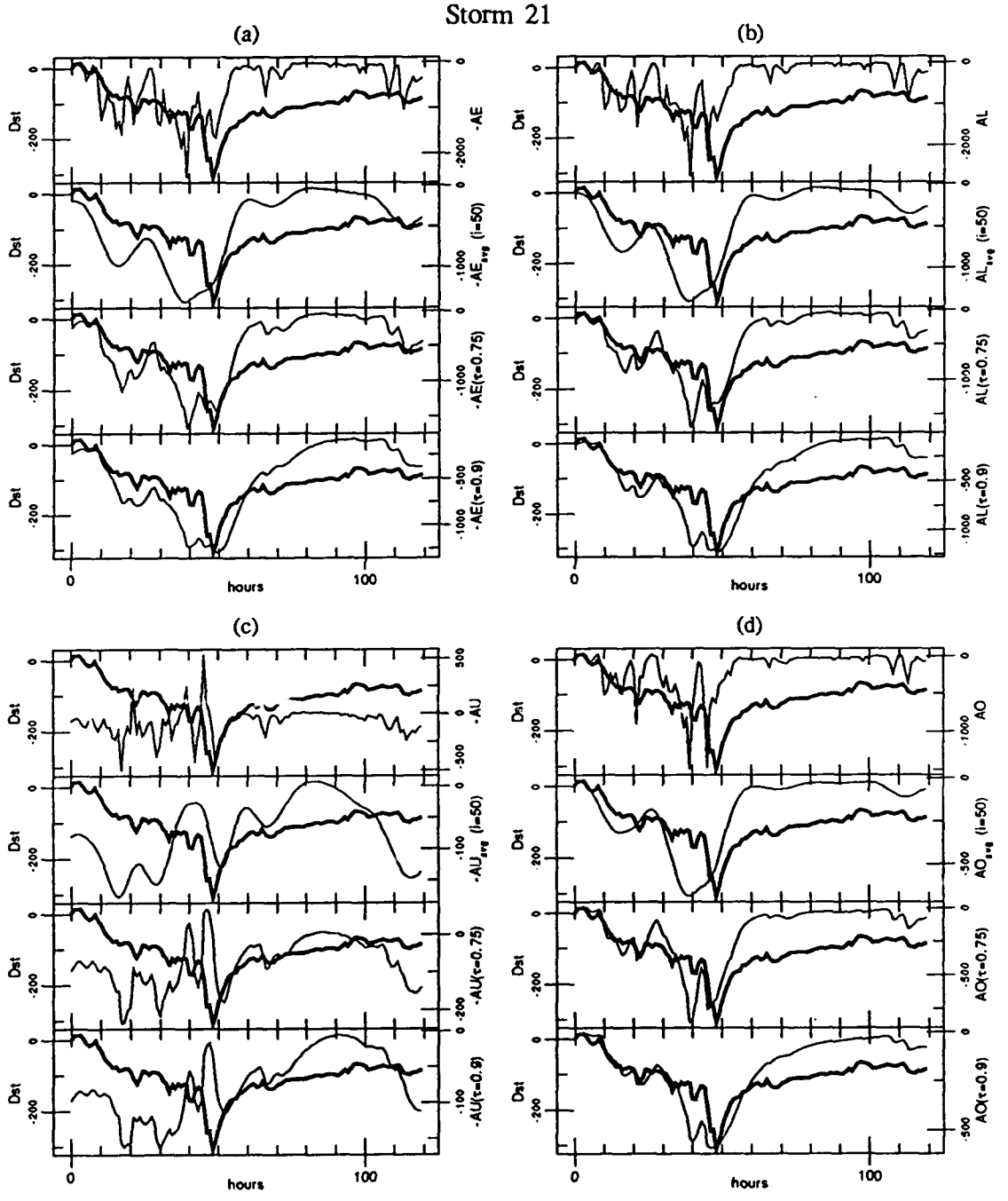

Fig. A.21. Plots for storm 21. *Dst* (bold) is plotted versus AE, AE_{avg}, $AE(\tau=0.75)$, and $AE(\tau=0.9)$ (a). The same is done for AL (b), AU (c), and AO (d).

APPENDIX B. FOURIER ANALYSIS OF 1 MINUTE AE DATA

FOURIER ANALYSIS OF 1 MINUTE AE DATA

A Fourier Transform analysis was done on one sample storm to determine the properties of the 1-minute *AE* index as it relates to the 1-hour index and the various manipulations performed on it. The storm selected was storm 11, July 13-16, 1982 because it is fairly representative of a normal storm.

First, the Fourier coefficients were obtained from the following relation [Chatfield, 1975]:

$$\begin{aligned} a_0 &= \bar{x} \\ a_{N/2} &= \sum_{t=1}^{N} (-1)^t \frac{x_t}{N} \\ a_p &= \frac{2}{N} \sum_{t=1}^{N} x_t \cos\left(\frac{2\pi pt}{N}\right) \\ b_p &= \frac{2}{N} \sum_{t=1}^{N} x_t \sin\left(\frac{2\pi pt}{N}\right) \end{aligned} \qquad \text{(A1)}$$

where N is the number of datapoints and p ranges from 1 to N/2−1. The 1-minute index was then reconstructed using:

$$x_t = a_0 + \sum_{p=1}^{\frac{N}{2}-1} \left[a_p \cos\left(\frac{2\pi pt}{N}\right) + b_p \sin\left(\frac{2\pi pt}{N}\right)\right] + a_{N/2} \cos(\pi t) \qquad \text{(A2)}$$

with the higher frequencies removed. Figure A.22 shows that when frequencies greater than 69 MHz are removed (corresponding to periods of 4 hours and lower),

the result is very similar to the 1-hour AE index. When frequencies higher than 28 MHz are removed, it is very similar to AE_{avg} achieved by space-centered averaging of the 1-hour AE index with 10 iterations. This demonstrates that the 1-hour AE index contains only lower frequency components of the electrojet variations and that AE_{avg} contains only increasingly lower components as the number of iterations is increased.

Next, time-weighted accumulations were applied to the 1-minute AE index. In Figure A.23 it can be seen that a τ of 0.9883 (corresponding to a decay time of ~10 hours for 1-minute data) applied to the 1-minute AE is virtually identical to a τ of 0.9 (corresponding to a decay time of ~10 hours for 1-hour data) used on the 1-hour AE. Similar results are found when τ=0.9883 is used for 1-minute AE with higher frequencies removed. Therefore, when time-weighted accumulations are used, very little is lost when using the 1-hour AE index as opposed to the 1-minute index.

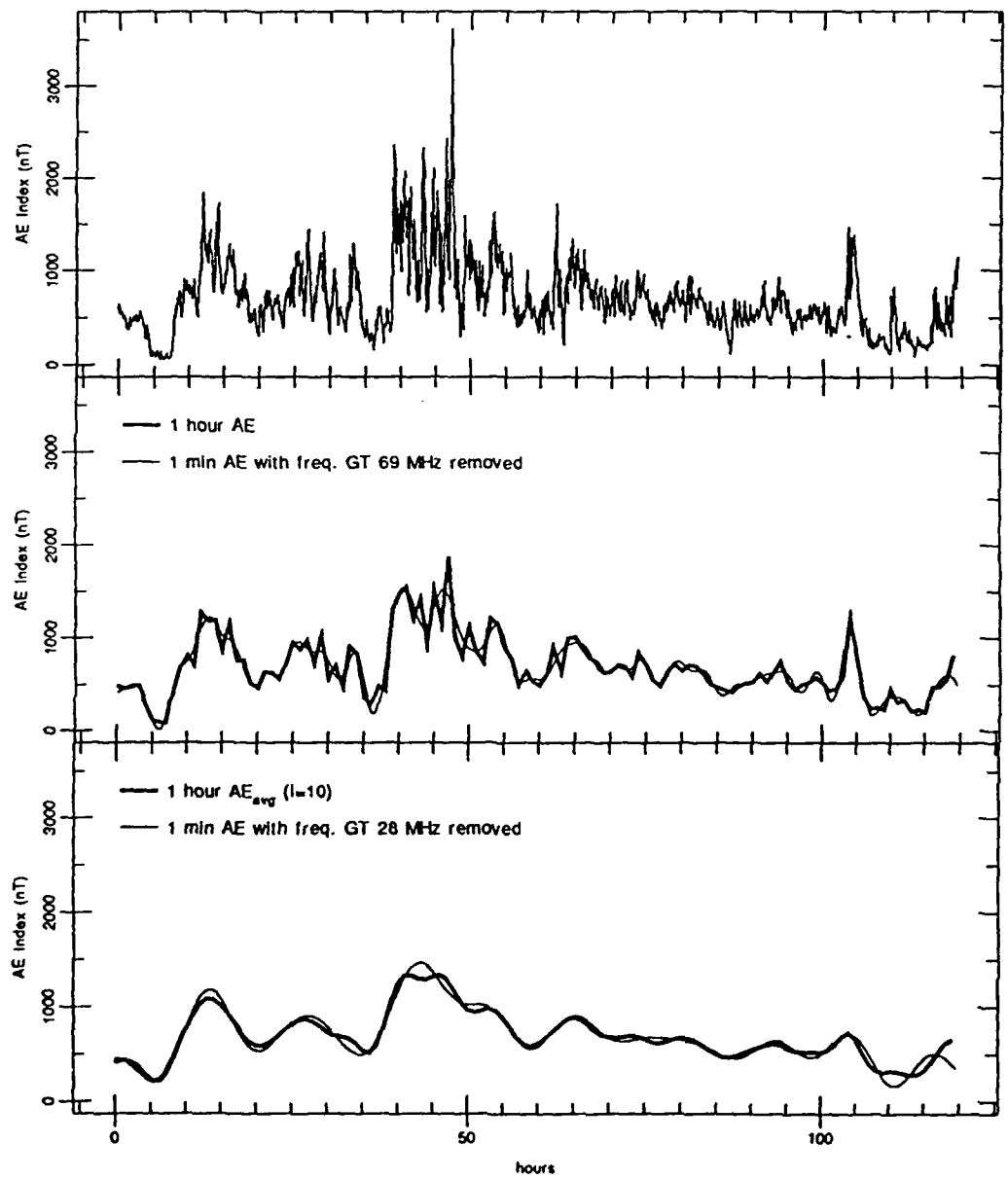

Fig. A.22. One minute *AE* (top) and 1 minute *AE* with higher frequencies removed compared to 1 hour *AE* (middle) and AE_{avg} (bottom).

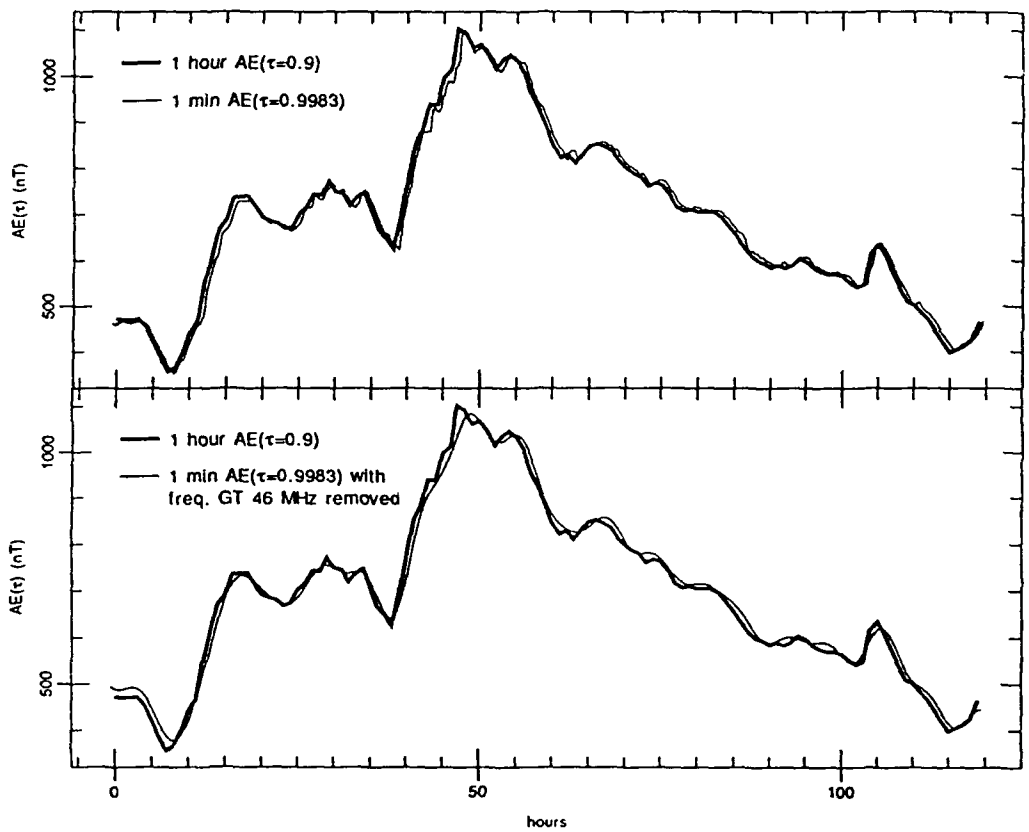

Fig. A.23. Time-weighted accumulations of 1 minute AE (τ=0.9883), both unaltered and with higher frequencies removed, compared to time-weighted accumulations of 1 hour AE (τ=0.9).

APPENDIX C. DST MODELING FROM SOLAR WIND PARAMETERS

DST MODELING FROM SOLAR WIND PARAMETERS

As stated by *Feldstein* [1992] in his review of ring current modeling, the method outlined by *Pisarsky et al.* [1989] is one of the best for deriving *Dst* from IMF data. in order to give examples of the current state of *Dst* modeling, this method will be applied to those storms of the 21 that have as complete a set of IMF data as possible.

Pisarsky et al. used this relation:

$$DR_{i+1} = \frac{DR_i(2-\frac{1}{\tau}) + 2F_i}{2 + \frac{1}{\tau}} \qquad \text{(A3)}$$

where DR is the measure of the ring current (*Dst* minus magnetospheric compression) and F is the ring current injection function modeled by:

$$F = (8.2\times10^{-3})v(B_z-0.67\sigma) - 14.1\times10^{-3}(v-300) + 9.4, \quad \text{for } v(B_z-0.67\sigma) < -1146 \text{ (injection)} \qquad \text{(A4)}$$

$$F = (-14.1\times10^{-3}(v-300), \quad \text{for } v(B_z-0.67\sigma) > -1146 \text{ (decay)} \qquad \text{(A5)}$$

where σ is the IMF modulus. The decay parameter is obtained from:

$$\tau_{mp} = 2.4 + 13e^{0.08F} \quad \text{(main phase)}$$
$$\tau_{rp} = 10.0 + 1.84e^{0.007DR} \quad \text{(recovery phase)} \qquad \text{(A6)}$$

using the F or DR value for that hour. Since no definition of the IMF modulus σ could be found, it was set to 0. The results of applying this method to storms 2, 3, 4, 6, and 9 are shown in Figures A.24-A.28.

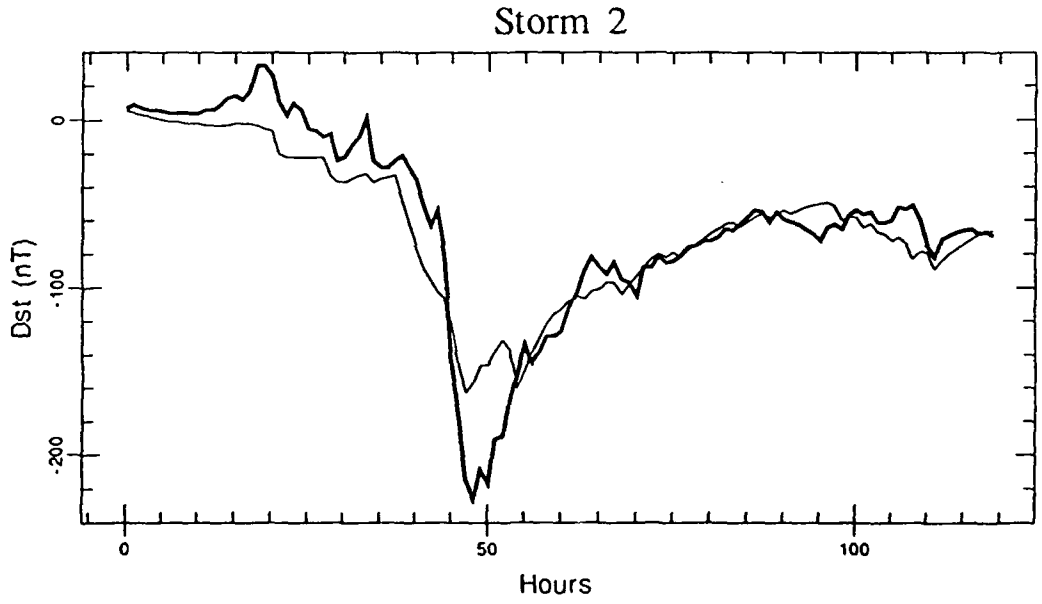

Fig. A.24. *Dst* (bold line) compared to *Dst* derived from the method of Pisarsky et al. for Storm 2.

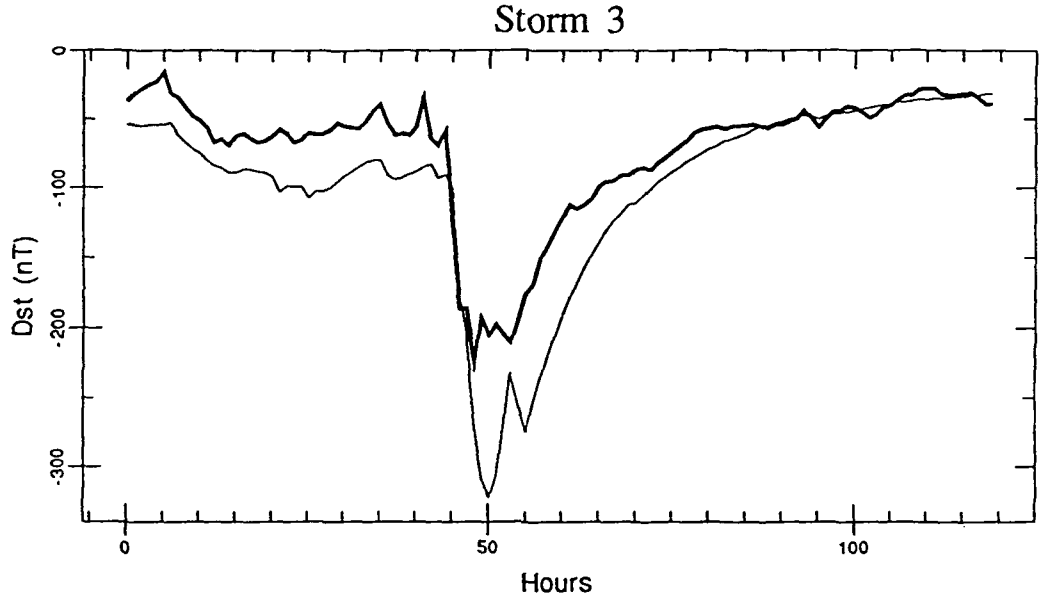

Fig. A.25. *Dst* (bold line) compared to *Dst* derived from the method of Pisarsky et al. for Storm 3.

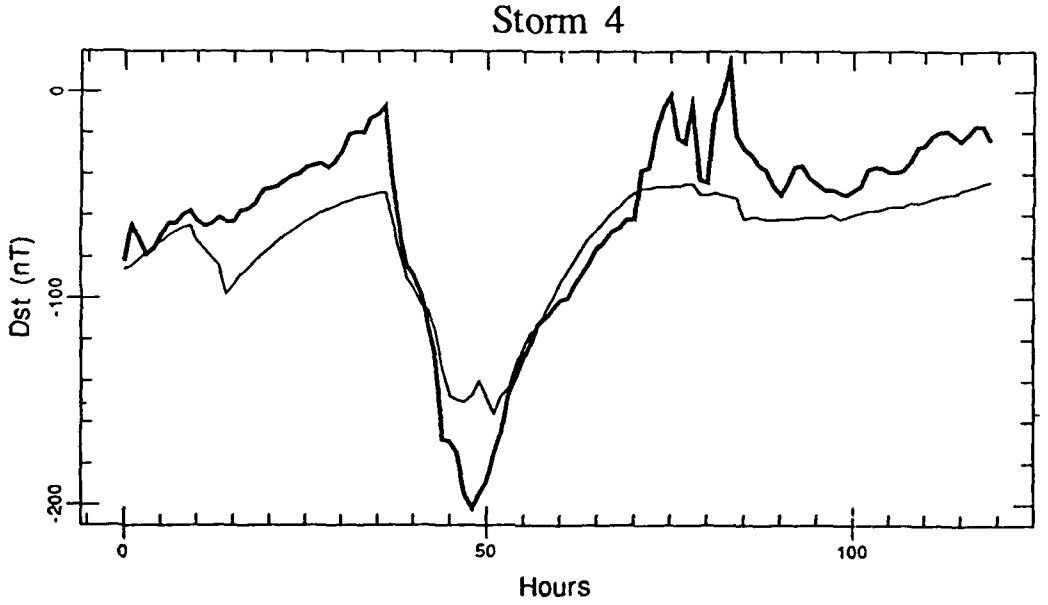

Fig. A.26. *Dst* (bold line) compared to *Dst* derived from the method of Pisarsky et al. for Storm 4.

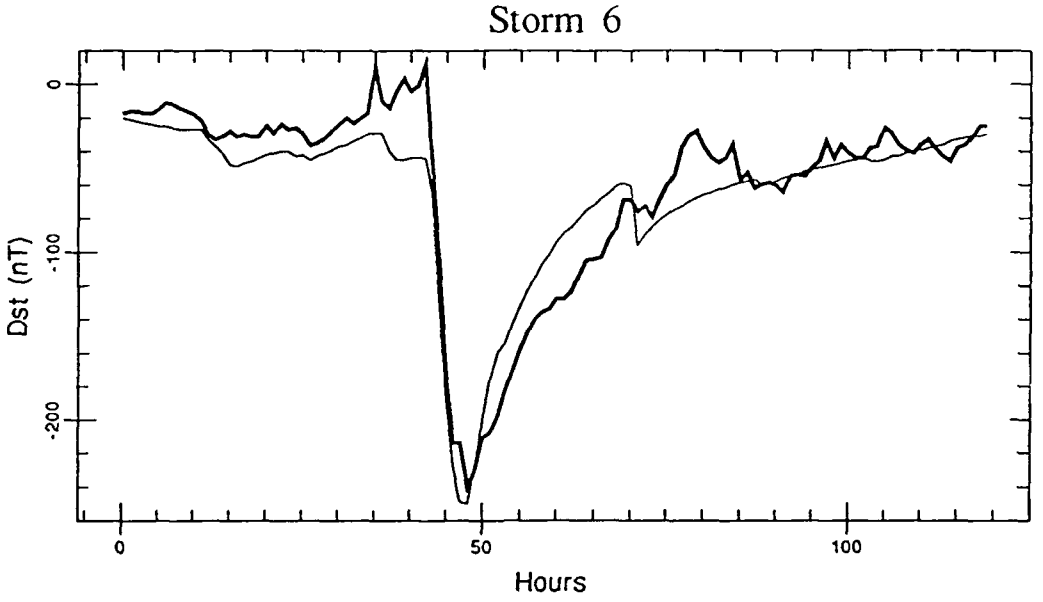

Fig. A.27. *Dst* (bold line) compared to *Dst* derived from the method of Pisarsky et al. for Storm 6.

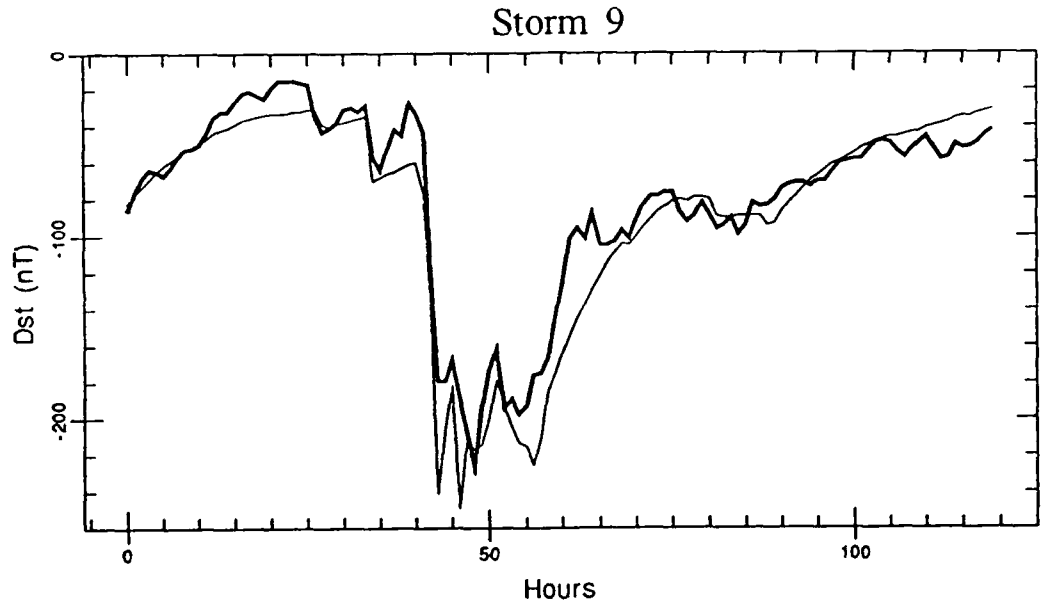

Fig. A.28. *Dst* (bold line) compared to *Dst* derived from the method of Pisarsky et al. for Storm 9.

APPENDIX D. COPYRIGHT CREDIT AND PERMISSION

COPYRIGHT CREDIT

Figure 11 from McPherron, R. L., Magnetospheric substorms, *Reviews of Geophysics and Space Physics*, Vol. 17, p. 657, 1979, copyright by the American Geophysical Union.

Figure 12 from McPherron, R. L., Physical processes producing magnetospheric substorms and magnetic storms, in *Geomagnetism*, Vol. 4, edited by J. A. Jacobs, Chapter 7, pp. 593-739, Academic Press, London, 1991.

Figures 16 and 17 from Akasofu, S. I., Prediction of development of geomagnetic storms using the solar wind-magnetosphere energy coupling function ϵ, *Planetary and Space Science*, Vol. 29, p. 1151, 1981, copyright by the American Geophysical Union.

Figure 18 from Fairfield, D. H., Advances in magnetospheric storm and substorm research: 1989-1991, *Journal of Geophysical Research*, Vol. 97, p. 10865, 1992, publlished by the American Geophysical Union.

COPYRIGHT PERMISSION LETTERS

American Geophysical Union
2000 Florida Avenue, N.W.
Washington, D.C. 20009
Phone (202) 462-6900
TWX 710-822-9300
FAX 202-328-0566

AGU POLICY ON REPRODUCTION OF COPYRIGHT MATERIALS

AGU no longer requires that permission be obtained from AGU or the author(s) for the use of tables, figures, or short extracts of papers published in AGU journals or books, provided that the source be appropriately cited; however, the author's permission must be obtained for modifying the material in any way beyond simple redrawing.

We recommend that the credit line read "authors, journal or book title, volume number, page number(s), year, copyright by the American Geophysical Union." If an article was placed in the public domain, in which case the words "Not subject to U.S. copyright" appear on the bottom of the first page of the article, please substitute "published" for the word "copyright" in the credit line mentioned above.

Also, AGU policy requires that the article be published by AGU before any material may be reproduced therefrom.

AGU Publications

I hereby give permission to William B. Cade to reprint the following material in his thesis.

Figures 1 and 2 of:
Axford, W. I., 'Viscous Interaction Between the Solar Wind and the Earth's Magnetosphere', *Planet. Space Sci.*, 12, 45, 1964.

Figure 1 of:
Akasofu, S. I., 'The Development of the Auroral Substorm', *Planet. Space Sci.*, 12(4), 273, 1964.

_____
(Fee)

PERMISSION REQUEST

We hereby grant you permission to reprint the material specified in your letter (see recto) for the purpose you have indicated therein, at no charge, provided that:

1. The material to be used has appeared in our publication without credit or acknowledgement to another source.

2. Suitable acknowledgement to the source is given as follows:

For Books: "Reprinted from (Author/Title), Copyright (Year), Pages No., with kind permission from Pergamon Press Ltd, Headington Hill Hall, Oxford OX3 0BW, UK"

For Journals: "Reprinted from Journal title, Volume number, Author(s), Title of article, Pages No., Copyright (Year), with kind permission from Pergamon Press Ltd, Headington Hill Hall, Oxford 0X3 0BW, UK."

3. Reproduction of this material is confined to the purpose for which permission is hereby given.

Should your thesis be published commercially, please reapply for permission.

For Future Permissions please contact:
Anne-Cecile Junger (Ms)
Subsidiary Rights Manager
Pergamon Press Ltd
Headington Hill Hall
Oxford OX3 OBW, U.K. FAX:(0865)743950

April 8, 1993

APR 2 3 1993

William B. Cade
Center for Atmospheric and Space Science
Utah State University
Logan, Utah 84322
(801) 750-3962

29 APR 1993

Dear Copyright holder,

I am in the process of preparing my thesis in the Physics Department at Utah State University. I hope to complete in the Summer of 1993.

I am requesting your permission to include the attached material as shown. I will include acknowledgements and/or appropriate citations of your work as indicated as well as copyright and reprint rights information in a special appendix. The bibliographical citation will appear at the end of the manuscript as shown. Please advise me of any changes you require.

Please indicate your approval of this request by signing in the space provided, attaching any other form or instruction necessary to confirm permission. If you charge a reprint fee for use of your material, please indicate that as well. If you have any questions, please call me at the number above.

I hope you will be able to reply immediately. If you are not the copyright holder, please forward my request to the appropriate person or institution.

William B. Cade

I hereby give permission to William B. Cade to reprint the following material in his thesis.

Figures 26, 40, 46, 59, 61, and 64 from:
McPherron, R. L., 'Physical Processes Producing Magnetospheric Substorms and Magnetic Storms', in *Geomagnetism*, Vol. 4, edited by J. A. Jacobs, Chapter 7, Academic Press, London, 1991.

_____
(Fee)

_____
(Signature)

PERMISSION GRANTED
provided
The material to be used has appeared in our publication without credit or acknowledgement to another source
Proper credit is given to our publication
Date 30/4/93 By Christine Martin
Rights and Permissions
ACADEMIC PRESS LTD
London, England